BCC-CSM2-HR: A High-Resolution Version of the Beijing Climate Center Climate System Model

Tongwen Wu[1*], Rucong Yu[1], Yixiong Lu[1], Weihua Jie[1], Yongjie Fang[1], Jie Zhang[1], Li Zhang[1], Xiaoge Xin[1], Laurent Li[1,2], Zaizhi Wang[1], Yiming Liu[1], Fang Zhang[1], Fanghua Wu[1], Min Chu[1], Jianglong Li[1], Weiping Li[1], Yanwu Zhang[1], Xueli Shi[1], Wenyan Zhou[1], Junchen Yao[1], Xiangwen Liu[1], He Zhao[1], Jinghui Yan[1], Min Wei[3], Wei Xue[4], Anning Huang[5], Yaocun Zhang[5], Yu Zhang[6], Qi Shu[7], Aixue Hu[8]

1. *Beijing Climate Center, China Meteorological Administration, Beijing, China*
2. *Laboratoire de Météorologie Dynamique, IPSL, CNRS, Sorbonne Université, Ecole Normale Supérieure, Ecole Polytechnique, Paris 75005, France*
3. *National Meteorological Information Center, China Meteorological Administration, Beijing 100081, China.*
4. *Tsinghua University, Beijing 100084, China*
5. *Nanjing University, Nanjing 210023, China*
6. *Chengdu University of Information Technology, Chengdu 610225, China*
7. *The First Institute of Oceanography of the Ministry of Natural Resources, Qingdao 266061, China*
8. *National Center for Atmospheric Research, PO Box 3000, Boulder, Colorado 80307-3000, USA*

*Corresponding author: Tongwen Wu (twwu@cma.gov.cn)

First version on August 23, 2020

Revised on March 27, 2021

Abstract

BCC-CSM2-HR is a high-resolution version of the Beijing Climate Center (BCC) Climate System Model (T266 in the atmosphere and 1/4°lat.×1/4°lon. in the ocean). Its development is on the basis of the medium-resolution version BCC-CSM2-MR (T106 in the atmosphere and 1°lat.×1°lon. in the ocean) which is the baseline for BCC participation in~~to~~ the Coupled Model Intercomparison Project Phase 6 (CMIP6). This study documents the high-resolution model, highlights major improvements in the representation of atmospheric dynamical core and physical processes. BCC-CSM2-HR is evaluated for historical ~~present-day~~ climate simulations from 1950~~71~~ to 2014~~00~~, ~~which are~~ performed under CMIP6-prescribed historical forcing, in comparison with its previous medium-resolution version BCC-CSM2-MR. Observed global warming trend of surface air temperature from 1950 to 2014 are well captured by both BCC-CSM2-MR and BCC-CSM2-HR. ~~We focus on~~ Present-day basic atmospheric mean states during the period from 1995 to 2014 are then evaluated at global scale, followed by an assessment on climate ~~over the globe and~~ variabilities in the tropics including the tropical cyclones (TCs), the El Niño–Southern Oscillation (ENSO), the Madden-Julian Oscillation (MJO), and the quasi-biennial oscillation (QBO) in the stratosphere. It is shown that BCC-CSM2-HR keeps well the global energy balance and can realistically reproduce main patterns of atmosphere temperature and wind, precipitation, land surface air temperature and sea surface temperature (SST). It also improves ~~in~~ the spatial patterns of sea ice and associated seasonal variations in both hemispheres. The bias of double intertropical convergence zone (ITCZ), obvious in BCC-CSM2-MR, ~~is~~ almost disappears~~ed~~ in BCC-CSM2-HR. TC activity in the tropics is increased with resolution enhanced. The cycle of ENSO, the eastward propagative feature and convection intensity of MJO, the downward propagation of QBO in BCC-CSM2-HR are all in a better agreement with observation than their counterparts in BCC-CSM2-MR. ~~We also note s~~Some imperfections are however noted ~~weakness~~ in BCC-CSM2-HR, such as the excessive cloudiness in the

eastern basin of the tropical Pacific with cold ~~Sea Surface Temperature (~~SST~~)~~ biases and the insufficient number of tropical cyclones in the North Atlantic.

1. Introduction.

Accurately modeling climate and weather is a major challenge for the scientific community and needs high spatial resolution. However, many climate models, such as those involved in the Coupled Model Intercomparison Project Phase 5 (CMIP5, Taylor et al., 2012) and the more recent CMIP6 (Eyring et al., 2016)~~Fifth Assessment Report on Climate Change (IPCC AR5)~~, still use a spatial resolution of hundreds of kilometers (Flato et al., 2013). This nominal resolution is suitable for global-scale applications that run simulations for centuries into the future, but fails to capture small-scale phenomena and features that influence local or regional weather and climate events. This resolution is fine enough to simulate mid-latitude weather systems which evolve in thousands of kilometers, but insufficient to describe convective cloud systems that rarely extend beyond a few tens of kilometers. The study of Strachan et al. (2013) showed that while the average tropical cyclone number can be well simulated at a resolution of around 130 km, ~~but~~ grids finer than 60 km are needed to properly simulate the inter-annual variability of cyclone counts. Higher horizontal resolutions (e.g.~~i.e.,~~ 50 km) can further improve the simulated climatology of tropical cyclones (e.g., Oouchi et al., 2006; Zhao et al., 2009; Murakami et al., 2012; Manganello et al., 2012; Bacmeister et al., 2014; Wehner et al., 2015; Reed et al., 2015; Zarzycki et al., 2016). Growing evidence showed that high-resolution models (50 km or finer in the atmosphere) can reproduce the observed intensity of extreme precipitation (Wehner et al., 2010; Endo et al., 2012; Sakamoto et al., 2012). Some phenomena are sensitive to increasing resolution such as ocean mixing (Small et al., 2015), diurnal cycle of precipitation (Sato et al., 2009; Birch et al., 2014; Vellinga et al., 2016), the QBO (Hertwig et al., 2015), the MJO~~'s representation~~ (Peatman et al., 2015), and monsoons (Sperber et al., 1994; Lal et al., 1997; Martin et al., 1999; Yao et al., 2017; Zhang et al. 2018). Some small-scale processes associated with ~~such as~~ mid-latitude storms and tropical cyclones, and ocean eddies also feedback on the simulated large-scale circulation, climate variability and extremes (Smith et al., 2000; Masumoto et al., 2004; Mizuta et al., 2006; Shaffrey et al., 2009; Masson et al., 2012; Doi et al., 2012; Rackow et al., 2016). Many studies (e.g.

Ohfuchi et al., 2004; Zhao et al., 2009; Walsh et al., 2012; Bell et al., 2013; Strachan et al., 2013; Kinter et al. 2013; Demory et al., 2014; Schiemann et al., 2014; Small et al. 2014; Shaevitz et al., 2014; Hertwig et al., 2015; Murakami et al., 2015; Hertwig et al., 2015; Roberts et al. 2016; Hewitt et al. 2016; Roberts C.D. et al, 2018; Roberts M.J. et al., 2019) show that enhanced horizontal resolution in atmospheric and ocean models has many beneficial impacts on model performance and helps to reduce model systematic biases.

High-resolution climate system modelling becomes a key activity within the climate research community, although increasing model resolution needs considerable computational resources. In 2004, the first high-resolution global climate model produced its first simulations using~~within~~ the Japanese Earth Simulator (Ohfuchi et al., 2004; Masumoto et al., 2004). At present day, performing high-resolution climate simulations with model grid smaller than ~~for saying~~ 50 km in the atmosphere and 0.25° in the ocean is still a very costly effort but a growing number of research centers can exercise it ~~and can be realized only at a few research centers~~ (e.g. Shaffrey et al., 2009; Delworth et al., 2012; Mizielinski et al., 2014; Bacmeister et al., 2014; Satoh et al., 2014; Roberts et al., 2018; Zhou et al., 2020). The~~A~~ High Resolution Model Intercomparison Project (HighResMIP, Haarsma et al., 2016) is a CMIP6-endorsed MIP (Model Intercomparison Project)~~proposed as the primary activity within Phase 6 of the Coupled Model Intercomparison Project (CMIP6, Eyring et al., 2016)~~, which aimed to investigate the impact of model ~~horizontal~~ resolution on climate simulation fidelity and systematic model biases.

As a main climate modelling center in China (Wu et al., 2010, 2013, 2014, 2019, 2020; Xin et al., 2013, 2019; Li et al., 2019; Lu et al., 2020a,b), Beijing Climate Center (BCC), China Meteorological Administration, also put important efforts in developing high-resolution fully-coupled Beijing Climate Center Climate System Model (BCC-CSM-HR) (Yu et al., 2014). The currently released version (BCC-CSM2-HR, Table 1) is one of the three BCC model versions (Wu et al., 2019) involved in CMIP6 to run HighResMIP experiment. It is now in its pre-operational phase to become the next generation Beijing Climate Center Climate Prediction

System to produce forecasts at leading times of two weeks to one~~1~~ year. The purpose of this paper is to evaluate its performance by comparing it with the ~~previous version of~~ medium resolution version (BCC-CSM2-MR, Wu et al., 2019). In particular, we ~~evaluate~~ assess their performance to simulate large-scale mean climate and some important phenomena such as the ITCZ, tropical cyclones (TCs), MJO, and QBO which are expected to be improved with enhanced resolution. A relevant description of BCC-CSM2-HR is shown in Section 2, and the experiment design is shown in Section 3. Main results of model performance are presented in Section 4.

2. Model description at high-resolution configuration

Due to the diversity of research and operational needs in BCC, a basic rule that we imposed to ourselves in the development of BCC-CSMs (Wu et al., 2019) is the construction of a traceable hierarchy of model versions running from a coarse grid (T42, approximately 280km), to a medium grid (T106, approximately 110×110 km), and to a fine grid (T266, around 45×45 km). Actually, we fulfilled our target with an achievement to deliver all of these model versions. All of them are fully-coupled models with four components □~~,~~ atmosphere, ocean, land ~~surface~~ and sea-ice □~~,~~ interacting with each other (Wu et al., 2013, 2019, 2020). They are physically coupled through fluxes of momentum, energy, water at their interfaces. The ocean - atmosphere coupling frequency is 30 minutes, which is sufficient to account for the diurnal cycle. As shown in Table 1, the medium resolution of BCC-CSM2-MR is at T106 for the atmosphere and has 46 layers with its model lid at 1.459 hPa. The resolution of the global ocean is of 1° lat. × 1° lon. on average, but $1/3^\circ$ lat. × 1° lon. for the tropical oceans. BCC-CSM2-MR was described in detail in Wu et al. (2019). The atmosphere resolution of BCC-CSM2-HR is T266 on the globe and 56 layers with the top layer at 0.156 hPa (Figure 1) and model lid at 0.092 hPa (Table 1). The ocean and sea ice resolution in BCC-CSM2-HR is $1/4^\circ$ lat. × $1/4^\circ$ lon. and 40 layers in depth. Compared to BCC-CSM2-MR, BCC-CSM2-HR is updated for its dynamical core and model physics in the atmospheric component (Table 1). The ocean and sea ice components are also updated from Modular Ocean Model version 4 (MOM4) and Sea

Ice Simulator version 4 (SIS4) ~~(~~in BCC-CSM2-MR~~)~~ to their version 5 (MOM5 and SIS5), respectively. The land component in the two versions of BCC-CSMs is~~–~~ the Beijing Climate Center Atmosphere-Vegetation Interaction Model ~~BCC–AVIM~~ version 2 (BCC-AVIM2, ~~(~~ Li et al., 2019).

2.1 Atmosphere Model

The atmospheric component of BCC-CSM2-MR is Beijing Climate Center Atmospheric General Circulation Model version 3 (BCC-AGCM3) at~~the~~ medium resolution~~–~~ (BCC-AGCM3-MR), with details being described in Wu et al. (2019) and in a series of relevant publications (Wu et al., 2008, 2010; Wu, 2012; Wu et al., 2013; Lu et al., 2013; Wu et al., 2019; Lu et al., 2020a; Wu et al., 2020). The dynamical core in BCC-AGCM3-MR uses the spectral framework as described in Wu et al. (2008), in which explicit time difference scheme is applied to vorticity equation, semi-implicit time difference scheme for divergence, temperature, and surface pressure equations, and semi-Lagrangian tracer transport scheme is used for water vapor, liquid cloud water and ice cloud water. The main model physics in BCC-AGCM3-MR was described in Wu et al. (2019), which includes the modified scheme of deep convection suggested by Wu (2012), a new diagnostic scheme of cloud amount (Wu et al, 2019), the shallow convection transport scheme of ~~(~~Hack (~~,~~ ~~1~~1994), the stratiform cloud microphysics following~~ed~~ the framework of non-convective cloud processes in NCAR Community Atmosphere Model version 3 (CAM3, Collins et al., 2004) but with a different ~~noticeable~~ treatment for indirect effects of aerosols affecting ~~through mechanisms of~~ clouds and precipitation, the radiative transfer parameterization that was originally implemented in CAM3, a modified boundary layer turbulence parameterization based on the eddy diffusivity approach (Holtslag and Boville, 1993), and a ~~–~~treatments of gravity waves that are generated by a variety of sources related to~~including~~ orography and convection (Lu et al., 2020a).

The atmospheric component in BCC-CSM2-HR is the newly-developed version of BCC-AGCM3 with high~~-—~~resolution (BCC-AGCM3-HR). Main differences between BCC-AGCM3-HR and BCC-AGCM3-MR are listed in Table 1~~,~~ and ~~we will~~ detailed ~~them~~ in the following sub-sections. Actually, the high-resolution atmospheric component has incorporated ~~They respectively used~~ a spatially-varying~~iable~~ divergence damping scheme, amelioration of Wu's deep convective scheme (Wu, 2012), and an integrated consideration for shallow convection and boundary layer processes.

a. Spatially-varying~~iable~~ divergence damping

The performance of a climate model is largely determined by complex motions at different spatio~~al-~~temporal scales and interactions between them~~ of these scales~~. Subgrid-scale motions are generally caused by high-frequency waves, and they can exert impacts on the computational stability especially for a high-resolution model. Horizontal divergence damping is often needed ~~used~~ to control numerical noise in weather forecast models and for numerical stability reasons (Dey, 1978; Bates et al., 1993; Whitehead et al., 2011).

In BCC-AGCM3-HR, a second-order and a fourth-order horizontal Laplacians (∇^2 and ∇^4) are used to realize the damping operation on the divergence field D:

$$\frac{\partial D}{\partial t} = \cdots + k_2 \nabla^2 D, \tag{1}$$

and

$$\frac{\partial D}{\partial t} = \cdots - k_4 \nabla^4 D, \tag{2}$$

where k_2 and k_4 express the damping coefficients for the second-order and fourth-order dissipation operators, respectively. They are generally set as constant parameters. The second-order damping is used for the top three layers and the fourth-order damping for other layers.

Whitehead et al. (2011) proposed a horizontal divergence damping scheme that works on a latitude–longitude grid by using a linear von Neumann analysis. Here, we extended their idea to the spectral dynamical core in our high-resolution model BCC-AGCM3-HR, and we use a second-order horizontal damping operator with spatially-varying~~iable~~ damping coefficient. In order to express the grid spacing dependence of the dissipation, an additional term is introduced in Eqs. (1) and (2) as:

$$\frac{\partial D}{\partial t} = \cdots + k_2\nabla^2 D + k_v\nabla^2 D \qquad (3)$$

and

$$\frac{\partial D}{\partial t} = \cdots - k_4\nabla^4 D + k_v\nabla^2 D. \qquad (4)$$

where

$$k_v = C_s\frac{[A_E\Delta\emptyset]\cdot[A_E\Delta\lambda]}{\Delta t} \qquad (5)$$

~~Here,~~ k_v is dependent on the time-step Δt and grid spacing. A_E in Eq. (5) is the radius of the earth. $\Delta\emptyset$ and $\Delta\lambda$ stand for the latitudinal and longitudinal mesh sizes~~grid spacings~~, respectively. The parameter C_s is designed to depend on vertical position as,

$$C_s = C_{s0}\max\left\langle 1, 8\left\{1+\tanh\left[\ln\left(\frac{p_{top}}{p_k}\right)\right]\right\}\right\rangle, \qquad (6)$$

where C_{s0} is a constant and related to model resolution, p_{top} and p_k are the pressures at the top ~~layer~~ and the kth layers~~one~~ of the model, respectively. The expression (6) provides a rather flat vertical profile until the final two to three model levels, where the damping coefficient is increased rapidly by up to a factor of 8 (Whitehead et al., 2011). This dependence ~~is to~~ introduces a diffusive sponge layer near the model top to absorb rather than reflect outgoing gravity waves (Whitehead et al., 2011). ~~It means that the strength and frequency of the polar instabilities increase near the model top due to this increased damping coefficient, requiring a stronger diffusive operator to remove them, perhaps in addition to the polar Fourier filter.~~ The expression (5) implies the damping coefficient increase with latitude for BCC-AGCMs spectral grid. This spatially-varying~~iable~~ damping scheme can improve the atmospheric temperature simulation in the stratosphere, especially at polar areas of both hemispheres, which~~. This~~ is possibly due to the ~~much m~~more efficient damping of ~~the~~ small-scale meridional waves~~,~~ as Whitehead et al. (2011) pointed out. ~~employing a damping coefficient that neglects the latitudinal variation of the grid cell area will likely damp these meridional waves more effectively.~~

b. Deep convection

In ~~previous version of~~ BCC-AGCM3-MR, as well as in~~used in~~

BCC-AGCM3-HR~~CSM2-MR~~, a modified scheme of the deep cumulus convection developed by Wu (2012) is used (Wu et al., 2019). It is characterized by the following points~~as~~:

(1) Deep convection is initiated at the level of maximum moist static energy above the boundary layer, and~~ the~~ convection is triggered only when the boundary layer is unstable or there exists updraft velocity in the environment at the lifting level of convective cloud, and simultaneously there is positive convective available potential energy (CAPE).

(2) A bulk cloud model is used to calculate the convective updraft with consideration of budgets for mass, dry static energy, moisture, cloud liquid water, and momentum, and the entrainment/detrainment amount for the updraft cloud parcel is determined according to the increase/decrease of updraft parcel mass with altitude.

(3) The convective downdraft is assumed to be saturated and originated from the level of minimum environmental saturated equivalent potential temperature within the updraft cloud.

(4) The closure scheme determines the mass flux at the base of convective cloud, and depends on the decrease/increase of CAPE resulting from large-scale processes.

Along with increasing resolution in BCC-AGCM3-HR, the detrained cloud water can be transported to its adjacent grid boxes, which~~ inside a model time step. ~~ is accomplished in the dynamical core. Part of the horizontally-transported cloud water is permitted ~~assumed ~~to be transferred downward to lower troposphere and the amount of downward transferred water vapor is determined by the horizontally-transported convective cloud water increment ~~change ~~with time. These modifications of the deep convection scheme only in BCC-CSM2-HR are found in favor of~~for~~ improving the simulation of eastward propagation of MJO in the tropics, and their details will be presented in another paper.

c. Boundary layer turbulence

BCC-AGCM3~~CSM2~~-HR employs the University of Washington Moist Turbulence (UWMT) scheme as proposed in Bretherton and Park (2009) to replace the dry turbulence scheme of Holtslag and Boville (1993). The latter was used in

BCC-AGCM3~~CSM2~~-MR. In UWMT, the first-order K diffusion is used to represent all turbulences, by which the turbulent fluxes of a variable χ are written as

$$\overline{w'\chi'} = -K_\chi \frac{\partial \chi}{\partial z} \quad . \qquad (6)$$

The eddy diffusivity, $K\chi$, is calculated based on the turbulent kinetic energy ~~(TKE, e)~~ and proportional to the stability-corrected length scale L ~~lS_χ~~, given by

$$K_\chi = L\sqrt{e}\ \cancel{K_\chi = lS_\chi\sqrt{e}}. \qquad (7)$$

In the case of an entrainment~~inversion~~ layer at the top of convective ~~BLs~~boundary layers (BLs), the diffusivity is parameterized with

$$K_\chi = w_e\Delta z_e\ \cancel{K_\chi = w_e\Delta z_e}, \qquad (8)$$

where ~~w_e is the entrainment rate and~~ Δz_e is the thickness of the entrainment layer, and w_e is the entrainment rate which uses~~.~~ ~~T~~the expression in ~~UWMT scheme uses the~~ Nicholls and Turton (1986) ~~w* entrainment closure~~:

$$w_e = A\frac{w_*^3}{\left(g\Delta^E s_{vl}/s_{vl}\right)\left(z_t - z_b\right)} \quad . \qquad (9)$$

Here, ~~w*~~ w_* is the convective velocity, z_t and z_b are the top and bottom heights of the entrainment layer, Δ^E denotes a jump across the entrainment layer, and ~~svl~~s_{vl} is the liquid virtual static energy. *A* is a nondimensional entrainment efficiency, which is affected by evaporative cooling of mixtures of cloud-top and above-inversion air.

Compared to dry convective BLs over land which is mainly forced by the surface heating, the structure of marine stratocumulus-topped BLs depends strongly on dominant turbulence generating mechanism resulting from both evaporative and radiative cooling at cloud top. The UWMT scheme aims to provide a more physical and realistic treatment of marine stratocumulus-topped BLs and it has been demonstrated that the observed patterns of low-cloud amount with maxima in the subtropical stratocumulus decks can be well reproduced by UWMT in the Community Atmosphere Model (Park and Bretherton, 2009). The implementation of the UWMT scheme in BCC-AGCM3~~CSM2~~-HR is aimed to improve the simulation of the low-level clouds over subtropical eastern oceans and these improvements are found critical to reduce the double-ITCZ bias of precipitation (Lu et al., 2020b).

d. **Shallow convection**

BCC-AGCM~~CSM2~~3-HR basically inherits the shallow convection parameterization used in BCC-AGCM3~~CSM2~~-MR, which is a stability-dependent mass-flux representation of moist convective processes with the use of a simple bulk three-level cloud model, as in Hack (1994). Specifically, in a vertically discrete model atmosphere where the level index *k* decreases upward and considering the case where layers *k* and *k*+1 are moist adiabatically unstable, the Hack scheme assumes the existence of a non-entraining convective element with roots in level *k*+1, condensation and rain out processes in level *k*, and limited detrainment in level *k*-1. By repeated application of this procedure from the bottom of the model to the top, the thermodynamic structure is locally stabilized.

The Hack shallow cumulus scheme can also be~~ also~~ active in moist turbulent mixing, such as stratocumulus entrainment, which has different physical characteristics than cumulus convection. Shallow cumulus is usually regarded as a decoupled BL regime in which the vertical mixing processes do not achieve a single well-mixed layer, while the stratocumulus regime represents a well-mixed BL up to cloud top. The decoupling criterion to distinguish between the two regimes is of great importance for simulating the stratocumulus-to-cumulus transition (Bretherton and Wyant, 1997; Wood and Bretherton, 2004). A number of these decoupling criteria have been explored, such as static stability (Klein and Hartmann, 1993) and buoyancy flux integral ratio (Turton and Nicholls, 1987). In the light of its robustness, the stability criterion with a threshold of 17.5 K is introduced into the Hack scheme. The lower tropospheric stability (*LTS*) is defined as

$$LTS = \theta_{700hPa} - \theta_{sfc}, \tag{10}$$

where θ_{700hPa} and θ_{sfc} are potential temperatures at 700 hPa and at surface, respectively. In BCC-CSM2-HR, the modified Hack scheme is activated only in the decoupled BL regimes with $LTS < 17.5\ \mathrm{K}$ below 700 hPa to remove adiabatically moist instability, and~~. –~~ the original Hack scheme (Hack, 1993) is still retained above 700 hPa to remove any local instability as long as the two adjacent model layers are moist adiabatically unstable. This modification to the triggering of shallow convection is found very useful to improve the simulation of the ITCZ precipitation (Lu et al., 2020b).

2.2 Land surface model

~~The land surface component of BCC-CSM2-MR and BCC-CSM2-HR is the Beijing Climate Center Atmosphere-Vegetation Interaction Model (BCC-AVIM).~~ BCC-AVIM2~~It~~ is a comprehensive land surface model~~scheme~~ developed and maintained in BCC. Its previous ~~The~~ version ~~1 (~~BCC-AVIM1~~.0)~~ was used as the land component in BCC-CSM1.1m participating in CMIP5 (Wu et al., 2013), which~~.~~ includes major land surface biophysical processes treated similarly as in the Community Land Model version 3.0 (CLM3, Oleson et al., 2004) developed at the National Center for Atmospheric Research (NCAR), and plant physiological processes (Ji, 1995; Ji et al., 2008), with 10 layers for soil and up to five layers for snow. The land component in BCC-CSM2-MR and BCC-CSM2-HR is BCC-AVIM version 2~~.2~~ (Li et al., 2019). Updates in BCC-AVIM2 from its precedent version BCC-AVIM1 include a replacement of the water-only lake module by the common land model lake module (CoLM-lake) with a more realistic snow–ice–water–soil framework, a parameterization scheme for rice paddies added in the vegetation module, renewed parameterizations of snow cover fraction and snow surface albedo to accommodate the varied snow aging effect during different stages of a snow season, a revised parameterization to calculate the threshold temperature to initiate freeze (thaw) of soil water (ice) rather than being fixed at 0 ℃ in BCC-AVIM1, a prognostic phenology scheme for vegetation growth instead of empirically prescribed dates for leaf onset/fall, and a renewed scheme to depict solar radiation transfer through the vegetation canopy. ~~It includes major land surface biophysical and plant physiological processes (Ji, 1995; Ji et al., 2008), with 10 layers for soil and up to five layers for snow. The d~~Details of the updating are given in~~may refer to~~ Li et al. (2019). ~~The main difference~~BCC-AVIM2 implemented ~~between~~ in BCC-CSM2-MR and is identical to what implemented in BCC-CSM2-HR, except ~~BCC-AVIM2.2 and BCC-AVIM2.3 is~~ horizontal resolution (same as in their atmosphere component) and the corresponding ~~in the~~ sub-grid surface classification.

2.3 Ocean and Sea Ice Models

The ocean component of BCC-CSM2-MR is MOM4-L40, developed by the Geophysical Fluid Dynamics Laboratory (GFDL, Griffies et al., 2005). It has a nominal resolution of 1°×1° with a tri-pole grid, and the actual resolution is from 1/3° latitude between 10°S and 10°N to 1° at 60° latitude. There are 40 levels in the vertical. More details of its implementation can be found in Wu et al. (2019).

The ocean component of BCC-CSM2-HR is MOM5, also ~~(Modular Ocean Model, version 5.1)~~ developed by ~~the Geophysical Fluid Dynamics Laboratory~~ ~~(~~GFDL (~~,~~ Griffies, 2012). The model is based on the hydrostatic primitive equations and uses the Boussinesq approximation. The model uses Arakawa B-grid in the horizontal, with a globally uniform 0.25° resolution. The quasi-horizontal rescaled height~~-~~ coordinate, namely, z* vertical coordinate is employed to~~for~~ enhancing~~e~~ flexibility of model applications, which allows for the free surface to fluctuate to values as large as the local ocean depth~~and comforts of algorithms~~. There are 50 levels in the vertical, with a resolution of 10 m in the upper ocean and 367 m at the ~~ocean~~ bottom. The tracer advection scheme used in both the horizontal and vertical is the multi-dimensional piecewise parabolic method (MDPPM, Marshall et al., 1997), which is of higher order and more accurate (less dissipative).

MOM5 has a complete set of physical processes with advanced parameterization schemes. Effect of mesoscale eddies through the neutral diffusion scheme of Griffies et al. (1998) is not ~~taken into account~~included in this work~~through the neutral diffusion scheme of Griffies et al. (1998) with a constant diffusivity of 800 m^2 s^{-1} and the neutral slope tapering scheme of Danabasoglu and McWilliams (1995) with the maximum slope of 1/200~~. The K-profile parameterization (KPP) is used to parameterize ocean surface boundary layer processes (Large et al., 1994). MOM5 uses the optical scheme of Manizza et al. (2005) to define the light attenuation exponentials. SeaWiFS chlorophyll-a monthly climatology is used in the calculation of the attenuation of shortwave radiation entering the ocean layers with a maximum depth set at 200m. The re-stratification effect~~s~~ of sub-mesoscale eddies in the ocean surface mixed layer are parameterized with the sub-mesoscale scheme of Fox-Kemper et al. (2008) and Fox-Kemper et al. (2011).

~~The ocean component of BCC-CSM2-MR is MOM4-L40, also developed by the GFDL (Griffies et al., 2005). It has a nominal resolution of 1°×1° with a tri-pole grid, and the actual resolution is from 1/3° latitude between 10°S and 10°N to 1° at 60° latitude. There are 40 levels in the vertical. More details are referred to Wu et al. (2019).~~ The sea-ice component of BCC-CSM2-HR and BCC-CSM2-MR is SIS4 (Winton, 2000) and SIS5 (Delworth et al., 2006) ~~(Sea Ice Simulator)~~ that developed by GFDL ~~(Delworth et al., 2006)~~, respectively. ~~SIS employs Semtner's scheme for the vertical thermodynamics and contains full dynamics with internal ice forces calculated using an elastic-viscous-plastic rheology.~~ Both SIS4 and SIS5 are the sea ice component of MOM4 and MOM5, respectively, and haves three vertical layers~~,~~ including one snow cover and two ice layers of equal thickness. They ~~. The sea-ice component~~ operate~~s~~ on the same oceanic grid of MOM4 in BCC-CSM2-MR and MOM5 in BCC-CSM2-HR, respectively~~and has the same horizontal resolution~~. There are up to five categories of sea ice on each model grid for SIS4 and SI5 according to the thickness of sea ice, and the mutual transformation from one category to another are taken into account under thermodynamic conditions. Both SIS4 and SIS5 employ the scheme of Semtner (1976) for the vertical thermodynamics and contains full dynamics with internal ice forces calculated using an elastic-viscous-plastic rheology.

3. Experimental design and ~~simulations~~data used

3.1 Historical simulation

The principal simulation to be analyzed is the CMIP6 historical ~~simulation~~run (hereafter referred to as historical) with prescribed forcings from 18~~971~~50 to 2014~~00~~ for ~~both~~ BCC-CSM2-MR and from 1950 to 2014 for BCC-CSM2-HR. All historical forcings are from the CMIP6-recommended data (https://esgf-node.llnl.gov/search/input4mips/) including: (1) Greenhouse gases concentrations such as CO_2, N_2O, CH_4, CFC11 and CFC12 with zonal-mean values and updated monthly; (2) Annual means of total solar irradiance derived from the CMIP6 solar forcing; (3) Stratospheric aerosols from volcanoes; (4) CMIP6-recommended tropospheric aerosol optical properties due to anthropogenic emissions that are formulated in terms of nine spatial plumes associated with different major anthropogenic source regions using version 2 of the Max Planck Institute Aerosol Climatology Simple Plume model (MACv2-SP, Stevens et al., 2017); (5) Time-varying gridded ozone concentrations; (6) Yearly global gridded land-use forcing. In addition, aerosol masses based on CMIP5 (Taylor et al., 2012) are also used for the on-line calculation of cloud droplet effective radius in our models.

The historical simulation of BCC-CSM2-MR follows the requirement of CMIP6,~~.~~ with ~~T~~the preindustrial initial state ~~is~~ obtained after a 500-year piControl simulation.~~,~~ ~~and the historical simulation is then conducted~~ It covers the whole period from 1850 to 2014 (Wu et al., 2019). The simulation of BCC-CSM2-HR covers a shorter ~~the~~ historical period from 1950 to 2014. Its initial state is the final state from a 50-year control simulation with fixed historical forcing of the year 1950, following the HighResMIP protocol. The control run itself is initiated from the states of individual components with their uncoupled mode. That is, the state of atmosphere and land are obtained from a 10-year AMIP run forced with monthly climatology of sea surface temperature (SST) and sea ice concentration, while the states of ocean (MOM5) and sea ice (SIS~~v2~~5) are derived from a 1000-year forced run with a repeating annual cycle of monthly climatology of atmospheric state from the Coordinated Ocean-Ice Reference Experiment (CORE) dataset version 2 (Danabasoglu et al., 2014).

3.2 Data used for evaluations

We choose the same period of 1950-2014 from both BCC-CSM2-MR and BCC-CSM2-HR historical simulations to evaluate their performance against observation-based or reanalysis data.

The 1950-2014 monthly global 1 °×1 ° gridded surface temperature from the Hadley Centre–Climatic Research Unit (HadCRUT version 4.6.0.0, available at https://www.metoffice.gov.uk/hadobs/ hadcrut4/) is used to evaluate the global warming trend from BCC-CSM2-MR and BCC-CSM2-HR. HadCRUT (Morice et al., 2012) is a dataset combining land surface air temperature from the Climatic Research Unit (CRUTEM) and Hadley Centre Sea Ice and Sea Surface Temperature (HadISST). CRUTEM is derived from air temperatures near the land surface recorded at weather stations across the globe (Harris et al., 2013). HadISST contains global $1^\circ \times 1^\circ$ sea ice concentration and SST, including in-situ measurements from ships and buoys (Rayner et al., 2003).

For the evaluation of present-day mean climate over the globe and major climate variabilities in the tropics, we choose the recent past 20 years of 1995-2014 as our reference period which will be observed as close as possible for observation-based or reanalysis data, described as follows.

(a) The 2001-2014 monthly global $1^\circ \times 1^\circ$ gridded net radiations at top-of-atmosphere (TOA) from CERES-EBAF version 4.1 products (Loeb et al., 2018, available at https://asdc.larc.nasa.gov/project/CERES/CERES_EBAF_Edition4.1) are used to evaluate the global energy budget in models. CERES-EBAF data are derived on the basis of satellite observation from CERES (Clouds and Earth's Radiant Energy System) and synthesized with EBAF (Energy Balanced and Filled) data. Satellite observation is a direct monitoring of the net radiation at TOA, and a primary source of data for estimating Earth's energy balance (Wielicki et al, 1996).

(b) The 1995-2014 monthly global $0.25^\circ \times 0.25^\circ$ gridded atmospheric temperature and wind from the fifth generation of ECMWF (the European Centre for Medium-Range Weather Forecasts) atmospheric reanalyses (ERA5, Hersbach and Dee 2016) and the climatological data of global zonal mean temperature and wind above the 1-hPa level to 0.1 hPa at 5° latitudes interval from the COSPAR (Committee on Space Research) International Reference Atmosphere (CIRA86) are used to evaluate the vertical structure of atmospheric temperature and wind. The 1995-2014 monthly global gridded wind data from ERA5 are also used to evaluate the quasi-biennial oscillation (QBO) of the equatorial zonal wind between easterlies and westerlies in the tropical stratosphere. CIRA-86 (available at https://catalogue.ceda.ac.uk/uuid/4996e5b2f53ce0b1f2072adadaeda262) includes a global climatology of zonal atmospheric temperature and velocity extending from pole to pole on a 5-degree latitude grid and 0-120 km approximately at 2 km vertical resolution. It is derived from a combination of satellite, radiosonde and ground-based measurements (Fleming et al., 1990).

(c) The 1995–2014 monthly global observed precipitation at 2.5° resolution is taken from the Global Precipitation Climatology Project (GPCP version 2.2; Adler et al., 2003) dataset and used to evaluate the global distribution of precipitation climatology.

(d) The 2001-2014 quasi-global (60° N–60° S) 0.1° × 0.1° gridded half-hourly precipitation estimates of Global Precipitation Measurement (GPM) Integrated Multi-satellitE Retrievals for GPM (IMERG) products (available at https://gpm1.gesdisc.eosdis.nasa.gov/data/GPM_L3/GPM_3IMERGHH.06/) are used to derive 3-hourly data, and then to evaluate the spectrum of precipitation intensity. IMERG uses inter-calibrated estimates from the international constellation of precipitation-relevant satellites and other data sources, including surface precipitation gauge analyses (Huffman et al., 2019).

(e) Two datasets (CRUTEM and HadISST) of the 1995-2014 monthly global 1°×1° gridded surface temperature for the land (Jones et al., 2012) and ocean (Rayner et al., 2003), and gridded sea ice concentration are used to evaluate the model biases of land and ocean temperatures as well as sea ice cover. For the assessment of the ENSO cycle variation, a longer period of 1950-2014 is used from the global monthly HadISST dataset.

(f) The 1995 to 2014 daily global 0.25°×0.25° wind from ERA5, daily global 2.5°×2.5° outgoing longwave radiation (OLR) from NOAA (Liebmann and Smith, 1996), and daily global 2.5°×2.5° precipitation from GPCP (Adler et al., 2003) are used to diagnose the Madden-Julian Oscillation (MJO), which is the dominant mode of sub-seasonal variability in the tropical troposphere (Madden and Julian, 1971). All the data firstly undergo the 20–100-day band-pass-filter.

An analysis of multivariate empirical orthogonal functions (EOFs) and principal components (PCs) is then performed on intra-seasonal OLR, 850-hPa and 200-hPa zonal wind anomalies averaged over 10°S–10°N. Eight MJO phases defined by the inverse tangent of the ratio of PC2 to PC1 as in Wheeler and Hendon (2004) are also reconstructed.

~~(a)~~ The 1995–2014 6-hourly tropical cyclones observations from International Best Track Archive for Climate Stewardship (IBTrACS; Knapp et al., 2010) provide information of all tropical cyclones, including latitude-longitude position, minimum central pressure, and maximum sustained winds (instantaneous values) at a time frequency of every 6 hours. We use the multiple criteria reported by Murakami (2014) to detect TCs with 6-hourly outputs from models (instantaneous values from BCC-CSM2-HR, but accumulated values from BCC-CSM2-MR). (1) The maximum of relative vorticity of a TC-like vortex at 850 hPa exceeds 15×10^{-5} s^{-1} (a threshold that can vary from 1×10^{-5} s^{-1} to 15×10^{-5} s^{-1} in function of resolution (Murakami, 2014). (2) The warm-core above the TC-like vortex, which is presented as the sum of the air temperature deviations (subtracting the maximum temperature from the mean temperature within the TC-like vortex center for an area of 10°×10°) at 300, 500 and 700 hPa, exceeds 0.8 K, a threshold falling in the range 0.6~1.0K that are recommended in Murakami (2014); (3) The maximum wind speed at 850 hPa is higher than that at 300 hPa; (4) The maximum wind speed at 10 m within the TC-like vortex center for an area of 3°×3° grid is higher than 10 m s^{-1}; (5) The genesis position of the TC-like vortex is over the ocean; (6) The duration of the TC-like vortex satisfied above conditions exceeds 48 hours.

(g)

4. ~~4.~~ Results

Data analysis and visualization are generally on the original or native grid of observation and models. An exception is on the assessment of models' biases with contrast to observation. In this case, simulations are re-gridded onto the grid of corresponding observation.

4.1 Global mean surface air temperature variations from 1950 to 2014

The historical simulation from 1950 to 2014 allows us to evaluate the ability of models to reproduce the global warming of near surface temperature. Figure 2 presents global-mean surface air temperature evolutions for HadCRUT4 data and the two BCC models, in which the climatological mean is calculated for the reference period 1961–1990 and removed from the time series to better reveal long-term trends. The interannual variability of both simulations is qualitatively comparable to that observed, and the correlation coefficients reach to 0.84 in both models. A remarkable feature in Figure 2 is the presence of a global warming hiatus or pause for the period from 1998 to 2013 when the observed global surface air temperature warming slowed down. It is interesting that both models reproduce a hiatus, from 2002 to 2010 in BCC-CSM2-MR and from 2004 to 2012 in BCC-CSM2-HR. This warming hiatus is a hot topic (e.g. Fyfe et al., 2016; Medhaug et al., 2017; Wu et al., 2019), largely debated in the scientific research community. The reason why the BCC models simulate the recent global warming hiatus is beyond the scope of this paper and will be explored in other works.

~~**In order to fairly evaluate BCC-CSM2-MR and BCC-CSM2-HR against observation-based or reanalysis data, and to make a right inter-comparison among the three models, we choose a common period of 30 years from 1971 to 2000 from their historical simulations in this work.**~~

~~4.1~~4.2 –Global energy budget

It is to be noted that only the period 2001–2014 is available for CERES-EBAF. For the consistency of comparison, we also shortened data from models and keep the same time interval as in CERES-EBAF. ~~Satellite observation is a direct monitoring of the net radiation at top-of-atmosphere (TOA, Wielicki et al, 1996), which is a primary indicator for the Earth's energy balance. CERES-EBAF products are derived on the~~

~~basis of satellite observation data from CERES (Clouds and Earth's Radiant Energy System) project and synthesized with EBAF (Energy Balanced and Filled) data, suitable for evaluation of climate models. The 2001-2014 monthly global gridded net radiations at top-of-atmosphere (TOA) from CERES-EBAF products are used to evaluate the two versions of BCC-CSM.~~ As shown in Table 2, the globally-averaged TOA net energy is 2.12~~1.81~~ ±0.40~~9~~ W m^{-2} in BCC-CSM2-MR and 1.51~~08~~ ±0.57~~46~~ W m^{-2} in BCC-CSM2-HR for the same period from 2001~~1971~~ to 2014~~00~~. The energy equilibrium of the whole earth system in BCC-CSM2-HR is slightly improved.~~. T~~ The TOA shortwave and longwave components for clear sky in BCC-CSM2-HR are also much closer to CERES-EBAF than in BCC-CSM2-MR. We noted that the TOA shortwave and longwave components for all sky in BCC-CSM2-HR gets lower than CERES-EBAF data and are not improved from BCC-CSM2-MR. This is related to cloud radiative forcing. ~~It is to be noted that only the period 2001–2014 is available for CERES-EBAF. We believe it is still a good climatology to evaluate our models despite the lack of temporal concomitance.~~

Clouds constitute a major modulator of the radiative transfer in the atmosphere, and their radiative properties exert strong impacts on the equilibrium and variation of the radiative budget at TOA. The globally-averaged shortwave cloud radiative forcing in ~~BCC-CSM2-MR and~~ BCC-CSM2-HR is~~are~~ slightly stronger than that in CERES-EBAF (-47.16±0.24 W m^{-2}) about 3 W m^{-2} of cooling effect, and the globally-averaged longwave cloud radiative forcing in ~~the two models are~~ BCC-CSM2-HR is also stronger than the CERES-EBAF data (25.99±0.25 W m^{-2}) near 2 W m^{-2} of warming effect (biases). The globally-averaged shortwave and longwave cloud radiative forcing in BCC-CSM2-MR are much closer to CERES-EBAF.

The obvious biases of model with contrast to CERES-EBAF are mainly located in the mid-latitudes and subtropics. Figure 3~~2~~ shows the annual and zonal mean of shortwave, longwave and net cloud radiative forcing for the two model versions and observations. The longwave and net cloud radiative forcing are overall consistent with CERES-EBAF in most latitudes. In mid-latitudes of both the hemispheres, the shortwave cloud radiative forcing from BCC-CSM2-HR is much closer to CERES-EBAF than ~~that~~ from BCC-CSM2-MR. But in low latitudes between 30 °S and 30 °N, BCC-CSM2-HR simulates excessive cloud shortwave radiative forcing which mainly comes from evident biases over the eastern tropical Pacific and tropical Atlantic oceans (Figure 4~~3~~). These biases are possibly attributable to new treatments for ~~the new scheme of~~ boundary layer processes~~ in which abundant water vapor are confined in the lower atmosphere in those regions~~.

~~4.2~~ Present-day mean climate

4.3

~~4.2.1~~4.3.1 Vertical structure of the atmosphere temperature and wind

Figure ~~4~~5 presents zonally averaged vertical profiles of air temperature and zonal wind for December-January-February (DJF) and June-July-August (JJA) as simulated by BCC-CSM2-MR and BCC-CSM2-HR, with contrast to the ERA5 reanalysis below the 1-hPa level (Hersbach and Dee 2016) and climatological values above the 1-hPa level from ~~the COSPAR (Committee on Space Research) International Reference Atmosphere (~~CIRA86 (~~,~~ Fleming et al., 1990)~~, in which all data except CIRA86 are time averaged over the period from 1971 to 2000~~. The observed vertical profile of atmospheric temperature shows a clear structure of stratification, with an evident seasonal transition. In DJF, it is characterized as cool layers over broader latitudes spanning the transition from troposphere to stratosphere over the Northern Hemisphere, and warm layers spanning from the top of the stratosphere to mesosphere over the Southern Hemisphere. Those different vertical structures in both hemispheres during DJF are almost reversed in JJA. BCC-CSM2-HR is capable of capturing the structure of upper stratosphere and the transition to mesosphere while BCC-CSM2-MR cannot. ~~The air temperature in DJF is characterized as cool layers centralized near about 300 hPa in the Northern Hemisphere and too warm layers near 1 hPa in the Southern Hemisphere. Those different vertical structures in both hemispheres during DJF are almost reversed of JJA. They are clear in~~

~~BCC-CSM2-HR. The warmer layer over top of the stratosphere near 1 hPa cannot be captured in BCC-CSM2-MR as its top is limited at 1.456 hPa.~~

Figure ~~5~~6 shows biases of the zonally-averaged annual air temperature, relative to ERA5. ~~Here o~~Only model data from 5 hPa to 1000 hPa are evaluated as there are spare station-based observations above 5 hPa and it is generally recognized that most of stations don't reach their best-practice altitude of 5 hPa (https://gcos.wmo.int/en/atmospheric-observation-panel-climate). ~~Lower troposphere~~ T~~t~~emperature biases in lower to middle troposphere are relatively small, about -2K to 2K in BCC-CSM2-MR and -1K to 1 K in BCC-CSM2-HR in most latitudes, except in the southern polar region where temperature below 700 hPa are extrapolated values for ERA5 observation and models. The two models BCC-CSM2-MR and BCC-CSM2-HR have a cold ~~negative air temperature~~ bias of air temperature that appears near the tropopause and extends to the stratosphere ~~above the 250 hPa pressure level (Fig. 5)~~ in the subpolar and polar regions. ~~,~~There is also ~~but~~ a thicker layer of warm biases in the lower stratosphere over the tropics and mid-latitude.~~a positive bias above 150 hPa in tropical regions. A prominent cold bias in the lower stratosphere and the upper troposphere does not decrease in magnitude at higher horizontal resolution, and such a negative bias in the troposphere has already been reported in many CMIP5 models (see Charlton-Perez et al., 2013; Tian et al., 2013). In the upper stratosphere, all model versions exhibit a warm bias that is maximal in the mid-latitudes and relatively insensitive to changes in atmospheric resolution.~~ Those temperature biases are not really reduced in BCC-CSM2-HR with a higher horizontal resolution. The cold bias in the troposphere was also reported in many CMIP5 models (see Charlton-Perez et al., 2013; Tian et al., 2013),

As shown in Figure ~~4~~5, the basic pattern of vertical structures of westerly and easterly zones and their changes in DJF and JJA are generally well simulated by BCC-CSM2-MR and BCC-CSM2-HR. Both models have westerly wind biases of annual means that are located in the upper troposphere and stratosphere near 60 °S and 60 °N (Figures ~~5~~6b and ~~6~~5d), and reflect the meridional structure of temperature biases (Figures ~~6~~5a and ~~5~~6c) in accordance with the thermal–wind relationship. ~~The largest~~

~~biases in westerly winds near 100hPa in the tropics may be related to the QBO and its downward propagation.~~

~~Surface Climate~~

~~(a) Precipitation, land surface air temperature and sea surface temperature, sea ice concentration are important variables, and there are rich ground- or satellite-based observations suitable for the assessment of model performance in terms of mean climate.~~

~~4.2.2~~ 4.3.2 Precipitation

~~Observed monthly precipitation is taken from the Global Precipitation Climatology Project (GPCP version 2.2; Adler et al., 2003) data set at 2.5 ° resolution for the period 1981–2010.~~ Figure 7~~6~~ shows the spatial distribution of DJF and JJA mean precipitation for BCC-CSM2-MR and BCC-CSM2-HR, compared to GPCP data. The two versions of BCC-CSMs were both able to reproduce the global observed precipitation patterns and there is an evident improvement in the high-resolution model (BCC-CSM2-HR). Improvements are particularly clear in the Pacific, Indian, and Atlantic Oceans. The double-ITCZ issue is one of the most significant biases that persists in many climate models (e.g., Hwang and Frierson, 2013; Li and Xie, 2014). It exists in BCC-CSM2-MR, with excessive precipitation in the South Pacific Convergence Zone (SPCZ). This bias almost disappears in BCC-CSM2-HR. ~~A strong negative bias of JJA precipitation over the Amazon region exists in the two models.~~ As shown in Figure 8~~7~~, there is too much precipitation along the southern intertropical convergence zone (ITCZ) in BCC-CSM2-MR, which is mainly caused by excessive precipitation in the southern intertropical zone in DJF. This systematic bias is evidently reduced ~~improved~~ in BCC-CSM2-HR, especially with weakened precipitation in the South Pacific Convergence Zone (SPCZ). ~~.~~The improvement of SPCZ precipitation in BCC-CSM2-HR might be attributed to the implementation of the UWMT scheme which improved the simulation of low-level clouds over the tropical eastern South Pacific (Lu et al., 2020b) and reduced warm biases there (Fig. 10c). But the intensity of precipitation in the northern intertropical convergence zone in BCC-CSM2-HR is stronger than that from GPCP, which is partly attributed to the excessive precipitation in the tropical oceans, especially in the eastern tropical North Pacific (Figure 7~~6~~e). ~~—~~A strong negative bias of JJA precipitation over the Amazon region exists in the two models. In Figure 7f, we also noted that the amount of JJA precipitation in east of the Philippines and near the Pacific warm pool is worsened, since it is smaller in BCC-CSM2-HR than in BCC-CSM2-MR and GPCP data. This bias of lacking precipitation in BCC-CSM2-HR may partly be caused by a cold-SST bias over the western Pacific warm pool (Fig.10c).

~~The 2001-2019 quasi-global (60° N–60° S) 0.1° × 0.1° gridded half-hourly precipitation estimates of Global Precipitation Measurement (GPM) Integrated Multi-satellitE Retrievals for GPM (IMERG) products are used to evaluate the precipitation intensity in BCC-CSMs. IMERG data are rainfall estimates combining data from all passive-microwave instruments in the GPM Constellation, together with microwave-calibrated infrared satellite estimates, precipitation gauge analyses, and potentially other precipitation estimators at fine time over the entire globe (Huffman et al., 2019).~~ Figure 9~~8~~ shows the probability density of 3-hourly precipitation between 40°S and 40°N in function of precipitation intensity with intervals of 1 mm/hour~~ between 40°S and 40°N~~. The frequency of light rainfall events~~, with precipitation rate~~ smaller than 1 mm/hour, in ~~the two versions of~~ BCC-CSM2-MR~~s~~ is ~~both~~ higher than in IMERG.~~ data, b~~ But strong ~~lower for~~ precipitation events ~~rate~~ exceeding 10 mm/hour, are clearly insufficient~~.~~ This is a common bias in many global climate models raising concerns for any studies on precipitation extremes. Compared to BCC-CSM2-MR, BCC-CSM2-HR with resolution increased shows substantial improvements for its precipitation spectrum: reduced ~~obvious improvement for its ability to~~ light rainfall and enhanced heavy rainfall events. The spectral distribution of precipitation in BCC-CSM2-HR is much closer to

IMERG.~~capture the spectral distribution of precipitation, especially the contrast between heavy and light rains.~~

4.3.3 SST~~Near-surface temperature~~

~~Global monthly mean sea surface temperature (SST) from 1971 to 2000 is taken from the EN4 objective analysis (Good et al., 2013), and land surface air temperature at 2 m is derived from the Climatic Research Unit (CRU) data set (Harris et al., 2013).~~ Figure 10~~9~~ shows a spatial-distribution map of the 1995-2014 annual mean SST for HadISST~~EN4~~ and the biases for BCC-CSM2-MR and BCC-CSM2-HR relative to HadISST~~EN4~~. BCC-CSM2-MR is generally warmer, while BCC-CSM2-HR is colder than what observed. A warm SST bias in BCC-CSM2-MR spreads throughout most oceans, except the north Pacific and north Atlantic. Such warm biases do not appear in BCC-CSM2-HR, and the cold SST biases in the eastern subtropical south Pacific are possibly attributed to excessive clouds there, also manifested by strong cloud shortwave radiative forcing (Figure 4e). The warm biases in the eastern tropical ocean basins in BCC-CSM2-MR are associated with a deficit of stratiform low-level clouds, a common and systematic bias for many climate models (Richter, 2015). The cold biases there in BCC-CSM2-HR, similarly, are associated with too much low cloud, except over the tropical north Pacific. We also noted that a belt of warm SST biases in the Kuroshio extension and in the North Atlantic in both models (Figures 10b and 10c), especially in the high-resolution model. This bias may be partly resulted from the coarse resolution of HadISST data used, as SST near the Kuroshio shows strong temperature gradients with filamentous structures (Shi and Wang, 2020).

4.3.4 Land-surface air temperature

Figure 11~~0~~ shows the simulation biases of annual mean land-surface air temperature from BCC-CSM2-MR and BCC-CSM2-HR. The near-surface air temperature over land in BCC-CSM2-MR is generally cold~~oler~~er than the CRUTEM observations, particularly exhibiting severe cold~~ol~~ biases in North Europe. As there are no physical (but only resolution) changes in the land modeling component in the two models, the systematic biases of near-surface air temperature over land are very similar to each other. Increasing atmospheric resolution in BCC-CSM2-HR does not seem to show amelioration, and the surface air temperatures in BCC-CSM2-HR exhibits rather similar patterns ~~for their biases~~ as in BCC-CSM2-MR with ~~and there are~~ biases of -2 to 2 K in most land regions between 50 °N and 50 °S compared~~with contrast to~~ to CRU data.

~~4.3.3~~

~~4.3.4~~4.3.5 Sea ice

Figure 12~~1~~ shows the annual mean sea ice concentration simulated by BCC-CSM2-MR and BCC-CSM2-HR over the period 1995~~71~~–2014~~00~~, compared to ~~the climatology (1971–2000) from~~HadISST observation data ~~Hadley Centre Sea Ice and Sea Surface Temperature data set (HadISST, Rayner et al., 2003)~~. The simulated geographic distribution of sea ice in the Arctic is overall realistic, except that the sea ice concentration in the Atlantic is slightly overestimated in both models. This overestimation of sea ice possibly has a consequence for the severe cold biases of surface air temperature in North Europe (Figure 1~~0~~1). In the Antarctic, sea ice concentration simulated by BCC-CSM2-MR is smaller than HadISST data, especially from 60 °W to 60 °E in the subpolar region where the simulated SST is warmer compared to HadISST data~~EN4~~ (Figure 10~~9~~b). Those deficiencies in BCC-CSM2-MR (Figure 12e) are largely reduced ~~improved~~ in BCC-CSM2-HR (Figure 12~~1~~f).

Figure 13~~2~~ shows the monthly sea ice covers for the Arctic and Antarctic from BCC-CSM2-MR and BCC-CSM2-HR. HadISST observations show that the Arctic sea ice cover reaches a minimum extent of 6.9×10^6 km^2 in September and rises to a maximum extent of 16.0×10^6 km^2 in March, and the Antarctic sea ice cover reaches a minimum extent in February and a maximum extent in September. The seasonal cycle amplitude and phase of sea ice area are well captured by the two models, and their biases are ~~almost~~ mostly smaller than 1×10^6 km^2 while compared to HadISST observations. We note that the extents of the Arctic sea ice for each month in BCC-CSM2-MR are slightly but systematically smaller than HadISST, and in the

Antarctic are smaller~~less~~ in February and March but larger in other months than HadISST. BCC-CSM2-HR slightly overestimated sea ice concentration by about 1×10^{6} km^{2} in both hemispheres with reference to HadISST.

~~5~~

~~5.3~~4.4 Variabilities in the T~~T~~ropics~~al Climate~~

The tropical cyclone (TC), also known as typhoon or hurricane, is among the most destructive weather phenomena. The Madden-Julian Oscillation (MJO) is the dominant mode of sub-seasonal variability in the tropical troposphere (Madden and Julian, 1971), and the quasi-biennial oscillation (QBO) is a quasiperiodic oscillation of the equatorial zonal wind between easterlies and westerlies in the tropical stratosphere. TC, MJO and QBO are very important variabilities in the tropics, with consequences to global weather and climate.

4.4.1~~The tropical cyclone (TC), also known as typhoon or hurricane, is among the most destructive weather phenomena. The Madden-Julian Oscillation (MJO) is the dominant mode of sub-seasonal variability in the tropical troposphere (Madden and Julian, 1971), and the quasi-biennial oscillation (QBO) is a quasiperiodic oscillation of the equatorial zonal wind between easterlies and westerlies in the tropical stratosphere. TC, MJO and QBO are very important variabilities in the tropics, with consequences to global weather and climate.~~

Tropical Cyclones

~~Following previous studies (Murakami, 2014), we use multiple criteria to detect TCs in our simulations. (1) The maximum of daily relative vorticity of a TC-like vortex at 850 hPa exceeds 15×10-5 s-1 for BCC-CSM2-HR and 1×10-5 s-1 for BCC-CSM2-MR; (2) The warm-core above the TC-like vortex, which is presented as the sum of the air temperature deviations at 300, 500 and 700 hPa over a 10°×10° grid box, exceeds 0.8 K; (3) The maximum wind speed at 850 hPa is higher than that at 300 hPa; (4) The maximum wind speed within the TC-like vortex center 3°×3°~~

~~grid box is higher than 10 m s-1; (5) The genesis position of the TC-like vortex is over the ocean; (6) The duration of the TC-like vortex satisfied above conditions exceeds 48 hours.~~

In Figure 1~~3~~4, we evaluate the average TC frequency over ~~the~~ twenty years (1995~~81~~-2014~~00~~) from BCC-CSM2-MR and BCC-CSM2-HR, with contrast to the climatology ~~(1981–2000)~~ of 1995-2014 observations from International Best Track Archive for Climate Stewardship (IBTrACS; Knapp et al., 2010). It is clear that TC activity is increased with resolution enhanced. The averaged total global TC numbers per year are 49.6~~58.3~~ in BCC-CSM2-MR and 94.4~~2.3~~ in BCC-CSM2-HR, and the global TC numbers in BCC-CSM2-HR is much closer to the IBTrACS observation (90.2). The global TC number is slightly influenced by the threshold (15×10^{-5} s^{-1} in Figure 14) of relative vorticity at 850 hPa used to detect TC. If this threshold gets looser to 5×10^{-5} s^{-1}, the averaged total global TC numbers per year in BCC-CSM2-MR and BCC-CSM2-HR would enhance to 55.9 and 101.5 (not shown), respectively. The low TC number in BCC-CSM2-MR is furthermore explained by the fact that its 6-hourly data used to detect TC are averaged values in the 6-hour interval, while instantaneous values would be more appropriate as in IBTrACS and BCC-CSM2-HR. ~~, and are slightly larger than IBTrACS observation (89.7), although one of the above criteria for TC in BCC-CSM2-MR is looser than that in BCC-CSM2-HR.~~ Spatially, BCC-CSM2-HR generates excess TC activity in the eastern North Pacific, Northern Indian Ocean, and Southern Hemisphere. But both models severely underestimate TC activity in the North Atlantic and in the Caribbean Sea. The general overestimation of TC activity in the eastern North Pacific and ~~over~~ the opposite in the North Atlantic in BCC-CSM2-HR may be related to the warmer SST in the eastern tropical North Pacific and colder SST in the tropical Atlantic with contrast to HadISST ~~EN4~~ data (Figure 10~~9~~c), but other factors such as the entrainment in the parameterization of convection (Zhao et al., 2012) and air-sea coupling (Li and Sriver, 2018) may also have an influence ~~(Zhao et al., 2012)~~. ~~The biases of missing TC activity in the North Atlantic also exist in other models (e.g., Bell et al., 2013; Strachan et al., 2013; Small et al., 2014), and still remain a challenge for the climate~~

~~modelling community.~~ The study of Li and Sriver (2018) showed that ocean coupling influences simulated TC frequency, geographical distributions, and storm intensity, and TC tracks are relatively sparse in the coupled simulations than in un-coupled simulations.

Figure 1~~4~~5 shows the maximum surface wind speed versus minimum sea level pressure for the tropical cyclones that are derived from the 1995~~81~~-2014~~00~~ ~~daily~~ IBTrACS observation (black dots and line), and ~~from the 1981-2000 daily~~ simulations of BCC-CSM2-MR and BCC-CSM2-HR. Here, the maximum surface wind speed (minimum sea level pressure) of a given TC was defined as the instantaneous maximum (minimum) of the 6-hours interval in IBTrACS and BCC-CSM2-HR, but averaged value in BCC-CSM2-MR for wind speed at 10m (sea level pressure). Instantaneous values of wind speed and sea level pressure were not recorded as output in BCC-CSM2-MR. ~~Consistent with other similar studies (e.g., Yamada et al., 2017), BCC-CSM2-MR and BCC-CSM2-HR cannot capture weak storms whose maximum wind speeds are less than 10 m s^{-1}.~~ Maximum wind speeds for TC lifetime in BCC-CSM2-MR are consistently weaker than BCC-CSM2-HR and IBTrACS, which is understandable given the coarser resolution. BCC-CSM2-MR cannot capture strong storms, ~~The maximum wind speed for TC in BCC-CSM2-MR~~ and maximum wind speeds at 10m only reach~~es~~ to 30 m s^{-1}~~.~~. –BCC-CSM2-HR, as expected, can reproduce those strong TCs for which ~~daily mean~~ minimum pressure of TC lifetime ~~in TC centers~~ may reach to 960 hPa and ~~daily mean~~ maximum wind speed at 10m may reach to 50 m s^{-1}. The fitting line of maximum wind speeds with minimum center pressures in BCC-CSM2-HR almost matches that from IBTrACS observation (Figure 15~~4~~). The BCC-CSM2-HR simulations just as previous studies have shown (e.g., Murakami et al., 2012; Sugi et al., 2017; Vecchi et al., 2019) demonstrate that the maximum wind speed of TC simulated by a model with approximately 50 km resolution can reach up to 50~60 m s^{-1}.

4.4.2 Madden–Julian Oscillation

MJO is the dominant mode of sub-seasonal variability in the tropical troposphere (Madden and Julian, 1971), and ~~MJO is~~ characterized by eastward propagation of deep convective structures ~~moving~~ along the Equator with an average phase speed of around 5 m s^{-1} at the intraseasonal time scale of 20–100 days (Wheeler and Kiladis, 1999). MJO generally forms over the Indian Ocean, strengthens over the Pacific Ocean, and weakens due to interaction with South America and cooler eastern Pacific SSTs (Madden and Julian, 1971). Figure 16~~5~~ gives the time lag-longitude evolution of 10°S–10°N-averaged intraseasonal precipitation anomalies for the left panels and time lag-longitude evolution of 80°–100°E-averaged intraseasonal precipitation anomalies correlated against the precipitation over the equatorial eastern Indian Ocean for the right pancels. Both versions of BCC-CSMs reasonably reproduce the eastward propagating feature of convection from the Indian Ocean across the Maritime Continent to the Pacific (Figs. 16~~5~~b and 16~~5~~c), as well as the apparent poleward propagations from the equatorial Indian Ocean into the Northern Hemisphere and the Southern Hemisphere (Figs. 16~~5~~e and 16~~5~~f). The signal of northward propagation is more evident ~~skillfully depicted in simulations~~ in BCC-CSM2-HR than in BCC-CSM2-MR. The average phase speed of eastward propagation of deep convection in BCC-CSM2-HR is much closer to ~~the~~ GPCP data denoted by the dashed line in Fig 1~~5~~6c. Figure 16~~5~~b shows that the eastward propagation of deep convection in BCC-CSM2-MR is too fast, compared to GPCP data.

MJO activity can be generally featured by a life cycle of eight phases (Wheeler and Hendon, 2004). Intensity of outgoing longwave radiation (OLR) is often used for this purpose to represent the activity of convection. Figure 1~~6~~7 shows the MJO phase-latitude diagram of composited outgoing longwave radiation (OLR) and 850-hPa zonal wind anomalies averaged over 10°S–10°N. ~~Here, on the basis of extracting the leading multivariate empirical orthogonal functions (EOFs) and principal components (PCs) of intra-seasonal OLR, 850-hPa and 200-hPa zonal wind anomalies, eight MJO phases are defined by the inverse tangent of the ratio of PC2 to PC1 as in Wheeler and Hendon (2004).~~ In observation, MJO convection initiated from Africa and the western Indian Ocean at phases 1–2, propagates eastward from the Indian Ocean across the Maritime Continent to the western Pacific at phases 3–6, and finally disappears in the western hemisphere at phases 7–8. BCC-CSM2-MR generally captures the evolution of convection with MJO phases, but shows faster propagative speed and apparently underestimates the intensity compared to the observation. In contrast, BCC-CSM2-HR shows an obviously improved MJO phase transition and convection intensity.

4.4.3 The stratospheric quasi-biennial oscillation

The alternative oscillation between westerly and easterly winds in the tropical stratosphere constitutes the characteristic feature of the quasi-biennial oscillation (QBO). A~~The~~ good simulation of QBO still remains nowadays a challenge for all state-of-the-art climate models. In a recent work, Kim et al. (2020) showed that only half (15 out of 30) of the CMIP6 models can internally generate QBO (BCC-CSM2-MR was in the good half). We should however recognize that there was a huge progress in CMIP6, since in CMIP5 only five models (about 10% of the total) were able to simulate a realistic QBO (Schenzinger et al., 2017).

To evaluate model performance in simulating the QBO, the time-height cross sections of the tropical zonal winds averaged from 5°S to 5°N for BCC-CSM2-MR and BCC-CSM2-HR are compared with contrast to the ERA5 reanalysis. As shown in Figure 18~~7~~, ERA5 shows alternative westerlies and easterlies in the lower stratosphere with a mean periodicity of about 28 months. The two BCC models are both able to generate a reasonable QBO, and the observed asymmetry ~~in amplitude~~ with the easterlies being stronger than the westerlies are also well reproduced. The general performance of QBO in BCC-CSM2-MR was evaluated in Wu et al. (2019). A detailed assessment of the underlying mechanism involving wave dynamics and the associated forcing to drive QBO is presented in Lu et al. (2020a). The simulated QBO has stronger amplitudes in BCC-CSM2-HR than in BCC-CSM2-MR. As the horizontal resolution and physics package are changed from BCC-CSM2-MR to BCC-CSM2-HR, the parameterized convective gravity wave forcing for QBO ~~seems~~ could be potentially enhanced in BCC-CSM2-HR. On the other hand, changes in the convective cumulus parameterization can also affect the simulation of the resolved convectively coupled equatorial waves (i.e., the Kelvin wave) driving the QBO, and lead to stronger QBO amplitudes in BCC-CSM2-HR.

In the two BCC models, the downward propagation of QBO occurs in a regular manner, but does not sufficiently penetrate to low altitudes below 50 hPa. The vertical resolution is similar below ~10 hPa in both BCC-CSM2-MR and BCC-CSM2-HR (Figure 1). A further downward propagation to lower altitudes can be expected by increasing the vertical resolution finer than 500 m to adequately resolve the wave-mean flow interaction in the upper troposphere-lower stratosphere (Geller et al. 2016; Garcia and Richter 2019).

4.4.4 Niño3.4 SST variability

Figure 19~~18~~ presents time series of the monthly Niño3.4 SST (5°N−5°S, 170°W−120°W) anomalies from BCC-CSM2-MR and BCC-CSM2-HR, with reference to HadISST~~EN4~~ data from 1950~~71~~ to 2014~~00~~. The amplitude of interannual variation of the Nino3.4 index in BCC-CSM2-HR and BCC-CSM2-MR are both ~~is~~ stronger ~~weaker~~ than in HadISST~~EN4 and in BCC-CSM2-MR.~~. Those strong amplitudes may partly come from the slight warming trends in both models. The power spectrum analysis of the Niño3.4 index from the HadISST ~~EN4~~ observations shows significant peaks at 4-6 years and 2-3 years. The periodicity of the ENSO cycle in BCC-CSM2-MR is mainly at 2-3 years. It is prolonged to 3-6~~4~~ years in BCC-CSM2-HR. As in ~~In~~ Figure 19h~~18e~~, the Niño3.4~~El Niño~~ SST variability from HadISST~~EN4~~ data reaches its maximum in the period from November to January. The phase locking (i.e., the preferred timing in the year for the peak of ENSO) simulated by BCC-CSM2-MR occurs in autumn. The simulated ENSO phase locking in BCC-CSM2-HR is partly improved, since ~~and the~~ ENSO events tend to reach their maximum toward winter~~, in spite of two months lag in the peak time~~.

Recent studies of Hayashi et al. (2020) showed that the ability to simulate the asymmetry between warm (El Niño) and cold (La Niña) phases as recorded in observations is still very poor for most CMIP5 and CMIP6 models. This imperfection also exists in both BCC-CSM2-HR and BCC-CSM2-MR. The asymmetry in SST anomalies is often measured by the normalized third statistical moment, i.e., skewness (Burgers and Stephenson, 1999). Figures 19d-f show spatial maps of the skewness of monthly SST anomalies (SSTA) in the tropical Pacific that are calculated following the methodology in Burgers and Stephenson (1999). In the eastern Pacific, the ENSO signal from HadISST data is the strongest and the observed SSTA skewness is highly positive (Fig. 19d) due to the presence of extreme El Niño events and absence of extreme La Niña events. The skewness values of SSTA in both models (Figs. 19e and 19f) are underestimated with contrast to HadISST observation, and the area of positive skewness in the eastern tropical Pacific from BCC-CSM2-HR simulations is much closer to HadISST data.

Figure 20 ~~19~~ presents the spatial patterns of correlation coefficients between the Niño3.4 index and the corresponding global SST anomalies from 1950~~71~~ to 2014~~00~~ for the HadISST~~EN4~~ observation and the two BCC models. Both BCC-CSM2-HR and BCC-CSM2-MR simulate a positive correlation structure over the equatorial region of the central and eastern Pacific, which is consistent with the analysis from HadISST~~EN4~~ despite an over extension ~~of a too westward extension~~ into the western Pacific. The HadISST~~EN4~~ data show clearly that the zone of positive correlation of SST with the Niño3.4 index in the equatorial eastern Pacific expands to extra-tropics. Especially along the eastern border of the Pacific, the areas of high values of positive correlations in BCC-CSM2-HR are larger than BCC-CSM2-MR, and much closer to HadISST. ~~There are also remarkable areas of positive correlation in the equatorial Indian Ocean and the eastern tropical Atlantic.~~ Compared to BCC-CSM2-MR, BCC-CSM2-HR improves the simulation in the equatorial Indian Ocean and the eastern tropical Atlantic where there are also remarkable areas of positive correlation~~in those regions~~. We also note that areas of negative correlation of SST with the Niño3.4 index in the western equatorial Pacific extend to the south and north Pacific in HadISST~~EN4~~, ~~a phenomenon however not clearly simulated in~~ which is clearer in BCC-CSM2-HR than in ~~, even deteriorated compared to~~ BCC-CSM2-MR.

5. Conclusions and discussions

This paper was devoted to the presentation of the high-resolution version BCC-CSM2-HR and to the description of its climate simulation performance. We focused on its updating and differential characteristics from its predecessor, the medium-resolution version BCC-CSM2-MR. BCC-CSM2-HR is our model version participating in~~to~~ ~~the~~ HighResMIP, while BCC-CSM2-MR is our basic model version participating in ~~for~~ other CMIP6-e~~E~~ndorsed MIPs (Wu et al., 2019; Xin et al. 2019).

The atmosphere resolution is increased from T106L46 in BCC-CSM2-MR to T266L56 in BCC-CSM2-HR, and the ocean resolution from 1°×1° ~~in BCC-CSM2-MR~~ to 1/4°×1/4° ~~in BCC-CSM2-HR~~. A few novel developments were implemented in BCC-CSM2-HR for both the dynamical~~s~~ core and model physics in the atmospheric component;~~.~~ First~~ly~~, a spatially-varying~~iable~~ damping for the divergence field was used to improve the atmospheric temperature simulation in the stratosphere at polar areas. It helps to control high-frequency noise in the stratosphere and above;~~.~~ Second~~ly~~, the deep cumulus convection scheme originally described in Wu (2012) was further ameliorated to allow detrained cloud water be transported to adjacent grids and downward to lower troposphere;~~.~~ Third~~ly~~, we modified the relevant schemes for the boundary layer turbulence and shallow cumulus convection to improve the simulation of ITCZ precipitation;~~.~~ Fourth,~~inally~~ the UWMT scheme is used to improve the simulation of ~~the~~ low-level clouds over eastern basins of subtropical oceans. The land model configuration in BCC-CSM2-HR is the same as ~~that~~ in BCC-CSM2-MR. Major land surface biophysical and plant physiological processes of BCC-AVIM2 implemented in BCC-CSM2-MR and BCC-CSM2-HR keep the same, and only~~main~~ differences are in the sub-grid surface classification. The ocean component of BCC-CSM2-HR is upgraded from MOM4 in BCC-CSM2-MR to MOM5. The sea ice component is also updated from SIS4 ~~in BCC-CSM2-MR~~ to SIS5 ~~in BCC-CSM2-HR~~.

For the sake of a rigorous comparison, historical simulations with fully coupled BCC-CSM2-MR and BCC-CSM2-HR are analyzed over a 65 year period from 1950 to 2014~~two simulations of 30 years each were realized under the same historical conditions from 1971 to 2000 with BCC-CSM2-MR and BCC-CSM2-HR, respectively~~. The long-term trends of 1950-2014 globally-averaged annual-mean surface air temperature from both BCC-CSM2-MR and BCC-CSM2-HR are highly correlated to HadCRUT4 observation. The global warming in the latter half of the 20^{th}

century is well simulated, and the observed global warming hiatus or slowdown in the period from 1998 to 2013 is generally captured by both model versions.

We compared the 1995-2014 basic climate features in relation to atmospheric temperature, circulation, precipitation, surface temperature, and sea ice between the two simulations and we evaluated them against observation-based and reanalysis data. With contrast to the medium-resolution BCC-CSM2-MR, the high-resolution BCC-CSM2-HR has ~~a~~ slightly improved energy equilibrium for the whole earth system. The global mean TOA net energy balance is about 1.51~~08~~ W m^{-2} in BCC-CSM2-HR for the period from 1995~~71~~ to 2014~~00~~, showing an evident improvement compared to 2.12~~1.81~~ W m^{-2} in BCC-CSM2-MR. The longwave and net cloud radiative forcing are overall consistent with CERES-EBAF in most latitudes, but excessive cloud radiative forcing for shortwave radiation is found over the eastern tropical Pacific and tropical Atlantic in BCC-CSM2-HR. ~~Lower troposphere~~ T~~t~~emperature biases in the low- to mid-troposphere below 300 hPa ~~—~~in BCC-CSM2-HR are relatively small, within the range of -1K to 1K. Both versions of BCC-CSMs have a cold air temperature bias that appears above 250 hPa in the subpolar and polar region, and a warm bias in the upper stratosphere in the mid-latitudes, which caused westerly wind biases in the upper troposphere and in the stratosphere.

Although those prominent systematic biases in temperature and wind ~~do not change at higher horizontal and vertical resolution and~~ seem~~s~~ relatively insensitive to changes in atmospheric resolution, the ability to capture the winter to summer seasonal transition ~~change~~ in the vertical structure of temperature and wind in the upper stratosphere is strengthened in BCC-CSM2-HR.

The two versions of BCC-CSMs were both able to reproduce the observed global precipitation patterns and there is a remarkable improvement in precipitation centers over the Pacific, Indian, and Atlantic Oceans in the high-resolution model. The double-ITCZ biases in BCC-CSM2-MR are reduced in BCC-CSM2-HR and excessive precipitation in the South Pacific Convergence Zone is also strongly reduced in BCC-CSM2-HR. The climatological SST in BCC-CSM2-HR, relative to the observation-based HadISST~~EN4~~ data, shows cold biases but reduced compared to BCC-CSM2-MR. Such SST cold biases are partly attributable to different ocean components, MOM4 in BCC-CSM2-MR and MOM5 in BCC-CSM2-HR. The seasonal cycles of amplitude and phase of sea ice in both hemispheres are generally well captured in BCC-CSM2-HR, but with a small excess all year round in the Northern Hemisphere, especially in the Atlantic.

We also conducted an assessment on a few important phenomena of the tropical climate, such as TC (tropical cyclone), MJO (Madden-Julian oscillation), QBO (quasi-biennial oscillation), and ENSO (El Nino – southern oscillation). The averaged total number of global TC in BCC-CSM2-HR is a bit larger than in IBTrACS observation. BCC-CSM2-HR can simulate main TC activities in the eastern North Pacific, Northern Indian, and in the Southern Hemisphere but misses the TC activities in the North Atlantic. BCC-CSM2-HR is able to capture a realistic MJO signal including the eastward-propagating behavior of MJO and its phase speed. The QBO-related alternative westerlies and easterlies in the tropical lower stratosphere with a mean periodicity of about 28 months are well simulated. The weakness in downward propagation of the simulated QBO (insufficient penetration of the signal to low altitudes) in BCC-CSM2-MR is slightly improved in BCC-CSM2-HR. Main features of the ENSO cycle such as the periodicity and phase locking are captured by BCC-CSM2-HR although its main ENSO periodicity of 3-6~~4~~ years is still shorter compared to~~than~~ HadISST~~EN4~~ observations~~ and the pick time of ENSO variability is about two months later compared to EN4 data~~.

Our work shows that enhancing resolution does not noticeably improve climate mean state and deterioration is even possible. For example, the decrease of JJA precipitation over the warm pool in our high-resolution model is still an important issue which certainly deserves further investigations with multiple models and simulations. Actually, other studies also reported similar issues. Haarsma et al. (2020) shows that increasing resolution in the EC-Earth model deteriorated the wet bias over the western Pacific warm pool. Bacmeister et al. (2014) analysed the high-resolution climate simulations performed with the Community Atmosphere Model (CAM), and showed that dry bias over the same region with enhanced resolution. Over the western Pacific warm pool, the atmospheric circulation and precipitation undergoes not only the impact of tropical variations such as MJO and TC, but also strong regional air-sea coupling.

We finally should note that there exist some systematic biases in our high-resolution model, such as the excessive cloud radiative forcing for shortwave radiation over the eastern tropical Pacific, cold biases in the near surface temperature over North Europe~~,~~ and over the tropical Atlantic, insufficient TC activities over the North Atlantic and the Caribbean Sea. These are all important issues motivating us to develop and implement more physically-based parameterizations in our future work. For the lack of sufficient TC activities in the North Atlantic, it seems that this bias also exists in other models (e.g., Bell et al., 2013; Strachan et al., 2013; Small et al., 2014) and still remains a challenging issue for the climate modelling community. A recent study reported by Davis (2018) showed that models with horizontal grid spacing of one fourth degree or coarser could not produce a realistic number of category 4 and 5 storms in the tropical Atlantic. The spatial resolution even in our current high-resolution model seems too coarse. ~~se are all important issues to improve in our future model development.~~

Code and data availability

Source codes of BCC-CSM-HR model can be accessed at a DOI repository http://doi.org/10.5281/zenodo.4127457 (Wu et al., 2020b). Model output of BCC models for CMIP6 simulations described in this paper is distributed through the Earth System Grid Federation (ESGF) and freely accessible through the ESGF data portals after registration (http://doi.org/10.22033/ESGF/CMIP6.2921, Jie et al., 2020). Details about ESGF are presented on the CMIP Panel website at http://www.wcrp-climate.org/index.php/wgcm-cmip/about-cmip. All source code and data can also be accessed by contacting the corresponding author Tongwen Wu (twwu@cma.gov.cn).

Author contributions

Tongwen Wu led the BCC-CSM development, and all other co-authors contributed to it. Tongwen Wu, Weihua Jie, Xiaoge Xin, and Jie Zhang designed the reported experiments and carried them out. Tongwen Wu, Laurent Li, Yixiong Lu, Junchen Yao, and Fanghua Wu wrote the final document with contributions from all other authors.

Competing interests

The authors declare that they have no conflict of interest.

Acknowledgements

This work was supported by The National Key Research and Development Program of China (2016YFA0602100).

References:

Adler, R. F., Chang, A.: The Version 2 Global Precipitation Climatology Project (GPCP) Monthly Precipitation Analysis (1979-Present), J. Hydrometeor., 4, 1147–1167, 2003.

Bacmeister, J. T., Wehner, M. F., Neale, R. B., Gettelman, A., Hannay, C. E., Lauritzen, P. H., Caron, J. M., and Truesdale, J. E.: Exploratory high-resolution climate simulations using the Community Atmosphere Model (CAM), J. Climate, 27, 3073–3099, doi:10.1175/JCLI-D-13-00387.1, 2014.

Bates, J. R., Moorthi, S., and Higgins, R. W.: A global multilevel atmospheric model using a vector semi-Lagrangian finite difference scheme. Part I: Adiabatic formulation. Mon. Wea. Rev., 121, 244–263, 1993.

Bell, R. J., Strachan, J., Vidale, P. L., Hodges, K. I., and Roberts, M.: Response of tropical cyclones to idealized climate change experiments in a global high resolution coupled general circulation model, J. Climate, 26, 7966–7980, 2013.

Beres, J. H., Alexander, M. J., and Holton, J. R.: A method of specifying the gravity wave spectrum above convection based on latent heating properties and background wind, J. Atmos. Sci., 61, 324-337, 2004.

Birch, C. E., Marsham, J. H., Parker, D. J., and Taylor, C. M.: The scale dependence and structure of convergence fields preceding the initiation of deep convection, Geophys. Res. Lett., 41, 4769–4776, doi:10.1002/2014GL060493, 2014.

Bretherton, C. S. and Park, S.: A new moist turbulence parameterization in the Community Atmosphere Model, J. Climate, 22, 3422-3448, 2009.

Bretherton, C. S. and Wyant, M. C.: Moisture transport, lower tropospheric stability, and decoupling of cloud-topped boundary layers, J. Atmos. Sci., 54, 148-167, 1997.

Burgers, G., and Stephenson D. B.: The “normality” of El Niño, Geophys. Res. Lett., 26, 1027–1039, doi:10.1029/1999GL900161, 1999.

Charlton-Perez, A.J., Baldwin, M.P., Birner T. et al: On the lack of stratospheric dynamical variability in low-top versions of the CMIP5 models. J Geophys Res Atmos, 118, 2494–2505. doi:10.1002/jgrd.50125, 2013.

Collins, W. D., Rasch, P.J., Boville, B.A., Hack, J. J., McCaa, J.R., Williamson, D. L., Kiehl, J. T., Briegleb, B., Bitz C., Lin S.J., Zhang, M.H., and Dai, Y.J.: Description of the NCAR community atmosphere model (CAM3). Technical Report NCAR/TN-464 + STR, National Center for Atmospheric Research, Boulder, Colorado, 226 pp, 2004.

Davis, C. A.: Resolving tropical cyclone intensity in models. Geophysical Research Letters, 45, 2082–2087. https://doi.org/10.1002/2017GL076966, 2018.

Delworth, T. L., Rosati, A., Anderson,W., Adcroft, A. J., Balaji, V., Benson, R., Dixon, K., Griffies, S. M., Lee, H.-C., Pacanowski, R. C., Vecchi, G. A., Wittenberg, A. T., Zeng, F., and Zhang, R.: Simulated climate and climate change in the GFDL CM2.5 high resolution coupled climate model, J. Climate, 25, 2755–2781, doi:10.1175/JCLI-D-11-00316.1, 2012.

Danabasoglu, G., McWilliams, J. C.: Sensitivity of the global ocean circulation to parameterizations of mesoscale tracer transports. Journal of Climate 8, 2967–2987, 1995.

Danabasoglu, G., and Co-authors: North Atlantic simulations in Coordinated Ocean-ice Reference Experiments phase II (CORE-II). Part I: Mean States. Ocean Modelling, 73, 76-107, doi: 10.1016/j.ocemod.2013.10.005, 2014.

Delworth, T. L., Broccoli, A. J., Rosati, A., Stouffer, R. J., Balaji, V., Beesley, J. A., et al.: GFDL's CM2 global coupled climate models. Part I: Formulation and simulation characteristics. J. Climate, 19, 643–674, doi:10.1175/JCLI3629.1, 2006.

Demory, M.-E., Vidale, P.-L., Roberts, M., Berrisford, P., Strachan, J., Schiemann, R., and Mizielinski, M. S.: The role of horizontal resolution in simulating drivers of the global hydrological cycle, Clim. Dynam., 42, 2201–2225, doi:10.1007/s00382-013-1924-4, 2014.

Doi, T., Vecchi, G. A., Rosati, A. J., and Delworth, T. L.: Biases in the Atlantic ITCZ in seasonal–interannual variations for a coarse- and a high-resolution coupled climate model, J. Climate, 25, 5494–5511, doi:10.1175/JCLI-D-11-00360.1, 2012.

de la Vara, A., Cabos, W., Sein, D.V., Sidorenko, D., Koldunov, N.V., Koseki, S., Soares, P. M. M., Danilov, S.: On the impact of atmospheric vs oceanic resolutions on the representation of the sea surface temperature in the South Eastern Tropical Atlantic. Clim. Dyn., 54, 4733–4757, https://doi.org/10.1007/s00382-020-05256-9, 2020.

Dey, C.: Noise suppression in a primitive equation prediction model. Mon. Wea. Rev., 106, 159–173, 1978.

Endo, H., Kitoh, A., Ose, T., Mizuta, R., and Kusunoki, S.: Future changes and uncertainties in Asian precipitation simulated by multiphysics and multi-sea surface temperature ensemble experiments with high-resolution Meteorological Research Institute atmospheric general circulation models (MRI-AGCMs). J. Geophys. Res. Atmos., 117, D16118, doi:10.1029/2012JD017874, 2012.

Eyring, V., Bony, S., Meehl, G. A., Senior, C. A., Stevens, B., Stouffer, R. J., and Taylor, K. E.: Overview of the Coupled Model Intercomparison Project Phase 6 (CMIP6) experimental design and organization, Geosci. Model Dev., 9, 1937-1958, doi:10.5194/gmd-9-1937-2016, 2016.

Flato, G., Marotzke, J., Abiodun, B., Braconnot, P., Chou, S.C., Collins, W., Cox, P., Driouech, F., Emori, S., Eyring, V., Forest, C., Gleckler, P., Guilyardi, E., Jakob, C., Kattsov, V., Reason C. and Rummukainen M.: Evaluation of climate models; in Climate Change 2013: The Physical Science Basis (Contribution of Working Group I to the Fifth Assessment Report of the Intergovernmental Panel on Climate Change), (ed.) T.F. Stocker, D. Qin, G.-K. Plattner, M. Tignor, S.K. Allen, J. Boschung, A. Nauels, Y. Xia, V. Bex and P.M. Midgley; Cambridge University Press, Cambridge, United Kingdom and New York, NY, USA, p. 741–866. 2013.

Fleming, E.L., Chandra, S., Barnett, J.J., and Corney M.: Zonal mean temperature, pressure, zonal wind, and geopotential height as functions of latitude, COSPAR International Reference Atmosphere: 1986, Part II: Middle Atmosphere Models, Adv. Space Res., 10, 12, 11-59, doi:10.1016/0273-1177(90)90386-E, 1990.

Fox-Kemper, B., Danabasoglu, G., Ferrari, R., Griffies, S. M., Hallberg, R. W., Holland, M., Peacock, S., and Samuels, B.: Parameterization of mixed layer eddies. III: Global implementation and impact on ocean climate simulations. Ocean Modelling 39, 61–78, 2011.

Fox-Kemper, B., Ferrari, R., and Hallberg, R.: Parameterization of mixed layer eddies. I: Theory and diagnosis. Journal of Physical Oceanography, 38, 1145–1165, 2008.

Fyfe, J.C., Meehl, G.A., England, M.H., Mann, M. E. Santer, B. D., Flato, G. M., Hawkins, E., Gillett, N. P., Xie, S.–P., Kosaka, Y., Swart, N. C.: Making sense of the early-2000s warming slowdown, Nat. Clim. Change 6, 224–228, 2016.

Garcia, R.R., and Richter, J.H.: On the momentum budget of the quasi-biennial oscillation in the whole atmosphere community climate model, J. Atmos. Sci., 76, 69-87, 2019.

Geller, M.A., Zhou, T., Shindell, D., Ruedy, R., Aleinov, I., Nazerenko, L., et al.: Modeling the QBO – Improvements resulting from higher-model vertical resolution, J. Adv. Model. Earth Syst., 8, 1092-1105, 2016.

~~Good, S.A., Martin, M.J., and Rayner, N.A.: EN4: quality controlled ocean temperature and salinity profiles and monthly objective analyses with uncertainty estimates, Journal of Geophysical Research: Oceans, 118, 6704-6716, doi:10.1002/2013JC009067, 2013.~~

Griffies, S. M.: Elements of the Modular Ocean Model (MOM), GFDL Ocean Group Technical Report No. 7, NOAA/Geophysical Fluid Dynamics Laboratory, 620pp., 2012.

Griffies, S. M., Gnanadesikan, A., Pacanowski, R. C., Larichev, V., Dukowicz, J. K., and Smith, R. D.: Isoneutral diffusion in a z-coordinate ocean model. Journal of Physical Oceanography 28, 805–830, 1998.

Griffies, S. M., Gnanadesikan, A., Dixon, K. W., Dunne, J. P., Gerdes, R., Harrison, M. J., Rosati, A., Russell, J. L., Samuels, B. L., Spelman, M. J., Winton, M., and Zhang, R.: Formulation of an ocean model for global climate simulations. Ocean Science, 1(1), 45–79, doi:10.5194/os-1-45-2005, 2005.

Haarsma, R. J., Roberts, M. J., Vidale, P. L., Senior, C. A., Bellucci, A., Bao, Q., Chang, P., Corti, S., Fučkar, N. S., Guemas, V., von Hardenberg, J., Hazeleger, W., Kodama, C., Koenigk, T., Leung, L. R., Lu, J., Luo, J.-J., Mao, J., Mizielinski, M. S., Mizuta, R., Nobre, P., Satoh, M., Scoccimarro, E., Semmler, T., Small, J., and von Storch, J.-S.: High Resolution Model Intercomparison Project (HighResMIP v1.0) for CMIP6, Geosci. Model Dev., 9, 4185–4208, doi:10.5194/gmd-9-4185-2016, 2016.

Haarsma, R., Acosta, M., Bakhshi, R., Bretonnière, P.-A., Caron, L.-P., Castrillo, M., Corti, S., Davini, P., Exarchou, E., Fabiano, F., Fladrich, U., Fuentes Franco, R., García-Serrano, J., von Hardenberg, J., Koenigk, T., Levine, X., Meccia, V. L., van Noije, T., van den Oord, G., Palmeiro, F. M., Rodrigo, M., Ruprich-Robert, Y., Le Sager, P., Tourigny, E., Wang, S., van Weele, M., and Wyser, K.: HighResMIP versions of EC-Earth: EC-Earth3P and EC-Earth3P-HR – description, model computational performance and basic validation, Geosci. Model Dev., 13, 3507–3527, https://doi.org/10.5194/gmd-13-3507-2020, 2020.

Hack, J. J.: Parameterization of moist convection in the National Center for

Atmospheric Research Community Climate Model (CCM2), J. Geophys. Res., 99, 5551-5568, 1994.

Harris, I.C., and Jones, P.D.: CRU TS4.01: Climatic Research Unit (CRU) Time-Series (TS) version 4.01 of high-resolution gridded data of month-by-month variation in climate (Jan. 1901–Dec. 2016). Cent. Environ.Data Anal., http://dx.doi.org/10.5285/58a8802721c94c66ae45c3baa4d814d0, 2017.

~~Harris, I. C., Jones, P. D., Osborn, T. J., and Lister, D. H.: Updated high-resolution grids of monthly climatic observations – the CRU TS3.10 dataset. Int. J. Climatol., 34, 623–642, doi:10.1002/joc.3711, 2013.~~

Hayashi, M., Jin, F.F., Stuecker, M.F.: Dynamics for El Niño-La Niña asymmetry constrain equatorial-Pacific warming pattern, Nat Commun, 11, 4230, https://doi.org/10.1038/s41467-020-17983-y, 2020.

Hwang, Y.-T. and Frierson, D. M. W.: Link between the double-Intertropical Convergence Zone problem and cloud biases over the Southern Ocean, P. Natl. Acad. Sci. USA, 110, 4935–4940, doi:10.1073/pnas.1213302110, 2013.

Hersbach, H., and D. Dee: ERA5 reanalysis is in production. ECMWF Newsletter, No. 147, ECMWF, Reading, United Kingdom, 7, 2016. http://www.ecmwf.int/sites/default/files/elibrary/2016/16299-newsletter-no147-spring-2016.pdf

Hertwig, E., von Storch, J.-S., Handorf, D., Dethloff, K., Fast, I., and Krismer, T.: Effect of horizontal resolution on ECHAM6-AMIP performance, Clim. Dynam., 45, 185–211, doi:10.1007/s00382-014-2396-x, 2015.

Hewitt, H.T., Roberts, M.J., Hyder, P., Graham, T., Rae, J., Belcher, S.E., Bourdallé-Badie, R., Copsey, D., Coward, A., Guiavarch, C., Harris, C., Hill, R., Hirschi, J. J.-M., Madec, G., Mizielinski, M. S., Neininger, E., New, A. L., Rioual, J.-C., Sinha, B., Storkey, D., Shelly, A., Thorpe, L., and Wood, R. A.: The impact of resolving the Rossby radius at mid-latitudes in the ocean: results from a high-resolution version of the Met Office GC2 coupled model. Geosci. Model Dev. 9, 3655–3670, https://doi.org/10.5194/gmd-9-3655-2016, 2016.

Holtslag, A. A. M., and Boville, B. A.: Local versus nonlocal boundary-layer diffusion in a glocal climate model, J. Climate, 6, 1825-1842, 1993.

Huffman, G. J., Bolvin, D. T., Braithwaite, D., Hsu, K., Joyce, R., Kidd, C., Nelkin, E.J., Sorooshian, S., Tan, J., and Xie, P.: NASA Global Precipitation Measurement (GPM) Integrated Multi-satellitE Retrievals for GPM (IMERG), Algorithm Theoretical Basis Document (ATBD) Version 06, 2019.

Ji, J.: A climate-vegetation interaction model: Simulating physical and biological processes at the surface, Journal of Biogeography, 22, 2063-2069, 1995.

Ji, J., Huang, M., and Li, K.: Prediction of carbon exchange between China terrestrial ecosystem and atmosphere in 21st century, Sci. China Ser. D: Earth Sci., 51(6), 885-898, 2008.

Jie, W., Zhang, J., Wu, T., Shi, X., Zhang, F., Li, J., Chu, M., Liu, Q., Yan, J., Ma, Q., Wei, M.: BCC BCC-CSM2HR model output prepared for CMIP6 HighResMIP hist-1950. Version YYYYMMDD[1], Earth System Grid Federation. https://doi.org/10.22033/ESGF/CMIP6.2921, 2020.

Jones, P.D., Lister, D.H., Osborn, T.J., Harpham, C., Salmon, M. and Morice, C.P.: Hemispheric and large-scale land surface air temperature variations: an extensive revision and an update to 2010. Journal of Geophysical Research 117, D05127. doi: 10.1029/2011JD017139, 2012.

Knapp, K. R., Kruk, M. C., Levinson, D. H., Diamond, H. J., and Neumann, C. J.: The International Best Track Archive for Climate Stewardship (IBTrACS): Unifying Tropical Cyclone Data. Bull. Amer. Meteor. Soc., 91, 363–376, https://doi.org/10.1175/2009BAMS2755.1, 2010.

Kim, H., Caron, J. M., Richter, J. H., and Simpson, I. R.: The lack of QBO - MJO connection in CMIP6 models. Geophysical Research Letters, 47, e2020GL087295, doi:10.1029/2020GL087295, 2020.

Kinter, J.L., Cash, B., Achuthavarier, D., Adams, J., Altshuler, E., Dirmeyer, P., Doty, B., Huang, B., Jin, E.K., Marx, L., Manganello, J., Stan, C., Wakefield, T., Palmer, T., Hamrud, M., Jung, T., Miller, M., Towers, P., Wedi, N., Satoh, M., Tomita, H., Kodama, C., Nasuno, T., Oouchi, K., Yamada, Y., Taniguchi, H., Andrews, P., Baer, T., Ezell, M., Halloy, C., John, D., Loftis, B., Mohr, R., and Wong, K.: Revolutionizing Climate Modeling with Project Athena: A Multi-Institutional, International Collaboration. Bull. Amer. Meteor. Soc., 94, 231–245, https://doi.org/10.1175/BAMS-D-11-00043.1, 2013.

Klein, S. A. and Hartmann, D. L.: The seasonal cycle of low stratiform cloud, J. Climate, 6, 1587-1606, 1993.

Lal, M., Cubasch, U., Perlwitz, J. P., and Waszkewitz, J.: Simulation of the Indian monsoon climatology in ECHAM3 climate model: Sensitivity to horizontal resolution, Int. J. Climatol., 17, 847–858, 1997.

Large, W., McWilliams, J., and Doney, S.: Oceanic vertical mixing: a review and a model with a nonlocal boundary layer parameterization. Reviews of Geophysics 32, 363–403, 1994.

Li, G., and Xie, S.-P.: Tropical biases in CMIP5 multimodel ensemble: The excessive equatorial Pacific cold tongue and double ITCZ problems, J. Climate, 27, 1765–1780, 2014.

Li, W., Zhang, Y., Shi, X., Zhou, W., Huang, A., Mu, M., Qiu, B., and Ji, J.: Development of the Land Surface Model BCC_AVIM2.0 and Its Preliminary Performance in LS3MIP/CMIP6, J. Meteor. Res., 33, 851–869, https://doi.org/10.1007/s13351-019-9016-y, 2019.

Li, H., and Sriver, R.L.: Tropical Cyclone Activity in the High‐Resolution Community Earth System Model and the Impact of Ocean Coupling, Advances in Modeling Earth Systems, 10, 165–186, https://doi.org/10.1002/2017MS001199, 2018.

Liebmann, B., and Smith, C.A.: Description of a Complete (Interpolated) Outgoing Longwave Radiation Dataset. Bulletin of the American Meteorological Society, 77, 1275-1277, 1996.

Loeb, N. G., Doelling, D. R., Wang, H., Su, W., Nguyen, C., Corbett, J. G., Liang, L., Mitrescu, C., Rose, F. G., Kato, S.: Clouds and the Earth's Radiant Energy System (CERES) Energy Balanced and Filled (EBAF) Top-of-Atmosphere (TOA) Edition-4.0 data product, J. Climate, 31, 895-918, doi:

10.1175/JCLI-D-17-0208.1, 2018.

Lu, Y., Wu, T., Jie, W., Scaife, A. A., Andrews, M. B., and Richter, J. H.: Variability of the Stratospheric Quasi-Biennial Oscillation and Its Wave Forcing Simulated in the Beijing Climate Center Atmospheric General Circulation Model. J.Atmos.Sci., 77, 149-165, doi:10.1175/JAS-D-19-0123.1, 2020a.

Lu, Y., Wu, T., Li, Y., and Yang, B.: Mitigation of the double ITCZ syndrome in BCC-CSM2-MR through improving parameterizations of boundary-layer turbulence and shallow convection, Geosci. Model Dev. Discuss., https://doi.org/10.5194/gmd-2020-40, in review, 2020b.

Madden, R. A. and Julian, P. R.: Detection of a 40–50 Day Oscillation in the Zonal Wind in the Tropical Pacific, J. Atmos. Sci., 28, 702–708, 1971.

Martin, G. M.: The simulation of the Asian summer monsoon, and its sensitivity to horizontal resolution, in the UK meteorological office unified model, Q. J. Roy. Meteor. Soc., 125, 1499–1525, doi:10.1002/qj.49712555703, 1999.

Manganello, J. V., Hodges, K. I., Kinter, J. L., Cash, B. A., Marx, L., Jung, T., Achuthavarier, D., Adams, J. M., Altshuler, E. L.,Huang, B., Jin, E. K., Stan, C., Towers, P., and Wedi, N.: Tropical Cyclone Climatology in a 10-km Global Atmospheric GCM: Toward Weather-Resolving Climate Modeling, J. Climate, 25, 3867–3893, doi:10.1175/JCLI-D-11-00346.1, 2012.

Manizza, M., Le Quere, C., Watson, A. J., and Buitenhuis, E. T.: Bio-optical feedbacks among phytoplankton, upper ocean physics and sea-ice in a global model. Geophys. Res. Lett., 32, L05603, 2005.

Marshall, J., Hill, C., Perelman, L., Adcroft, A.: Hydrostatic, quasi-hydrostatic, and nonhydrostatic ocean modeling. Journal of Geophysical Research, 102, 5733–5752, 1997.

Medhaug, I., Martin, B. S., Erich, M. F., and Knutti, R.: Reconciling controversies about the ‘global warming hiatus’, Nature, 545, 41–47, 2017.

Morel, A., and Antoine, D.: Heating rate within the upper ocean in relation to its bio-optical state, Journal of Physical Oceanography, 24, 1652-1665, 1994.

Masson, S., Terray, P., Madec, G., Luo, J.-J., Yamagata, T., and Takahashi, K.:

Impact of intra-daily SST variability on ENSO characteristics in a coupled model, Clim. Dynam., 39, 681–707, 2012.

Masumoto, Y., Sasaki, H., Kagimoto, T., Komori, N., Ishida, A., Sasai, Y., Miyama, T., Motoi, T., Mitsudera, H., Takahashi, K., Sakuma, H., and Yamagata, T.: A fifty-year eddy-resolving simulation of the world ocean – Preliminary outcomes of OFES (OGCM for the Earth Simulator), J. Earth Sim., 1, 35–56, 2004.

McFarlane, N. A.: The effect of orographically excited gravity wave drag on the general circulation of the lower stratosphere and troposphere, J. Atmos. Sci., 44, 1775-1800, 1987.

Mizielinski, M. S., Roberts, M. J., Vidale, P. L., Schiemann, R., Demory, M.-E., Strachan, J., Edwards, T., Stephens, A., Lawrence, B. N., Pritchard, M., Chiu, P., Iwi, A., Churchill, J., del Cano Novales, C., Kettleborough, J., Roseblade, W., Selwood, P., Foster, M., Glover, M., and Malcolm, A.: High-resolution global climate modelling: the UPSCALE project, a large-simulation campaign, Geosci. Model Dev., 7, 1629–1640, 2014.

Mizuta, R., Oouchi, K., Yoshimura, H., Noda, A., Katayama, K., Yukimoto, S., Hosaka, M., Kusunoki, S., Kawai, H., and Nakagawa, M.: 20-km-Mesh Global Climate Simulations Using JMAGSMModel: -Mean Climate States-, J. Meteorol. Soc. Jpn., 84, 165–185, 2006.

Murakami, H.: Tropical cyclones in reanalysis data sets. Geophysical Research Letters, 41, 2133-2141, 2014

Murakami, H., Vecchi, G. A., Underwood, S., Delworth, T. L.,Wittenberg, A. T., Anderson,W. G., Chen, J.-H., Gudgel, R. G., Harris, L. M., Lin, S.-J., and Zeng, F.: Simulation and Prediction of Category 4 and 5 Hurricanes in the High-Resolution GFDL HiFLOR Coupled Climate Model, J. Climate, 28, 9058–9079, 2015.

Murakami, H., Wang, Y., Yoshimura, H., Mizuta, R., Sugi, M., Shindo, E., Adachi, Y., Yukimoto, S., Hosaka, M., Kusunoki, S., Ose, T., and Kitoh, A.: Future Changes in Tropical Cyclone Activity Projected by the New High-Resolution MRI-AGCM, J. Climate, 25, 3237–3260, doi:10.1175/JCLI-D-11-00415.1, 2012.

Nicholls, S. and Turton, J. D.: An observational study of the structure of stratiform cloud sheets: Part II. Entrainment. Quart. J. Roy. Meteor. Soc., 112, 461-480, 1986.

Ohfuchi, W., Nakamura, H., Yoshioka, M. K., Enomoto, T., Takaya, K., Peng, X., Yamane, S., Nishimura, T., Kurihara, Y., and Ninomiya, K.: 10-km mesh meso-scale resolving simulations of the global atmosphere on the Earth Simulator: Preliminary outcomes of AFES (AGCM for the Earth Simulator), Journal of the Earth Simulator, 1, 8–34, 2004.

Oleson, K.W., Dai, Y., Bonan, G., Bosilovich, M., Dickinson, R., Dirmeyer, P., Hoffman, F., Houser, P., Levis, S., Niu, G.-Y., Thornton, P., Vertenstein, M., Yang, Z.-L., and Zeng, X.: Technical description of the Community Land Model (CLM). NCAR Tech. Note TN-461 + STR, 174 pp, 2004

Oouchi, K., Yoshimura, J., Yoshimura, H., Mizuta, R., Kusunoki, S., and Noda, A.: Tropical Cyclone Climatology in a Global-Warming Climate as Simulated in a 20 km-Mesh Global Atmospheric Model: Frequency and Wind Intensity Analyses, J. Meteorol. Soc. Japan., 84, 259–276, 2006.

Park, S., and Bretherton, C. S.: The University of Washington shallow convection and moist turbulence schemes and their impact on climate simulations in the Community Atmosphere Model, J. Climate, 22, 3449-3469, 2009.

Peatman, S. C., Matthews, A. J., and Stevens, D. P.: Propagation of the Madden–Julian Oscillation and scale interaction with the diurnal cycle in a high-resolution GCM, Clim. Dynam., 45, 2901–2918, doi:10.1007/s00382-015-2513-5, 2015.

Rackow, T., Goessling, H. F., Jung, T., Sidorenko, D., Semmler, T., Barbi, D., and Handorf, D.: Towards multi-resolution global climate modeling with ECHAM6-FESOM, Part II: climate variability, Clim. Dynam., 1–26, doi:10.1007/s00382-016-3192-6, 2016.

Rasch, P. J., and Kristj ánsson, J. E.: A comparison of the CCM3 model climate using diagnosed and predicted condensate parameterizations, J. Climate, 11, 1587-1614, 1998.

Rayner, N. A., Parker, D. E., Horton, E. B., Folland, C. K., Alexander, L. V., Rowell,

D. P., Kent, E. C., and Kaplan, A.: Global analyses of sea surface temperature, sea ice, and night marine air temperature since the late nineteenth century J. Geophys. Res.Vol. 108, No. D14, 4407, doi:10.1029/2002JD002670, 2003.

Reed, K. A., Bacmeister, J. T., Wehner, Rosenbloom, N. A., F., M., Bates, S. C., Lauritzen, P. H., Truesdale, J. T., and Hannay, C.: Impact of the dynamical core on the direct simulation of tropical cyclones in a high-resolution global model, Geophys. Res. Lett.,42, GL063974, doi:10.1002/2015GL063974, 2015.

Richter, I.: Climate model biases in the eastern tropical oceans: Causes, impacts and ways forward. Wiley Interdisciplinary Reviews: Climate Change, 6(3), 345 – 358. doi:10.1002/wcc.338, 2015.

Richter, J.H., Sassi, F., and Garcia, R.R.: Toward a physically based gravity wave source parameterization in a general circulation model, J. Atmos. Sci., 67, 136-156, 2010.

Roberts, C. D., Senan, R., Molteni, F., Boussetta, S., Mayer, M., and Keeley, S. P.E.: Climate model configurations of the ECMWF Integrated Forecasting System (ECMWF-IFS cycle 43r1) for HighResMIP, Geosci. Model.Dev., 11, 3681-3721, 2018.

Roberts, M. J., Baker, A., Blockley, E. W., Calvert, D., Coward, A., Hewitt, H. T., Jackson, L. C., Kuhlbrodt, T., Mathiot, P., Roberts, C. D., Schiemann, R., Seddon, J., Vannière, B., and Vidale, P. L.: Description of the resolution hierarchy of the global coupled HadGEM3-GC3.1 model as used in CMIP6 HighResMIP experiments, Geosci. Model Dev., 12, 4999–5028, https://doi.org/10.5194/gmd-12-4999-2019, 2019.

Roberts, M. J., Hewitt, H. T., Hyder, P., Ferreira, D., Josey, S. A., Mizielinski, M., and Shelly, A.: Impact of ocean resolution on coupled air-sea fluxes and large-scale climate. Geophysical Research Letters, 43(19), 10,430-10,438. https://doi.org/10.1002/2016GL070559, 2016.

Sakamoto, T. T., Komuro, Y., Nishimura, T., Ishi, M., Tatebe, H., Shiogama, H., Hasegawa, A., Toyoda, T., Mori, M., Suzuki, T., Imada, Y., Nozawa, T., Takata, K., Mochizuki, T., Ogochi, K., Emori, S., Hasumi, H., and Kimoto, M.:

MIROC4h –A New High-Resolution Atmosphere-Ocean Coupled General Circulation Model, J. Meteorol. Soc. Japan, 90, 325–359, 2012.

Sato, T., Miura, H., Satoh, M., Takayabu, Y. N., and Wang, Y. Q.: Diurnal cycle of precipitation in the tropics simulated in a global cloud-resolving model, J. Climate, 22, 4809–4826, 2009.

Satoh, M., Tomita, H., Yashiro, H., Miura, H., Kodama, C., Seiki, T., Noda, A. T., Yamada, Y., Goto, D., Sawada, M., Miyoshi, T., Niwa, Y., Hara, M., Ohno, Y., Iga, S., Arakawa, T., Inoue, T., and Kubokawa, H.: The Non-hydrostatic Icosahedral Atmospheric Model: Description and development, Progress in Earth and Planetary Science, 1, 1, doi:10.1186/s40645-014-0018-1, 2014.

Schenzinger, V., Osprey, S., Gray, L., and Butchart, N.: Defining metrics of the Quasi-Biennial Oscillation in global climate models, Geosci. Model Dev., 10, 2157–2168, https://doi.org/10.5194/gmd-10-2157-2017, 2017.

Schiemann, R., Demory, M.-E., Mizielinski, M. S.,and Roberts, M. J., Shaffrey, L. C., Strachan, J., and Vidale, P. L.: The sensitivity of the tropical circulation and Maritime Continent precipitation to climate model resolution, Clim. Dynam., 42, 2455–2468, doi:10.1007/s00382-013-1997-0, 2014.

Semtner, A.J.: A model for the thermodynamic growth of sea ice in numerical investigations of climate, J. Phys. Oceanogr., 6, 379–389, 1976.

Shaevitz, D., Camargo, S. J., Sobel, A. H., Jonas, J. A., Kim, D., Kumar, A., LaRow, T. E., Lim, Y.-K., Murakami, H., Reed, K., Roberts, M. J., Scoccimarro, E., Vidale, P. L.,Wang, H.,Wehner, M. F., Zhao, M., and Henderson, N.: Characteristics of tropical cyclones in high-resolution models in the present climate, J. Adv. Model. Earth Syst., 6, 1154–1172, doi:10.1002/2014MS000372, 2014.

Shaffrey, L. C., Stevens, I., Norton, W. A., Roberts, M. J., Vidale, P. L., Harle, J. D., Jrrar, A., Stevens, D. P., Woodage, M. J., Demory, M. E., Donners, J., Clark, D. B., Clayton, A., Cole, J. W., Wilson, S. S., Connolley, W. M., Davies, T. M., Iwi, A. M., Johns, T. C., King, J. C., New, A. L., Slingo, J. M., Slingo, A., Steenman-Clark, L., and Martin, G. M.: UK HiGEM: the new UK High-resolution Global Environment Model – model description and basic evaluation, J. Climate, 22, 1861–1896, doi:10.1175/2008JCLI2508.1, 2009.

Shi, Q., and Wang, G.: ObservedWarm Filaments from the Kuroshio Associated with Mesoscale Eddies, Remote Sens., 12, 3090, doi:10.3390/rs12183090, 2020.

Small, R. J., Curchitser, E., Hedstrom, K., Kauffman, B., and Large, W. G.: The Benguela upwelling system: Quantifying the sensitivity to resolution and coastal wind representation in a global climate model, J. Climate, 28, 9409–9432, doi:10.1175/JCLI-D-15-0192.1, 2015.

Small, R. J., Bacmeister, J., Bailey, D. A., Baker, A., Bishop, S., Bryan, F. O., Caron, J., Dennis, J., Gent, P. R., Hsu, H.-M., Jochum, M., Lawrence, D. M., Munoz Acevedo, E., diNezio, P., Scheitlin, T., Tomas, R., Tribbia, J., Tseng, Y., and Vertenstein, M.: A new synoptic scale resolving global climate simulation using the Community Earth System Model. J. Adv.Model. Earth Syst., 6, 1065–1094, https://doi.org/10.1002/2014MS000363, 2014.

Smith, R. D., Maltrud, M. E., Bryan, F. O., and Hecht, M. W.: Numerical Simulation of the North Atlantic Ocean at 1/10°, J. Phys. Oceanogr., 30, 1532–1561, 2000.

Sperber, K. R., Sultan, H., Potter, G. L., and Boyle, J. S.: Simulation of the Northern summer monsoon in the ECMWF model: sensitivity to horizontal resolution, Mon. Weather Rev., 122, 2461–2481, 1994.

Stevens, B., Fiedler, S., Kinne, S., Peters, K., Rast, S., Müsse, J., Smith, S. J., and Mauritsen, T.: MACv2-SP: a parameterization of anthropogenic aerosol optical properties and an associated Twomey effect for use in CMIP6, Geosci. Model Dev., 10, 433–452, doi:10.5194/gmd-10-433-2017, 2017.

Strachan, J., Vidale, P. L., Hodges, K., Roberts, M., and Demory, M.-E.: Investigating global tropical cyclone activity with a hierarchy of AGCMs: The role of model resolution, J. Clim., 26, 133–152, 2013.

Sugi, M., Murakami, H., and Yoshida., K.: Projection of future changes in the frequency of intense tropical cyclones. Climate Dynamics, 49(1-2), 619-632, 2017.

Sweby, P. K.: High resolution schemes using flux limiters for hyperbolic conservation laws, SIAM Journal on Numerical Analysis, 21(5), 995-1011, 1984.

Taylor, K. E., Stouffer, R. J., and Meehl, G. A.: An Overview of Cmip5 and the Experiment Design, B. Am. Meteorol. Soc., 93, 485–498, 2012.

Tian, B., Fetzer, E.J., Kahn, B.H., Teixeira, J., Manning, E., and Hearty, T.: Evaluating CMIP5 models using AIRS tropospheric air temperature and specific humidity climatology. J Geophys Res Atmos 118:114–134. doi:10.1029/2012JD018607, 2013.

Turton, J. D., and Nicholls, L.: A study of the diurnal variation of stratocumulus using a multiple mixed-layer model, Q. J. R. Meteorol. Soc., 113, 969-1009, 1987.

Vecchi, G. A., Delworth, T., Murakami, H., Underwood, S., Wittenberg, A. T., Zeng, F., Zhang, W., Baldwin, J. W., Bhatia, K., Cooke, W., He, J., Kapnick, S. B., Knutson, T., Villarini, G., van der Wiel, K., Anderson, W., Balaji, V., Chen, J., Dixon, K., Gudgel, R., Harris, L., Jia, L., Johnson, N., Lin, S., Liu, M., Ng, J., Rosati, A., Smith, J., and Yang., X.: Tropical cyclone sensitivities to CO_2 doubling: Roles of atmospheric resolution, synoptic variability and background climate changes. Climate Dynamics, 53(9), 5999-6033, 2019.

Vellinga, M., Roberts, M., Vidale, P. L., Mizielinski, M., Demory, M.-E., Schiemann, R., Strachan, J., Bain, C., Kettleborough, J., Good, P., Edmond, I., and Hibling, E.: Organised convection as the main carrier of Sahel rainfall variability at multi-annual timescales, Geophys. Res. Lett., 43, 326–333, doi:10.1002/2015GL066690, 2016.

Walsh, K., Lavender, S., Scoccimarro, E., and Murakami, H.: Resolution dependence of tropical cyclone formation in CMIP3 and finer resolution models, Clim. Dynam., 40, 585–599, 2012.

Wehner, M. F., Smith, R. L., Bala, G., and Duffy, P.: The effect of horizontal resolution on simulation of very extreme US precipitation events in a global atmosphere model. Clim. Dyn., 34, 241–247, 2010.

Wehner, M. F., Prabhat, Reed, K. A., Stone, D., Collins, W. D., and Bacmeister, J. T.: Resolution dependence of future tropical cyclone projections of CAM5.1 in the

US CLIVAR Hurricane Working Group idealized configurations, J. Climate, 28, 3905–3925, doi:10.1175/JCLI-D-14-00311.1, 2015.

Wheeler, M. C., and Hendon, H. H.: An all-season real-time multivariate MJO index: Development of an index for monitoring and prediction, Mon. Weather Rev., 132, 1917–1932, 2004.

Wheeler, M., and Kiladis, G. N.: Convectively coupled equatorial waves: Analysis of clouds and temperature in the wavenumber-frequency domain, J. Atmos. Sci., 56, 374– 399, 1999.

Whitehead, J. P., Jablonowski, C., Rood, R. B., and Lauritzen, P.H.: A stability analysis of divergence damping on a latitude–longitude grid. Mon. Wea. Rev., 139, 2976–2993, 2011.

Wielicki, B.A., Barkstrom, B. R., Harrison, E. F., Lee, R. B., Smith, G. L., and Cooper, J. E.: Clouds and the earth's radiant energy system (CERES): an earth observing system experiment, Bull. Am. Meteorol. Soc., 77, 853–868, 1996.

Wood, R. and Bretherton, C. S.: Boundary-layer depth, entrainment, and decoupling in the cloud-capped subtropical and tropical marine boundary layer, J. Climate, 17, 3576-3588, 2004.

Wu, T.: A Mass-Flux Cumulus Parameterization Scheme for Large-sistercale Models: Description and Test with Observations, Clim. Dyn., 38, 725–744, doi:10.1007/ s00382-011-0995-3, 2012.

Wu, T., Hu, A., Gao, F., Zhang, J., and Meehl, G. A.: New insights into natural variability and anthropogenic forcing of global/regional climate evolution, npj Climate and Atmospheric Science, 2:18, https://doi.org/10.1038/s41612-019-0075-7, 2019.

Wu, T., Song, L., Li, W., Wang, Z., Zhang, H., Xin, X., Zhang, Y., Zhang, L., Li, J., Wu, F., Liu, Y., Zhang, F., Shi, X., Chu, M., Zhang, J., Fang, Y., Wang, F., Lu, Y., Liu, X., Wei, M., Liu, Q., Zhou, W., Dong, M., Zhao, Q., Ji, J., Li, L., and Zhou, M.: An overview of BCC climate system model development and application for climate change studies. J. Meteor. Res., 28(1), 34-56, 2014.

Wu, T., Li, W., Ji, J., Xin, X., Li, L., Wang, Z, Zhang, Y., Li, J., Zhang, F., Wei, M., Shi, X., Wu, F., Zhang, L., Chu, M., Jie, W., Liu, Y., Wang, F., Liu, X., Li, Q., Dong, M., Liang, X., Gao, Y., and Zhang, J.: Global carbon budgets simulated by the Beijing climate center climate system model for the last century. J Geophys Res Atmos, 118, 4326-4347. doi: 10.1002/jgrd.50320, 2013.

Wu, T., Yu, R., Zhang, F., Wang, Z., Dong, M., Wang, L., Jin, X., Chen, D., and Li, L.: The Beijing Climate Center atmospheric general circulation model: description and its performance for the present-day climate, Climate Dynamics, 34, 123-147, doi:10.1007/s00382-008-0487-2, 2010.

Wu, T., Lu, Y., Fang, Y., Xin, X., Li, L., Li, W., Jie, W., Zhang, J., Liu, Y., Zhang, L., Zhang, F., Zhang, Y., Wu, F., Li, J., Chu, M., Wang, Z., Shi, X., Liu, X., Wei, M., Huang, A., Zhang, Y., and Liu, X.: The Beijing Climate Center Climate System Model (BCC-CSM): Main Progress from CMIP5 to CMIP6, Geosci. Model Dev., 12, 1573–1600, 2019.

Wu, T., Zhang, F., Zhang, J., Jie, W., Zhang, Y., Wu, F., Li, L., Yan, J., Liu, X., Lu, X., Tan, H., Zhang, L., Wang, J., and Hu, A.: Beijing Climate Center Earth System Model version 1 (BCC-ESM1): model description and evaluation of aerosol simulations, Geosci. Model Dev., 13, 977–1005, doi:10.5194/gmd-13-977-2020, 2020a.

Wu, T., Yu, R., Lu, Y., Jie, W., et al.: Source code for Wu et al, "BCC-CSM2-HR: A High-Resolution Version of the Beijing Climate Center Climate System Model", GMD publication. http://doi.org/10.5281/zenodo.4127457, 2020b.

Wu, T., Yu, R., and Zhang, F.: A modified dynamic framework for atmospheric spectral model and its application, J. Atmos.Sci., 65, 2235-2253, 2008.

Xie, P., and P.A. Arkin: Global precipitation: A 17-year monthly analysis based on gauge observations, satellite estimates, and numerical model outputs. Bull. Amer. Meteor. Soc., 78, 2539 – 2558, 1997.

Xin, X., Wu, T., and Zhang, J.: Introduction of CMIP5 experiments carried out with the climate system models of Beijing Climate Center. Adv. Clim. Change Res., 4(1), 41-49, doi: 10.3724/SP.J.1248.2013.041, 2013.

Xin, X., Wu, T., Zhang, J., Zhang, F., Li, W., Zhang, Y., Lu, Y., Fang, Y., Jie, W., Zhang, L., Dong, M., Shi, X., Chu, M., Liu Q., and Yan, J.: Introduction of BCC models and its participation in CMIP6, Climate Change Research, 15 (5): 533-539, https://doi.org/10.12006/j.issn.1673-1719.2019.039, 2019.

Yamada, Y., Satoh, M., Sugi, M., Kodama, C., Noda, A. T., Nakano, M., and Nasuno, T.: Response of tropical cyclone activity and structure to global warming in a high-resolution global nonhydrostatic model. Journal of Climate, 30, 9703– 9724, 2017.

Yao, J., Zhou, T., Guo, Z., Chen, X.: Improved Performance of High-Resolution Atmospheric Models in Simulating the East Asian Summer Monsoon Rain Belt, J. Climate, 30: 8825–8840, DOI: 10.1175/JCLI-D-16-0372.1, 2017.

Yu, R., Zhou, T., Wu, T., Xue, W., and Zhou, G.: Development and Evaluation of High Resolution Climate System Models, Springer, 258pp, doi:10.1007/978-981-10-0033-1, 2016.

Zarzycki, C. M., Reed, K. A., Bacmeister, J. T., Craig, A. P., Bates, S. C., and Rosenbloom, N. A.: Impact of surface coupling grids on tropical cyclone extremes in high-resolution atmospheric simulations, Geos. Model Dev., 9, 779-788, 2016.

Zhang, M., Lin, W., Bretherton, C. S., Hack, J. J., and Rasch, P. J.: A modified formulation of fractional stratiform condensation rate in the NCAR community atmospheric model CAM2, J. Geophys. Res., 108 (D1), 2003.

Zhang, Y., Gao, Z., Li, D., Li, Y., Zhang, N., Zhao, X., and Chen, J.: On the computation of planetary boundary-layer height using the bulk Richardson number method, Geosci. Model Dev., 7, 2599–2611, 2014.

Zhang L., Zhou, T., Klingaman, N.P., Wu, P., and Roberts, M.: Effect of Horizontal Resolution on the Representation of the Global Monsoon Annual Cycle in AGCMs. Adv. Atmos.Sci., 35, 1003-1020, 10.1007/s00376-018-7273-9. 2018.

Zhao, M., Held, I. M., and Lin, S.-J.: Some counterintuitive dependencies of tropical cyclone frequency on parameters in a GCM, J. Atmos. Sci., 69, 2272-2283, 2012.

Zhao, M., Held, I. M., Lin, S. J., and Vecchi, G. A.: Simulations of Global Hurricane Climatology, Interannual Variability, and Response to Global Warming Using a

50 km Resolution GCM, J.Climate, 33, 6653–6678, 2009.

Zhou, T, Chen, Z., Zou, L., Chen, X., Yu, Y., Wang, B., Bao, Q, Bao, Y., Cao, J., He, B., Hu, S., Li, L., Li, J., Lin, Y., Ma, L., Qiao, F., Rong, X., Song, Z., Tang, Y., Wu, B., Wu, T., Xin, X., Zhang, H., Zhang, M.: Development of climate and earth system models in China: Past achievements and new CMIP6 results. J. Meteor. Res., 34, 1-19, doi: 10.1007/s13351-020-9164-0, 2020.

Table 1. Constituents and configurations of BCC-CSM2-MR and BCC-CSM2-HR.

		BCC-CSM2-MR	BCC-CSM2-HR
Atmosphere component (BCC-AGCM3)	**Resolution**	T106 (~110km), 46 layers with top layer at 1.979hPa and model lid at 1.459 hPa	T266 (~45km), 56 layers with top layer at 0.156 hPa and model lid at 0.092 hPa
	Dynamical core	Spectral framework described in Wu et al. (2008)	Same as in BCC-CSM2-MR but including spatially-varying ~~variant~~ divergence damping.
	Deep convection	A modified Wu'2012 scheme (Wu, 2012) described in Wu et al. (2019)	Revised Wu et al. (2019) scheme, including the effects of convective downdraft in neighboring grids.
	Shallow/Middle Tropospheric Moist Convection	Hack (1994)	Modified Hack (1994) scheme described in Lu et al. (2020b), incorporating a trigger based on lower tropospheric stability.
	Cloud macrophysics	Diagnosed cloud fraction described in Wu et al. (2019)	Revised Wu et al. (2019) scheme, excluding the special treatment for the marine stratocumulus.
	Cloud microphysics	Modified scheme of Rasch and Kristj´ansson (1998) by Zhang et al. (2003), but included the aerosol indirect effects in which liquid cloud droplet number concentration is diagnosed using the aerosols masses.	Same as in BCC-CSM2-MR.
	Gravity wave drag	Gravity wave drag generated by both orography (Mcfarlane 1987) and convection (Beres et al., 2004).	Same as in BCC-CSM2-MR, but using tuned parameters related to model resolutions.
	Surface orographic drag	No treatment.	The turbulent mountain stress scheme as in Richter et al. (2010).
	Radiative transfer	Radiative transfer scheme used in CAM3 (Collins et al., 2004), but including the aerosol indirect effects, and the effective radius of the cloud droplet for liquid clouds is diagnosed using liquid cloud droplet number concentration.	Same as in BCC-CSM2-MR.
	Boundary Layer	Parameterization of Holtslag and Boville (1993), but modified PBL height computation as in Zhang et al. (2014)	The University of Washington Moist Turbulence scheme (Bretherton and Park, 2009)
Land surface component (BCC-AVIM2)	**Resolution**	Horizontal resolution same as in the atmosphere component. 10 layers for soil and up to five layers for snow.	Horizontal resolution same as in the atmosphere component. 10 layers for soil and up to five layers for snow.
	Biophysical process	CLM3 (Oleson et al., 2004)	CLM3 (Oleson et al., 2004)
	Plant physiological and Soil carbon-nitrogen dynamical processes	BCC-AVIM2 (Li et al., 2019)	BCC-AVIM2 (Li et al., 2019)
Ocean Component (MOM)	**Resolution**	1°×1° with a tri-pole grid, but 1/3° latitude between 30°S and 30°N to 1.0° at 60° latitude, 40 layers in vertical	1/4°×1/4° with a tri-pole grid at north to 60°N, 50 layers in vertical
	Tracer advection scheme	MOM4 (Griffies, 2005), Sweby advection scheme (Sweby, 1984)	MOM5 (Griffies, 2012), multi-dimensional piecewise parabolic method
	Neutral diffusion scheme	Griffies et al. (1998) with a constant diffusivity of 600 $m^2 s^{-1}$	None
	Surface boundary layer processes	K-profile parameterization (KPP, Large et al., 1994)	Same as in MOM4
	Submesoscale parameterization	None	Fox-Kemper et al. (2008)

	scheme		
	shortwave penetration	Morel and Antoine (1994), with the maximum depth of 100m	Manizza et al. (2005), with the maximum depth of 300m
Sea Ice Component (SIS)	**Resolution**	Same as in the ocean component MOM4, 3 vertical layers including 1 snow cover and 2 ice layers of equal thickness	Same as in the ocean component MOM5, 3 vertical layers including 1 snow cover and 2 ice layers of equal thickness
	Model physics	SIS4 (Winton, 2000)~~v1~~, – Elastic-viscous-plastic dynamical processes, Semtner's thermodynamic processes	SIS5 ~~Same as SISv2~~(Delworth et al., 2006), Elastic-viscous-plastic dynamical processes, Semtner's thermodynamic processes
	Snow albedo	0.80	0.85
	Ice albedo	0.5826	0.68

Table 2. Energy balance and cloud radiative forcing at the top-of-atmosphere (TOA) in the models with contrast to CERES-EBAF observations. Units: W m^{-2}.

	BCC-CSM2-MR	BCC-CSM2-HR	CERES-EBAF
Net energy at TOA	2.12 ±0.40~~1.81 ±0.49~~	1.51 ±0.57~~1.08 ±0.46~~	0.84 ±0.33
TOA outgoing longwave radiative flux	239.18 ±0.20~~239.13 ±0.29~~	237.85 ±0.18~~238.52 ±0.35~~	239.69 ±0.25
TOA net shortwave radiative flux	241.29 ±0.35~~240.95 ±0.55~~	239.35 ±0.49~~239.60 ±0.45~~	240.53 ±0.19
TOA outgoing longwave radiative flux in clear sky	265.10 ±0.20~~265.05 ±0.41~~	265.28 ±0.22~~266.12 ±0.46~~	265.67 ±0.37
TOA net shortwave radiative flux in clear sky	291.13 ±0.25~~290.52 ±0.85~~	290.06 ±0.15~~289.77 ±0.70~~	287.68 ±0.14
TOA incoming shortwave radiation	340.34 ±0.09~~340.38 ±0.09~~	340.35 ±0.09~~340.38 ±0.09~~	340.14 ±0.09
Shortwave cloud radiative forcing	-49.83 ±0.27~~-49.58 ±0.49~~	-50.71 ±0.48~~-50.17 ±0.58~~	-47.16 ±0.24
Longwave cloud radiative forcing	25.92 ±0.08~~25.92 ±0.19~~	27.43 ±0.11~~27.60 ±0.19~~	25.99 ±0.25

Notes: Mean value and standard deviation are calculated from 2001-2014 yearly global means of the ~~1971-2000~~ simulations for BCC-CSM2-MR, BCC-CSM2-HR, and the ~~2001-2014~~ CERES-EBAF Ed4.1~~2.8~~ data set.

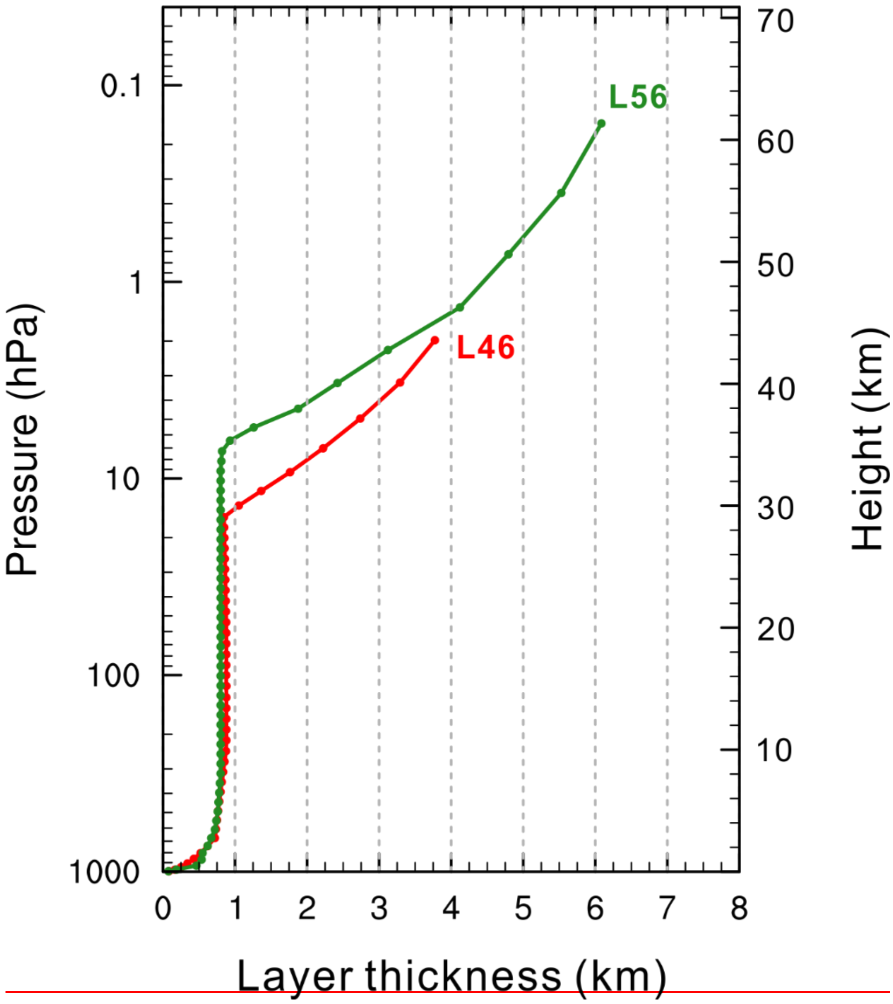

L56
L46
Pressure (hPa)
0.1
1
10
100
1000
Height (km)
70
60
50
40
30
20
10
0
1
2
3
4
5
6
7
8
Layer thickness (km)

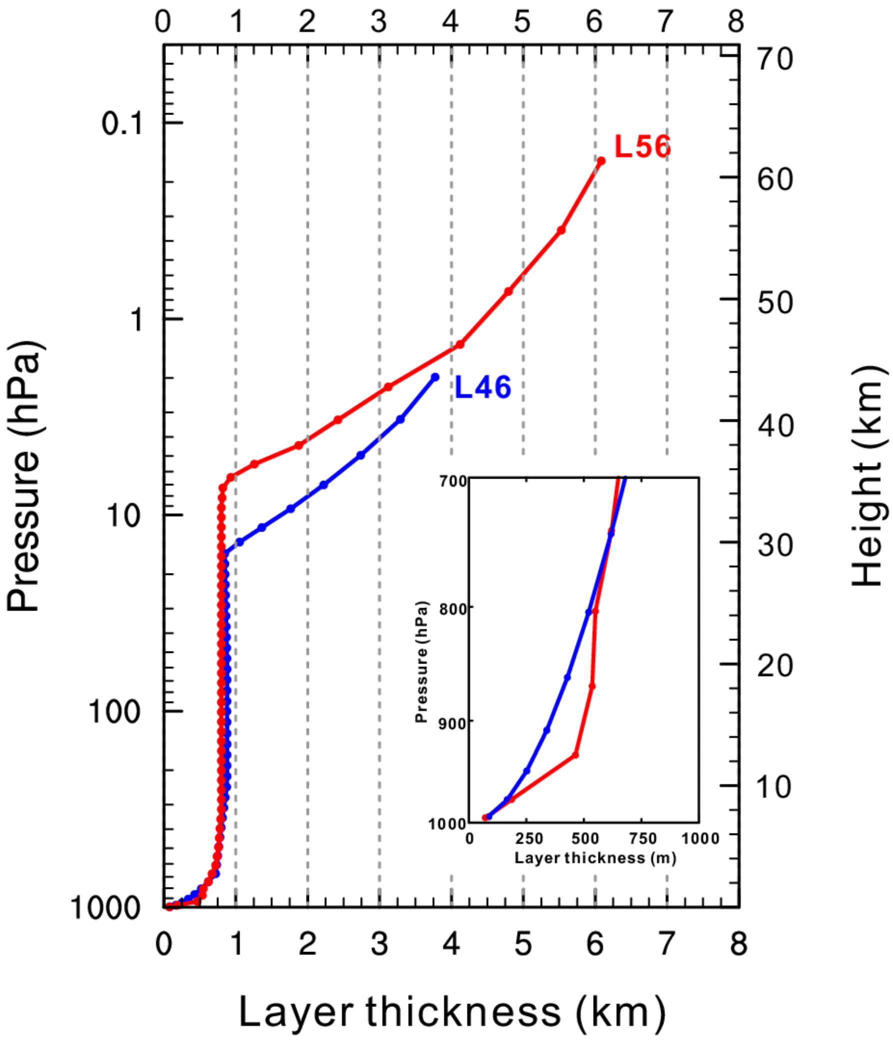

Figure 1. The profiles of layer thickness against height for 46 vertical layers in BCC-CSM2-MR (blue~~red~~) and 56 vertical layers in BCC-CSM2-HR (red~~green~~).

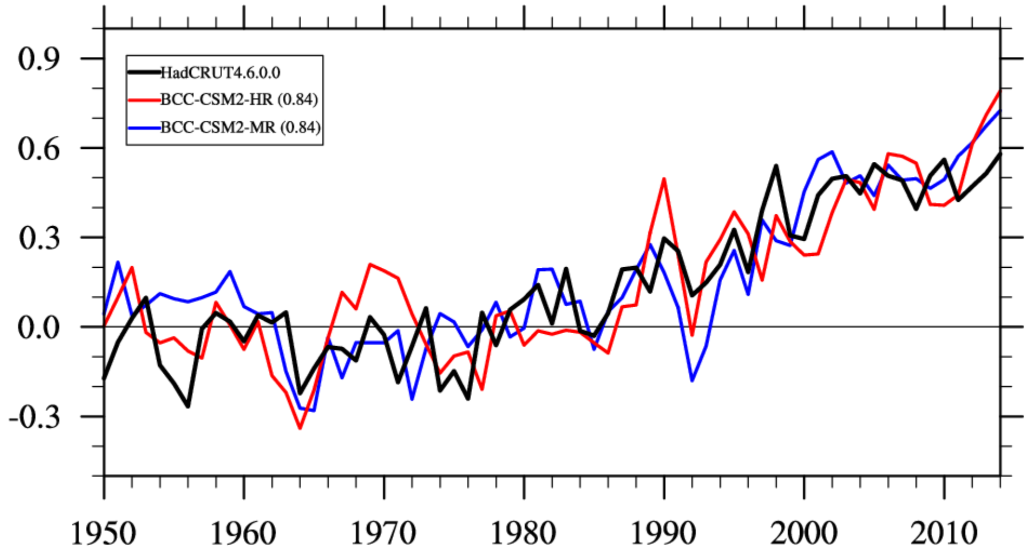

Figure 2. Time series of anomalies in the global mean surface air temperature from 1950 to 2014. The reference climate to deduce anomalies is for each individual curve from 1961 to 1990. The numbers in the parentheses denote the correlation coefficient of 11-year smoothed simulations with HadCRUT4.6.0.0 (Morice et al., 2012) observation.

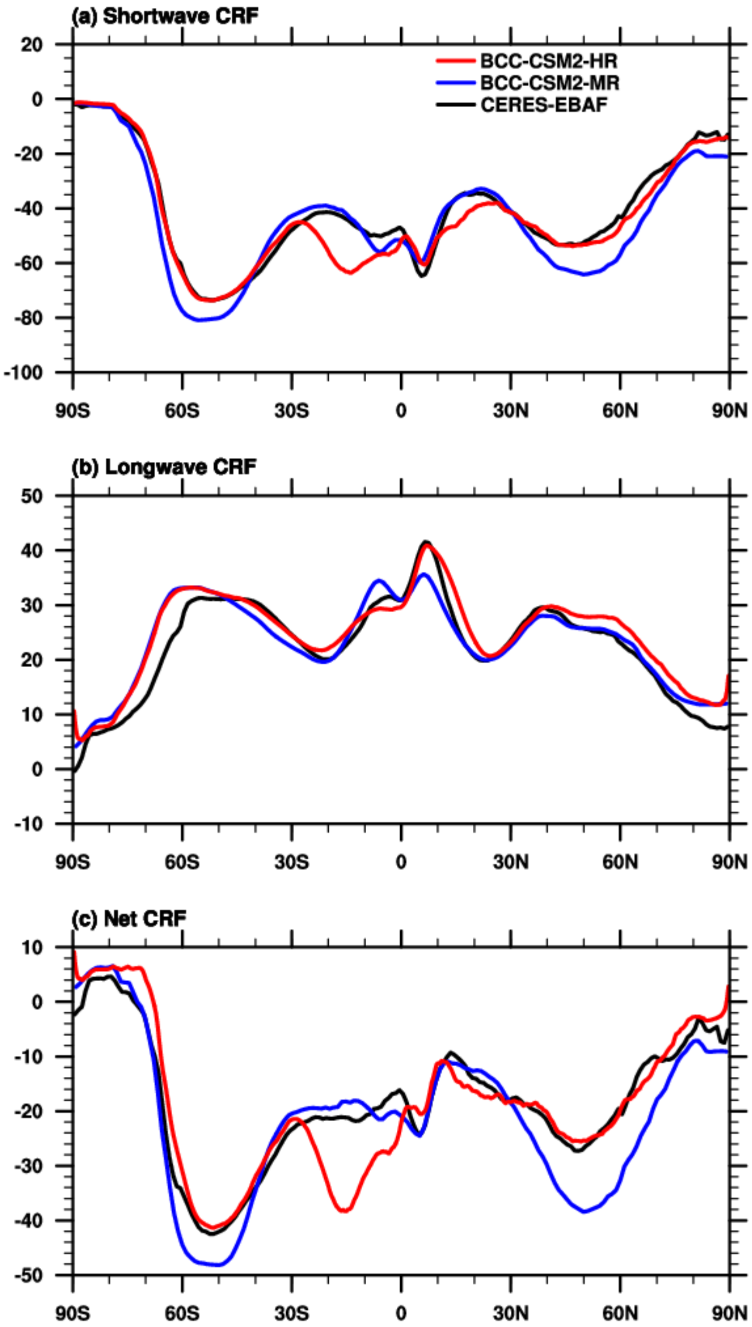

(a) Shortwave CRF
BCC-CSM2-HR
BCC-CSM2-MR
CERES-EBAF
20
0
-20
-40
-60
-80
-100
90S
60S
30S
0
30N
60N
90N
(b) Longwave CRF
50
40
30
20
10
0
-10
90S
60S
30S
0
30N
60N
90N
(c) Net CRF
10
0
-10
-20
-30
-40
-50
90S
60S
30S
0
30N
60N
90N

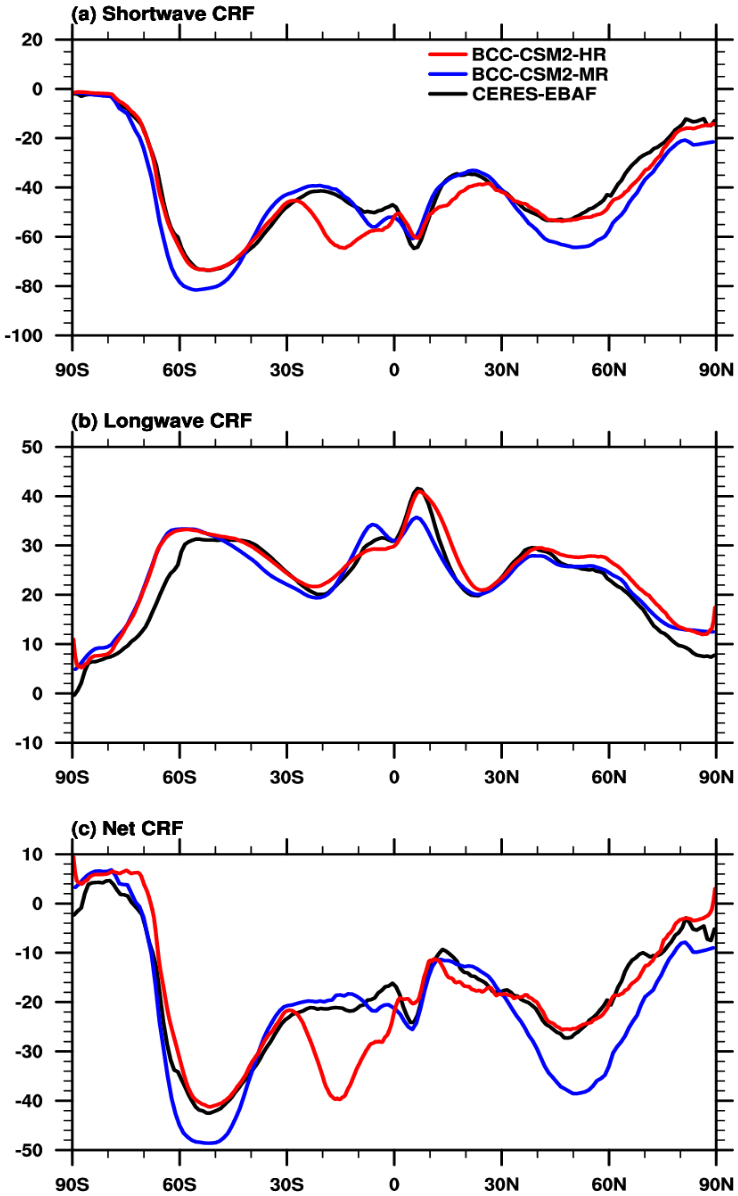

Figure 3~~2~~. Zonal averages of (a) ~~the~~shortwave, (b) longwave, and (c) net cloud radiative forcing (CRF, in W m^{-2}) for the historical simulations (2001~~1971~~-2014~~00~~) of BCC-CSM2-MR (blue lines) and BCC-CSM2-HR (red lines), compared to the 2001-2014 CERES-EBAF observations (black lines).~~2001-2014, a: shortwave effect; b: longwave effect; c: net effect).~~

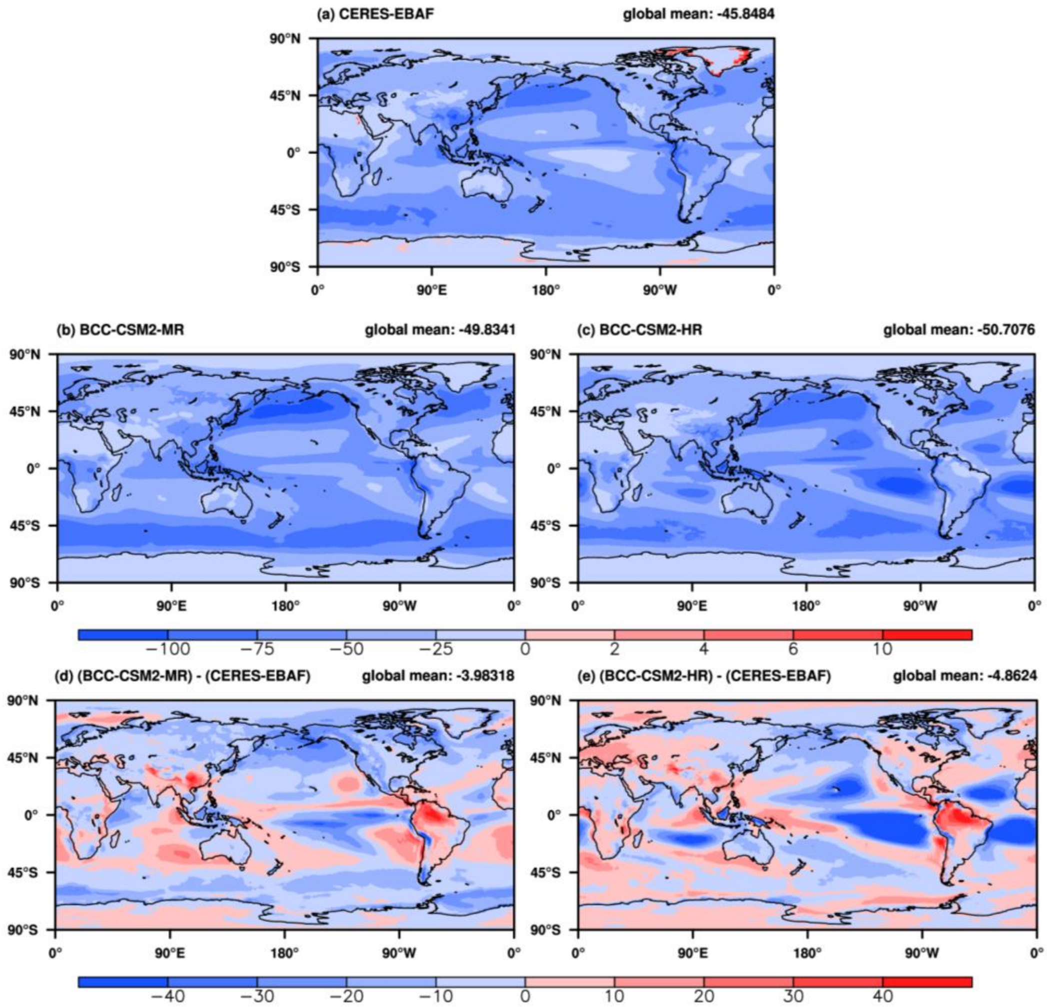
(a) CERES-EBAF
global mean: -45.8484
(b) BCC-CSM2-MR
global mean: -49.8341
(c) BCC-CSM2-HR
global mean: -50.7076
(d) (BCC-CSM2-MR) - (CERES-EBAF)
global mean: -3.98318
(e) (BCC-CSM2-HR) - (CERES-EBAF)
global mean: -4.8624
90°N
45°N
0°
45°S
90°S
0°
90°E
180°
90°W
−100 −75 −50 −25 0 2 4 6 10
−40 −30 −20 −10 0 10 20 30 40

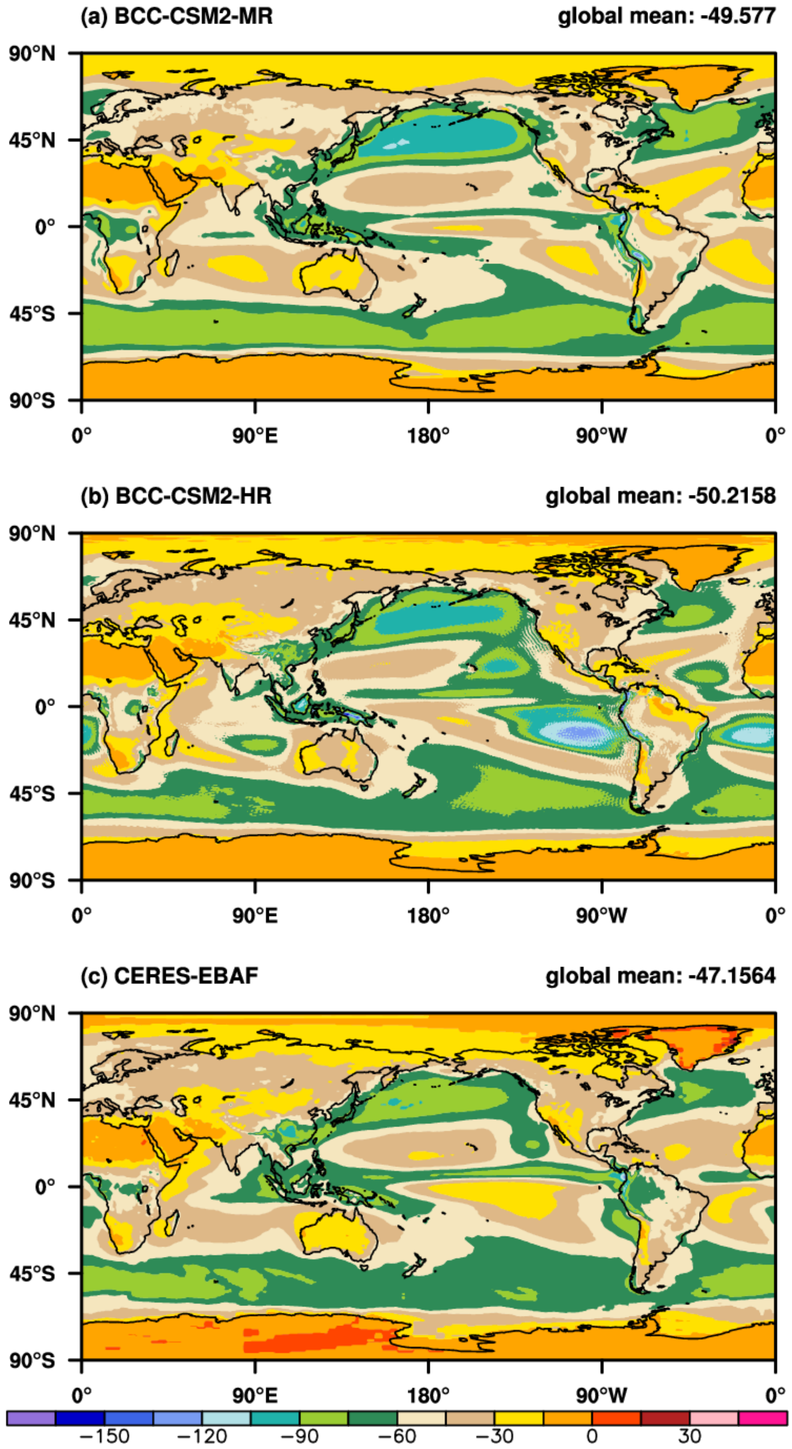

Figure ~~3~~4. The 2001-2014 averaged ~~A~~annual-mean shortwave cloud radiative forcing for (a) the CERES-EBAF observations, the historical simulations ~~, (1971 to 2000) o~~from (b~~a~~) BCC-CSM2-MR and (c~~b~~) BCC-CSM2-HR ~~,~~ and their biases (d and e)~~with comparison~~ against CERES-EBAF data~~(c) the CERES-EBAF observations (2001-2014)~~. Units: W m^{-2}.

1686

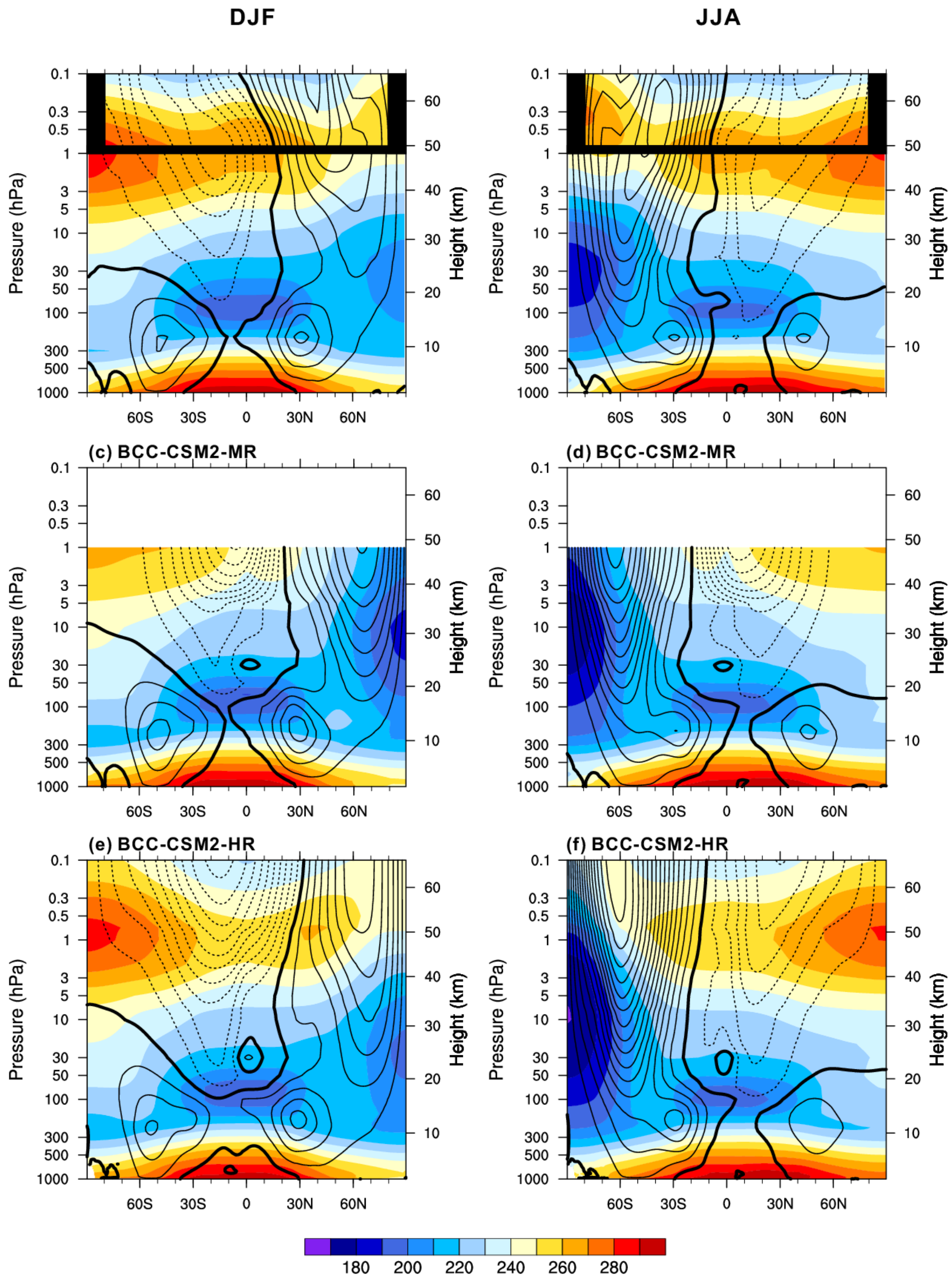
DJF
JJA
(c) BCC-CSM2-MR
(d) BCC-CSM2-MR
(e) BCC-CSM2-HR
(f) BCC-CSM2-HR
Pressure (hPa)
Height (km)
0.1
0.3
0.5
1
3
5
10
30
50
100
300
500
1000
60
50
40
30
20
10
60S
30S
0
30N
60N
180
200
220
240
260
280

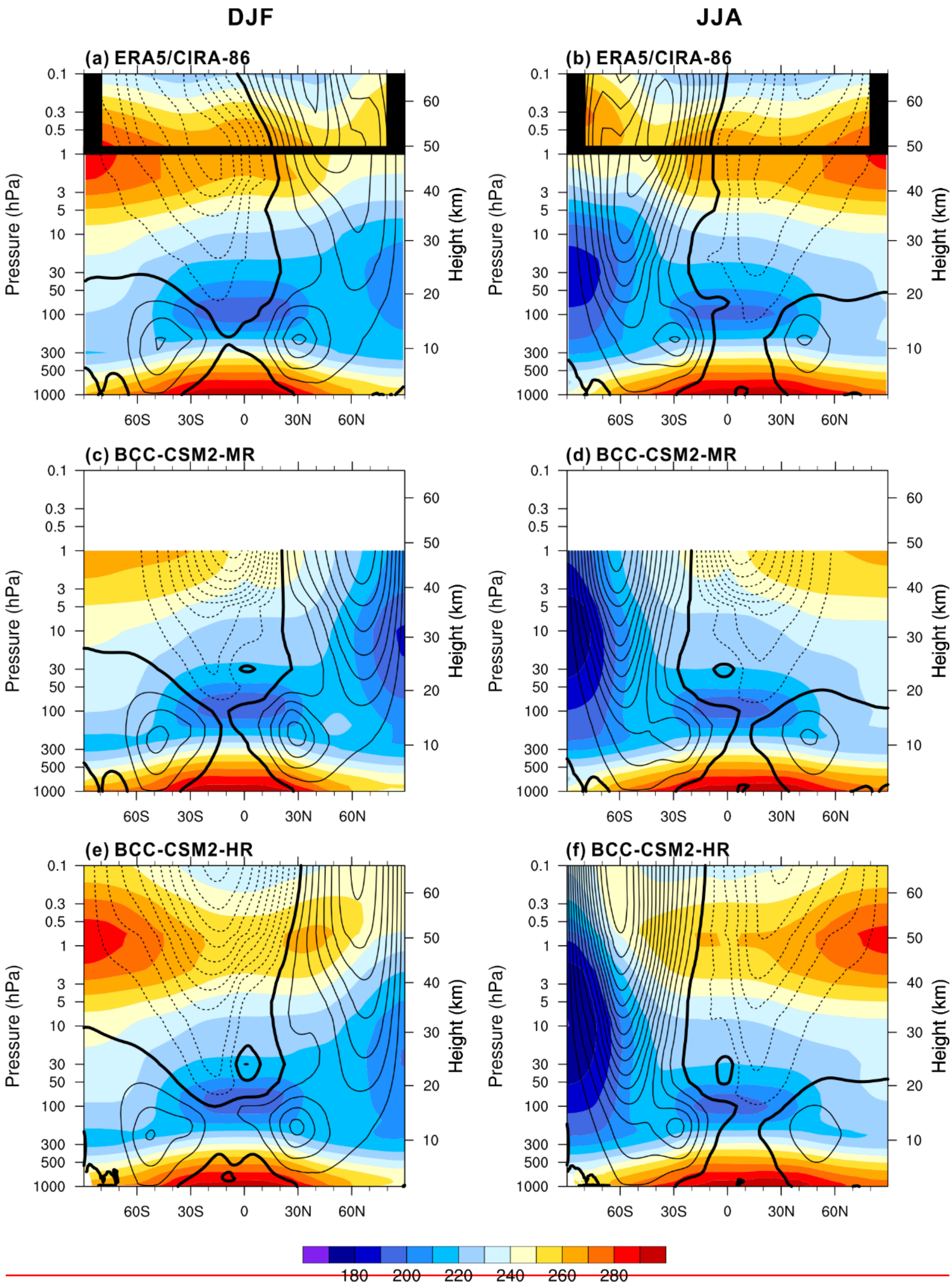

Figure 5~~4~~. The zonal means of temperature (colors; K) and zonal wind (contours; m s^{-1}) averaged for December-January-February (left panel) and Jun-July-August (right panel) from 1995~~71~~ to 2014~~00~~ for (a,b) ERA5/CIRA86, (c,d) BCC-CSM2-MR, (e,f) BCC-CSM2-HR. Positive (negative) zonal winds are plotted with solid (dashed) lines with a contour interval of 10 m s^{-1}. Thick contour line denotes zero zonal wind speed. In (a) and (b), the values above 1 hPa from the COSPAR International Reference Atmosphere (CIRA86, Fleming et al., 1990) and below 1 hPa from the ERA5 reanalysis.

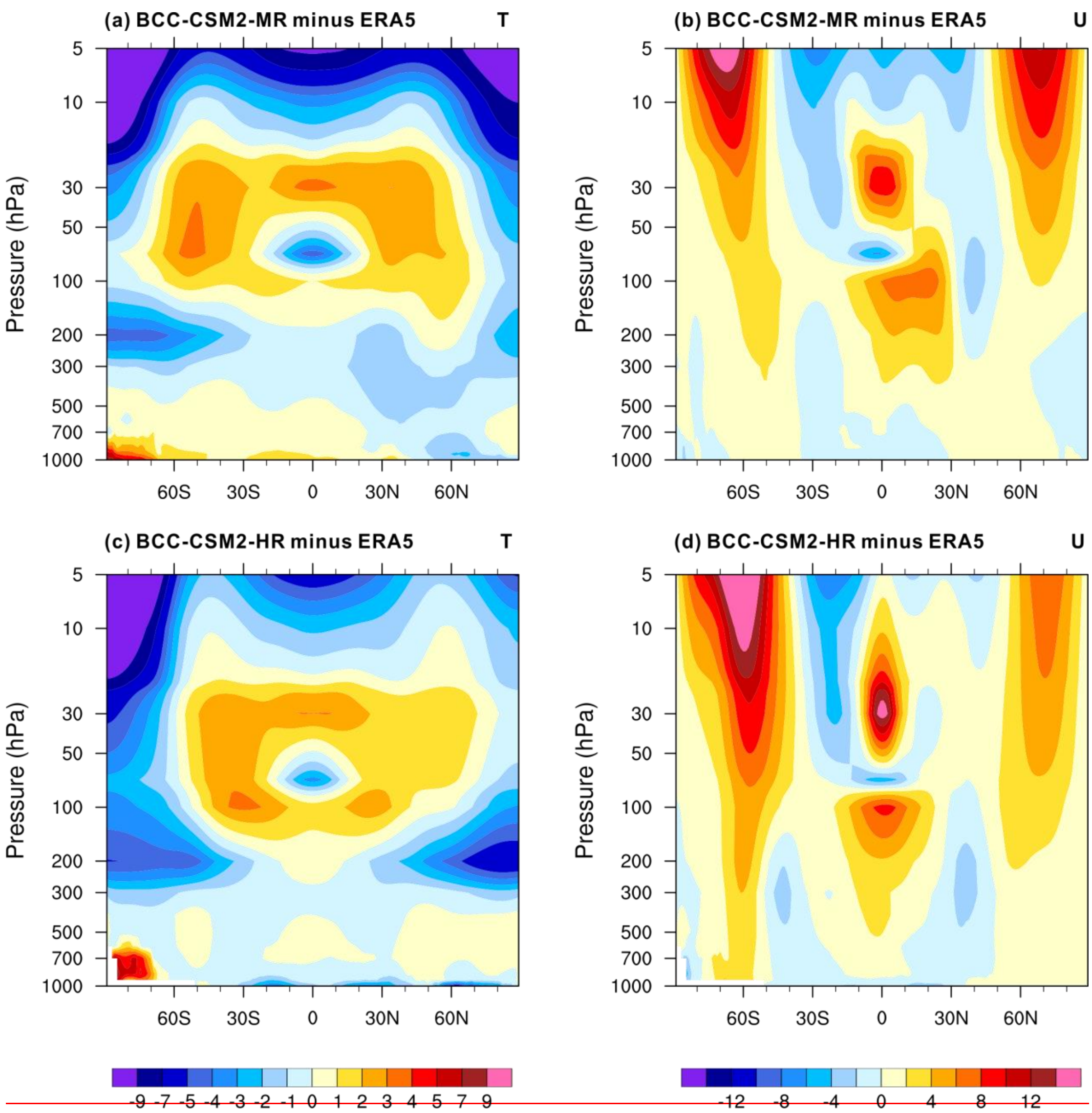
(a) BCC-CSM2-MR minus ERA5
T
(b) BCC-CSM2-MR minus ERA5
U
(c) BCC-CSM2-HR minus ERA5
T
(d) BCC-CSM2-HR minus ERA5
U
Pressure (hPa)
5
10
30
50
100
200
300
500
700
1000
60S
30S
0
30N
60N
-9 -7 -5 -4 -3 -2 -1 0 1 2 3 4 5 7 9
-12 -8 -4 0 4 8 12

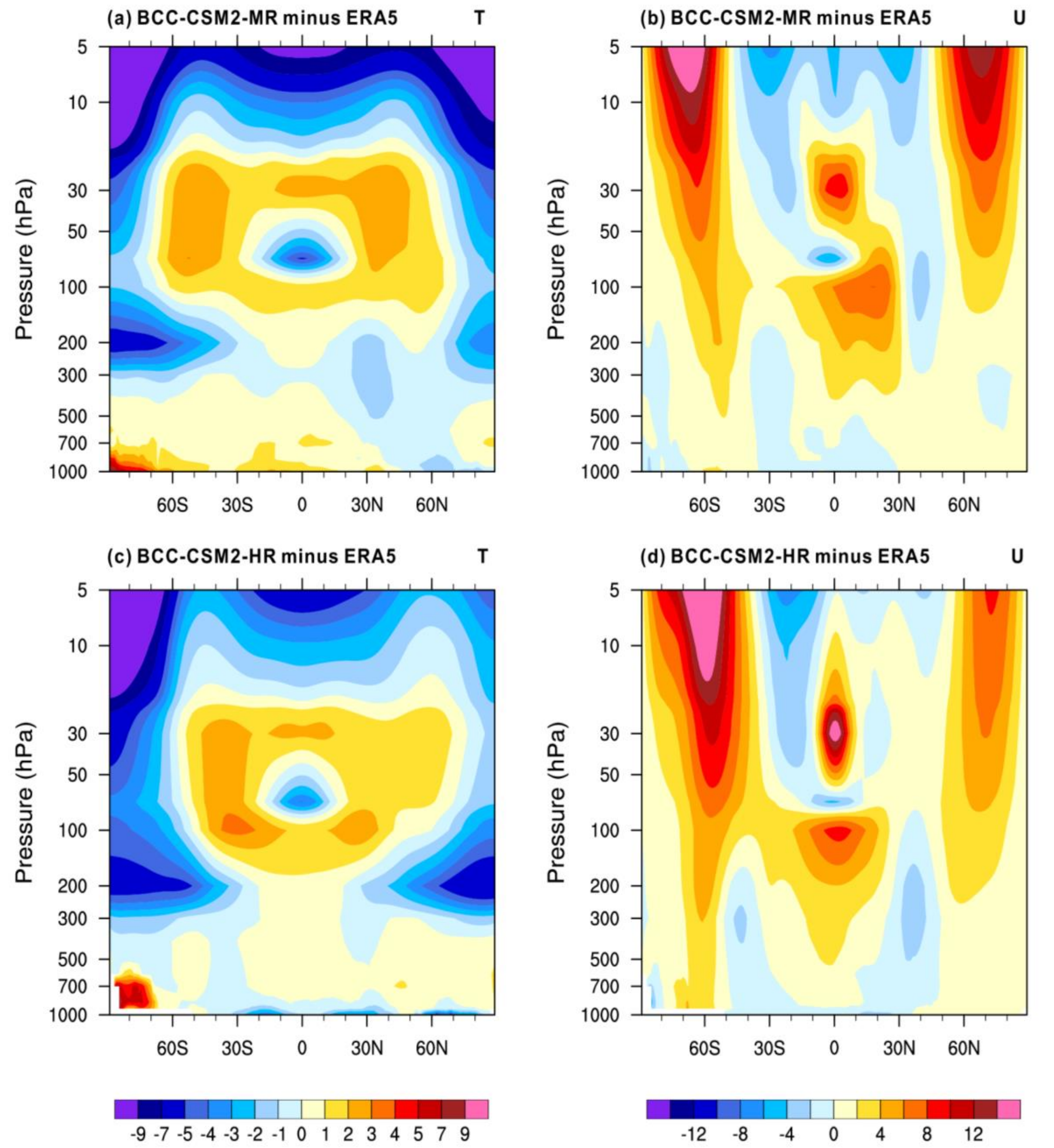

Figure ~~5~~6. Zonally-averaged annual mean temperature biases (left panel, in K) and zonal wind biases (right panel, in m s^{-1}) averaged for the period from 1995~~71~~ to 2014~~00~~ for (a,b) BCC-CSM2-MR, and (c,d) BCC-CSM2-HR, with respect to the ERA5 reanalysis data.

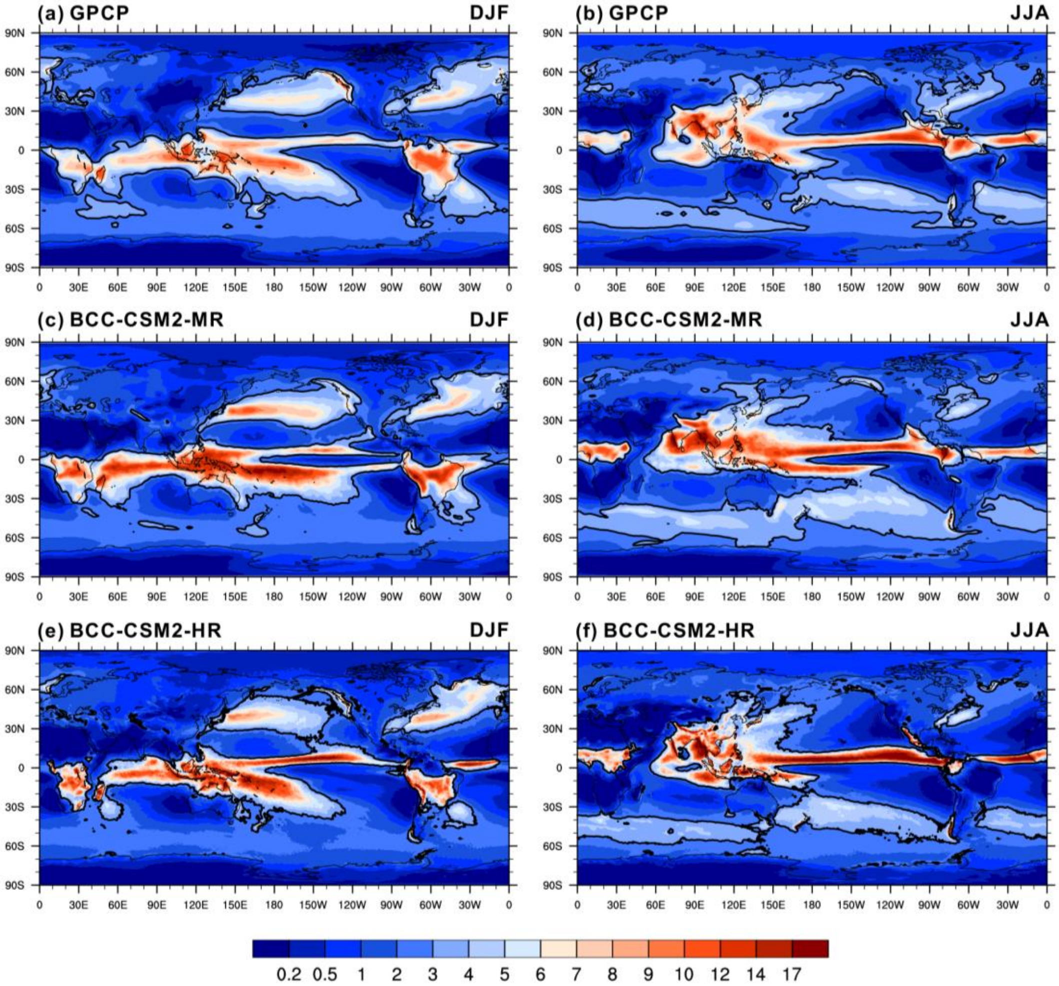
(a) GPCP
DJF
(b) GPCP
JJA
(c) BCC-CSM2-MR
DJF
(d) BCC-CSM2-MR
JJA
(e) BCC-CSM2-HR
DJF
(f) BCC-CSM2-HR
JJA
90N 60N 30N 0 30S 60S 90S
0 30E 60E 90E 120E 150E 180 150W 120W 90W 60W 30W 0
0.2 0.5 1 2 3 4 5 6 7 8 9 10 12 14 17

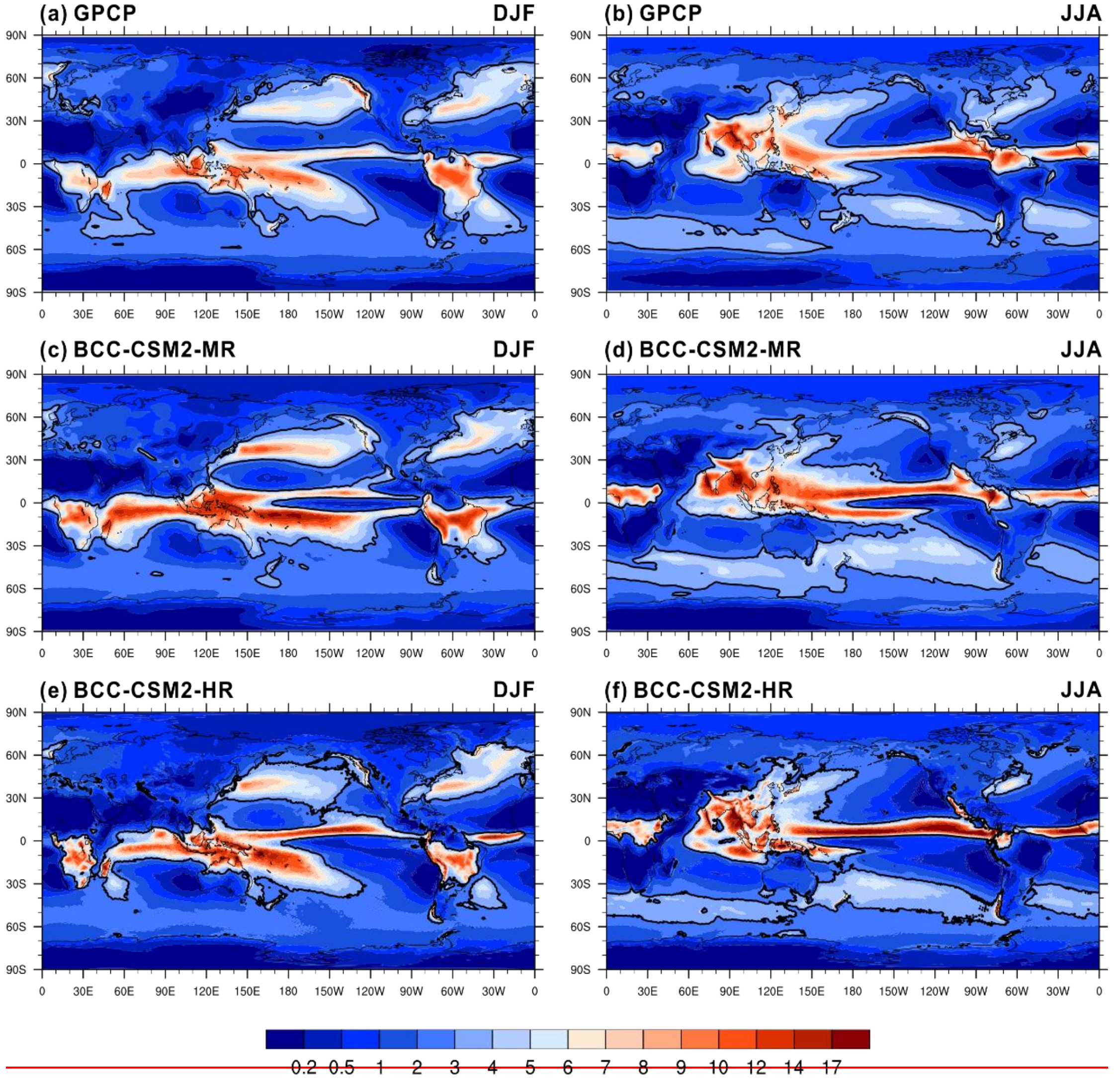

Figure 7~~6~~. The 1995-2014 averaged mean precipitation rate of December-January-February (left panel) and June-July-August (right panel) for (a,b) GPCP observations ~~(1981–2010)~~, (c,d) BCC-CSM2-MR ~~(1971–2000)~~, and (e,f) BCC-CSM2-HR ~~(1971–2000)~~. Units: mm day^{-1}. The 3 mm day^{-1} contour line is in bold as a reference to facilitate the visual inspection.

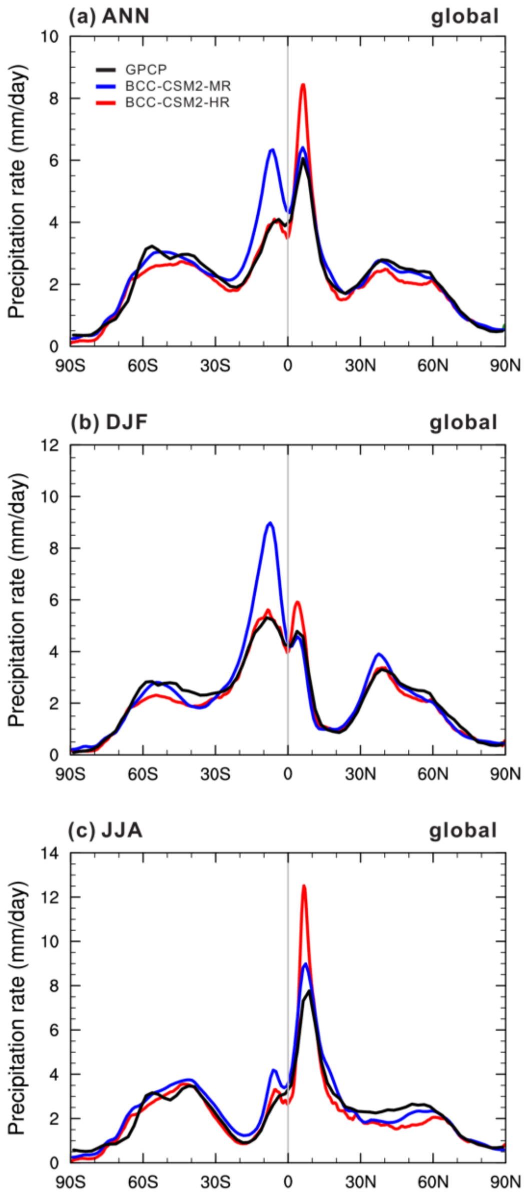
(a) ANN
global
GPCP
BCC-CSM2-MR
BCC-CSM2-HR
Precipitation rate (mm/day)
(b) DJF
global
(c) JJA
global
90S
60S
30S
0
30N
60N
90N

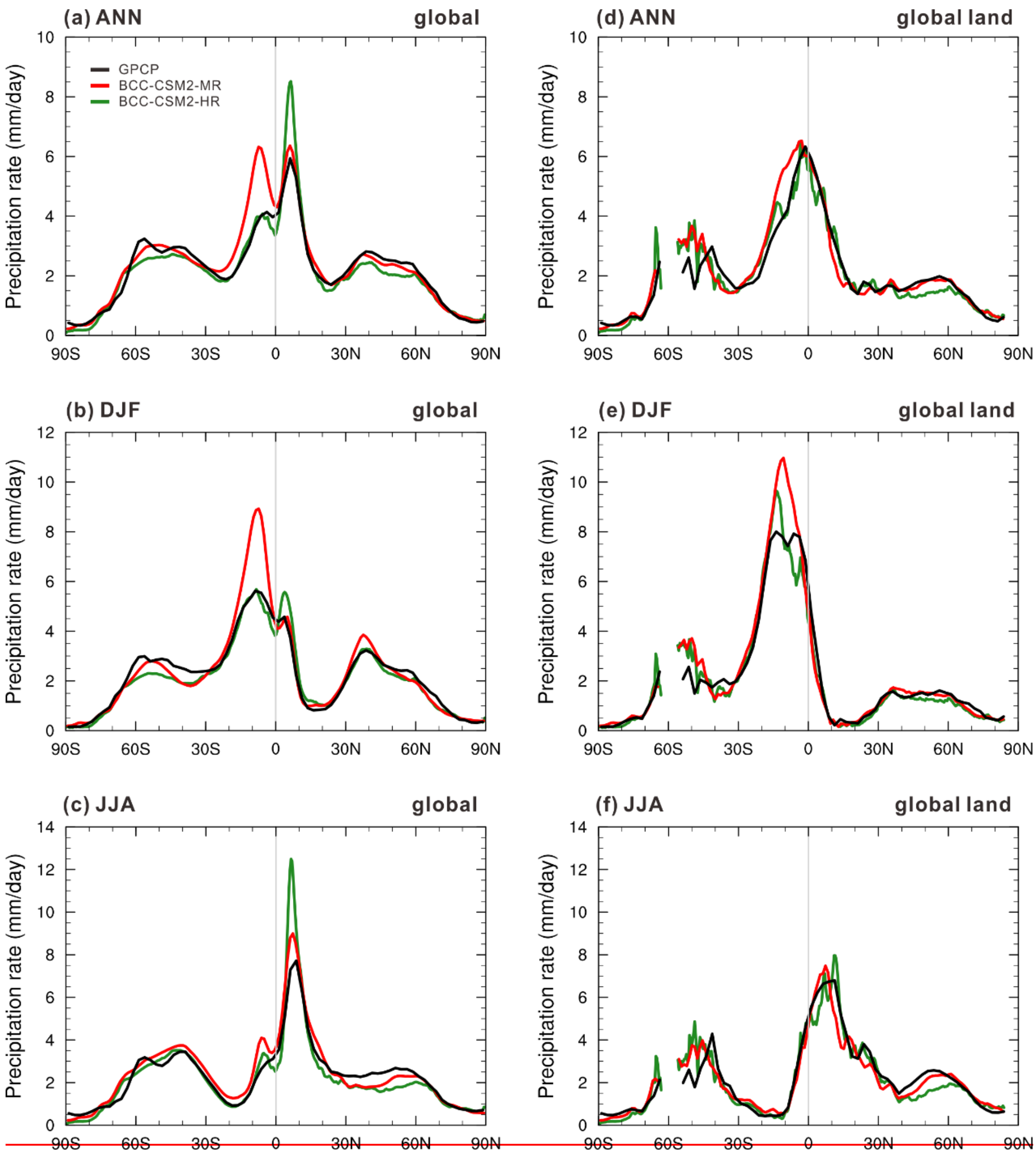

Figure 8~~7~~. The 1995-2014 averaged zonal~~ly averaged~~ mean precipitation rate (mm day^{-1}) ~~averaged~~ for (a~~, d~~) the annual mean, (b~~, e~~) December-February-February, and (c~~, f~~) June-July-August. The solid black lines denote GPCP data~~ (1981–2010)~~, and the color~~color~~ lines show BCC-CSM2-MR (blue) ~~(1971–2000)~~ and BCC-CSM2-HR (red~~1971–2000~~) simulations. Units: mm day^{-1}.

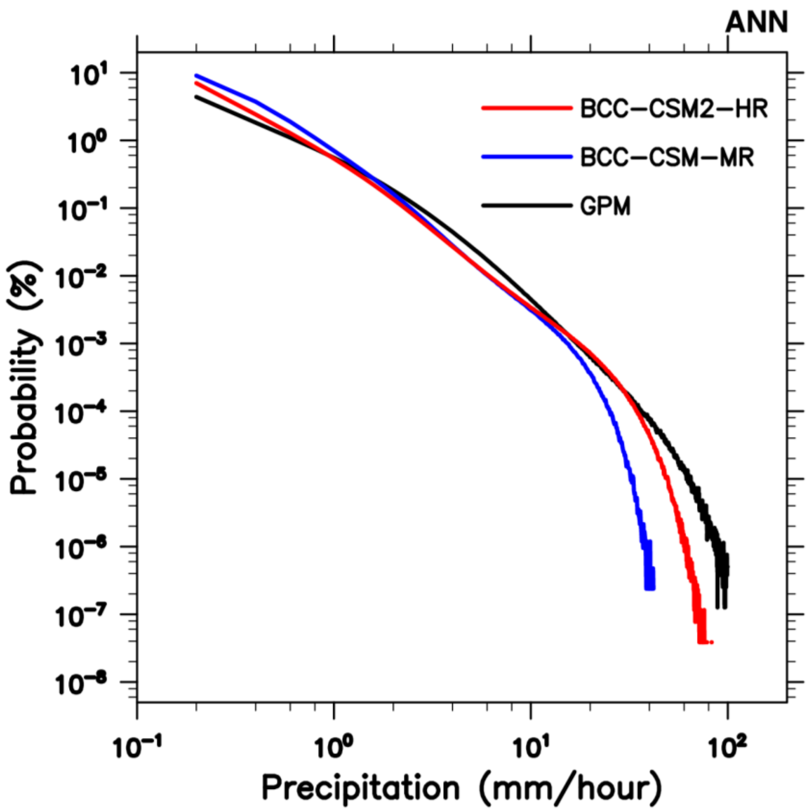

Figure 9~~8~~. The probability density of 3-hourly~~ly~~ precipitation between 40 °S and 40 °N and during the period from 2001 to 2014, in function of precipitation intensity with intervals of 1 mm/hour, for~~ between 40 °S and 40 °N derived from every 3 hours data for the~~ IMERG ~~Global~~ Precipitation~~ Measurement~~ (~~GPM~~black line), ~~from 2001 to 2019, and for~~ BCC-CSM2-MR (blue line) and BCC-CSM2-HR (red line), respectively. ~~simulations from 1971 to 2000.~~Two simulations were re-gridded to the grid of IMERG before processing.

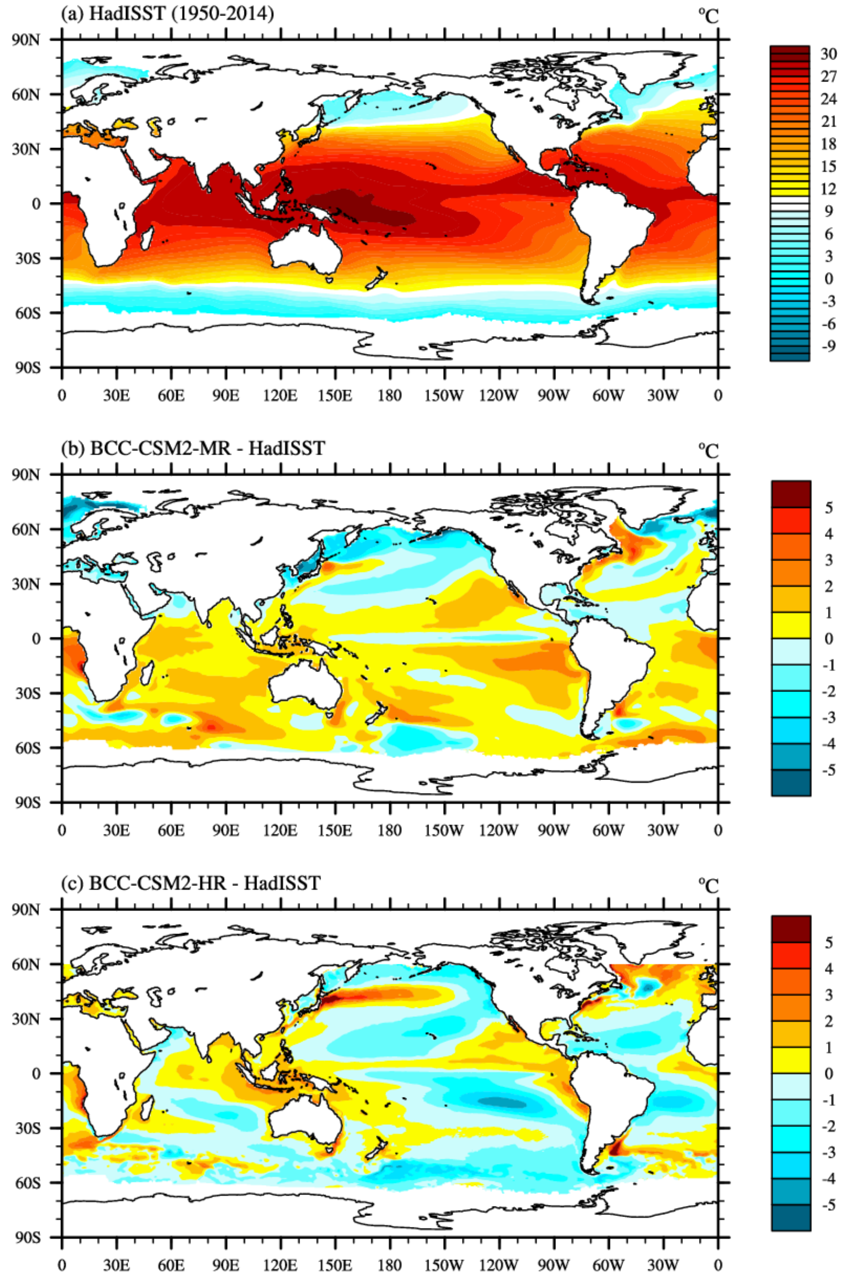
(a) HadISST (1950-2014)
°C
90N
60N
30N
0
30S
60S
90S
0
30E
60E
90E
120E
150E
180
150W
120W
90W
60W
30W
30
27
24
21
18
15
12
9
6
3
0
-3
-6
-9
(b) BCC-CSM2-MR - HadISST
°C
5
4
3
2
1
0
-1
-2
-3
-4
-5
(c) BCC-CSM2-HR - HadISST
°C

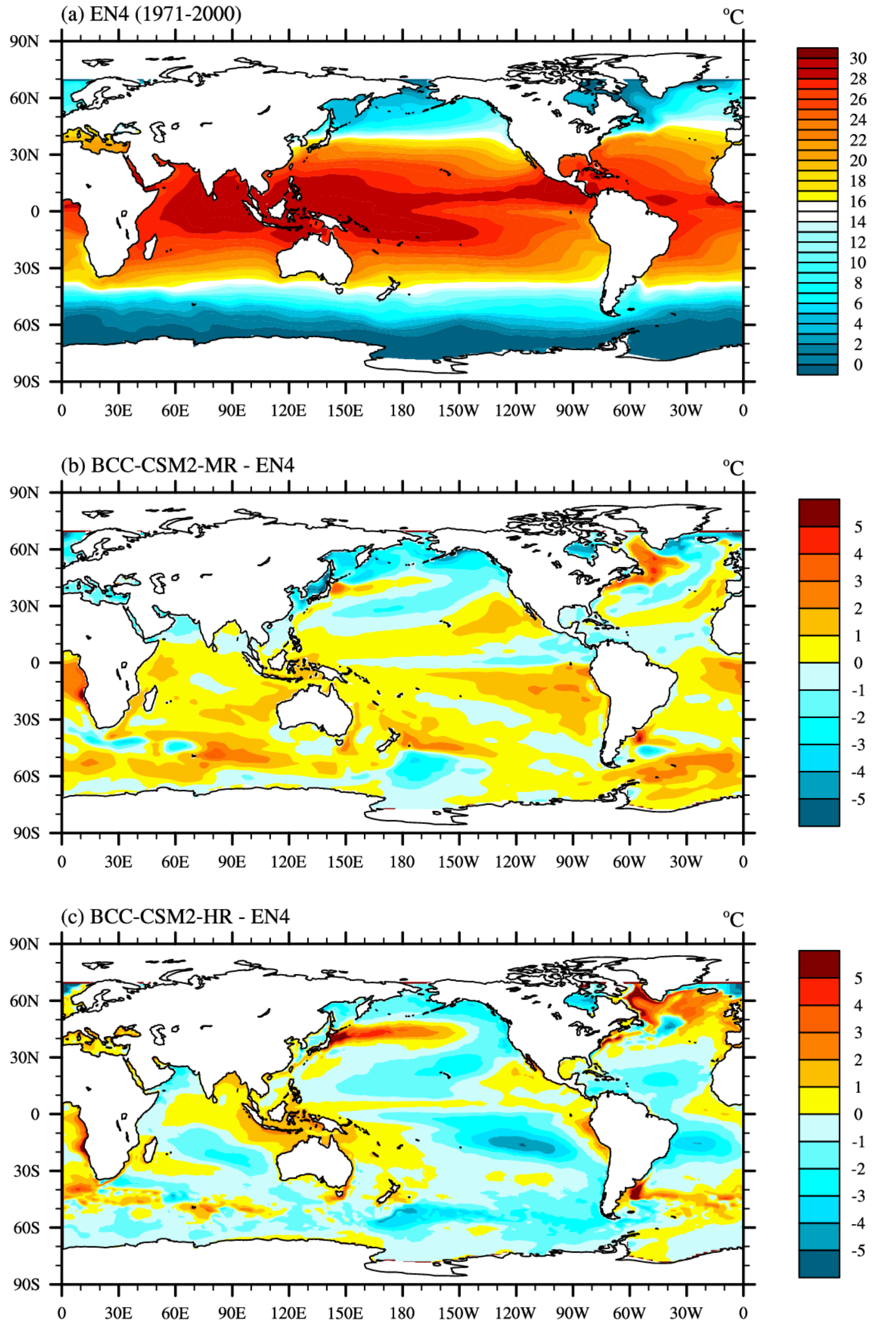

Figure 10~~9~~. The global distributions of the 1995~~71~~-2014~~00~~ annual mean sea surface temperature for (a) the observations from ~~Met Office Hadley Centre~~ HadISST~~EN4 dataset~~, and the simulation biases in (b) BCC-CSM2-MR and (c) BCC-CSM2-HR.

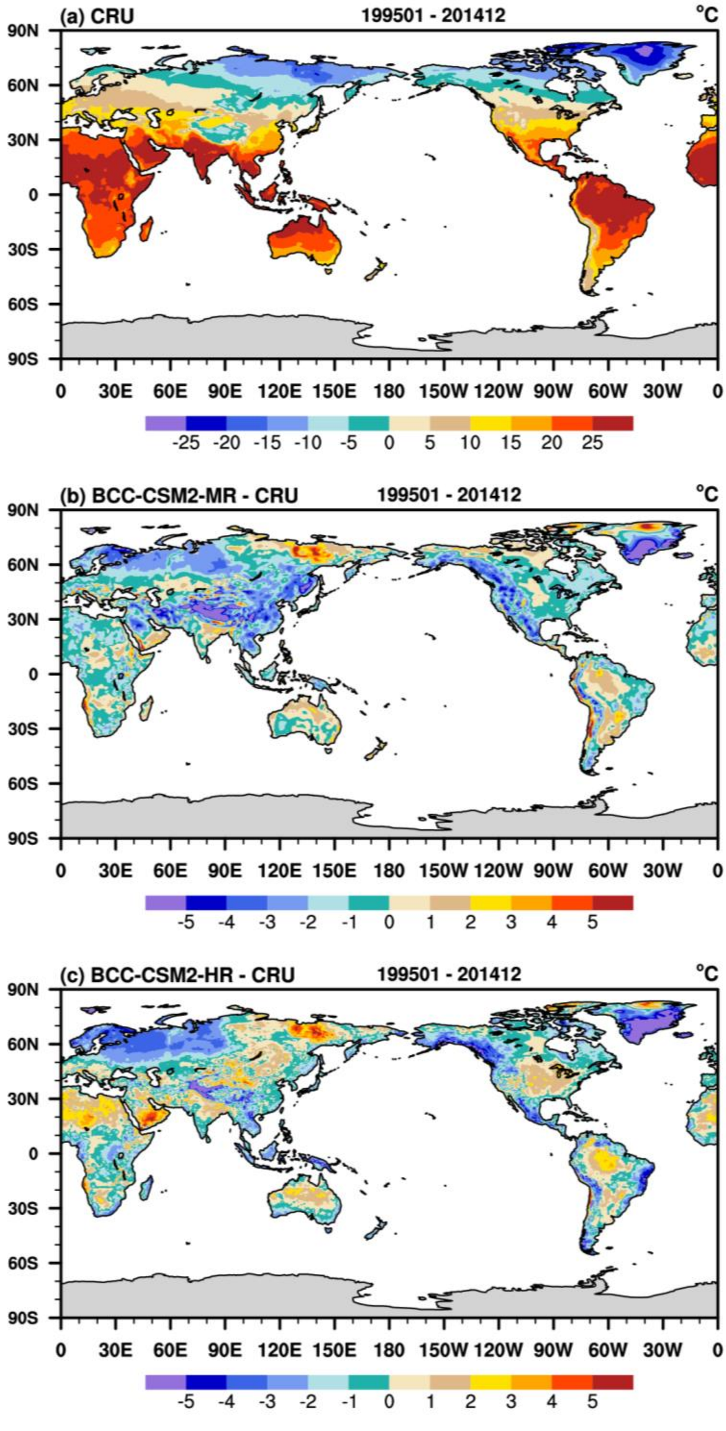
(a) CRU
199501 - 201412
°C
90N
60N
30N
0
30S
60S
90S
0
30E
60E
90E
120E
150E
180
150W
120W
90W
60W
30W
0
-25 -20 -15 -10 -5 0 5 10 15 20 25
(b) BCC-CSM2-MR - CRU
199501 - 201412
°C
-5 -4 -3 -2 -1 0 1 2 3 4 5
(c) BCC-CSM2-HR - CRU
199501 - 201412
°C
-5 -4 -3 -2 -1 0 1 2 3 4 5

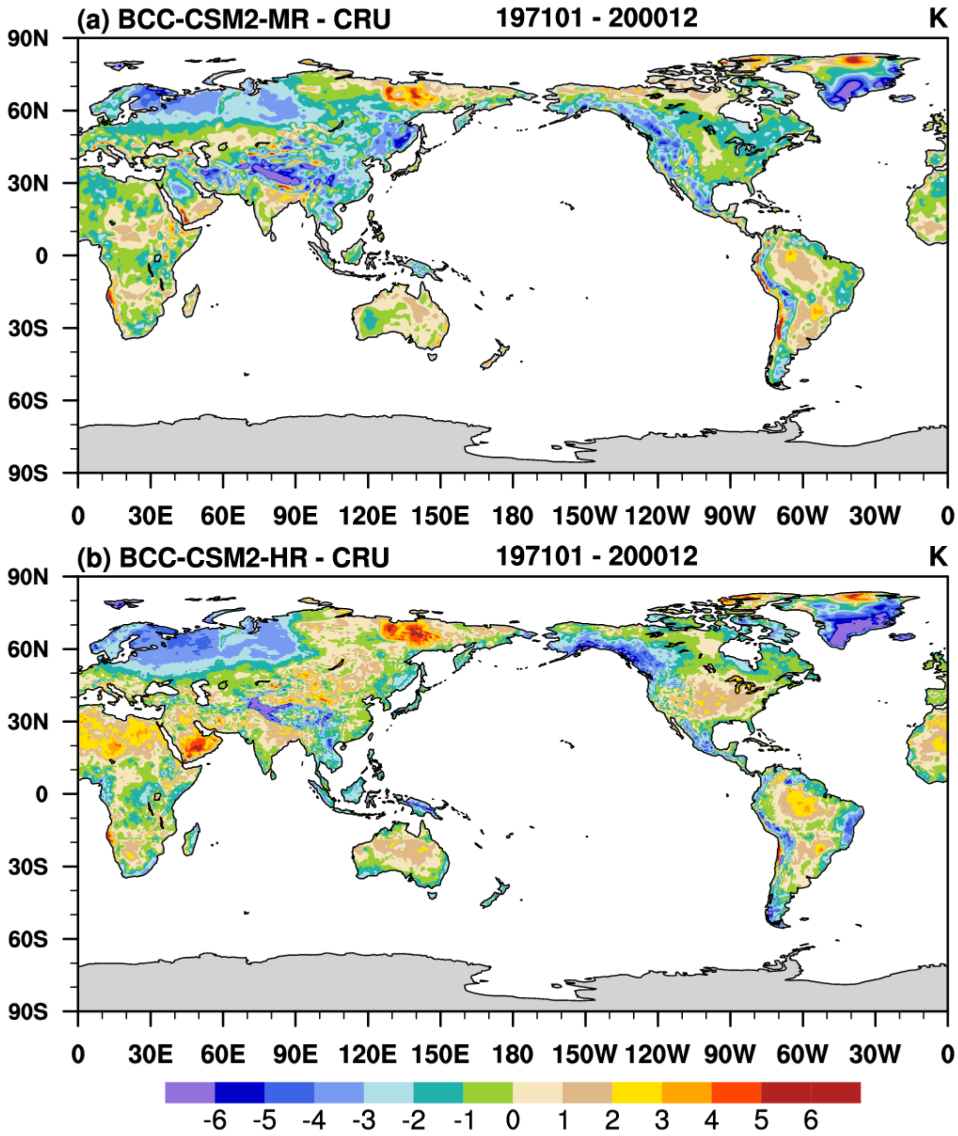

Figure 11~~0~~. The 1995-2014 averaged global land-surface air temperature for (a) CRUTEM observations, and simulation biases ~~of annual mean land-surface air temperature~~ in (b) BCC-CSM2-MR and (c) BCC-CSM2-HR~~, with contrast to HadCRUT~~ .~~global land-surface air temperature observations during the period from 1971 to 2000.~~

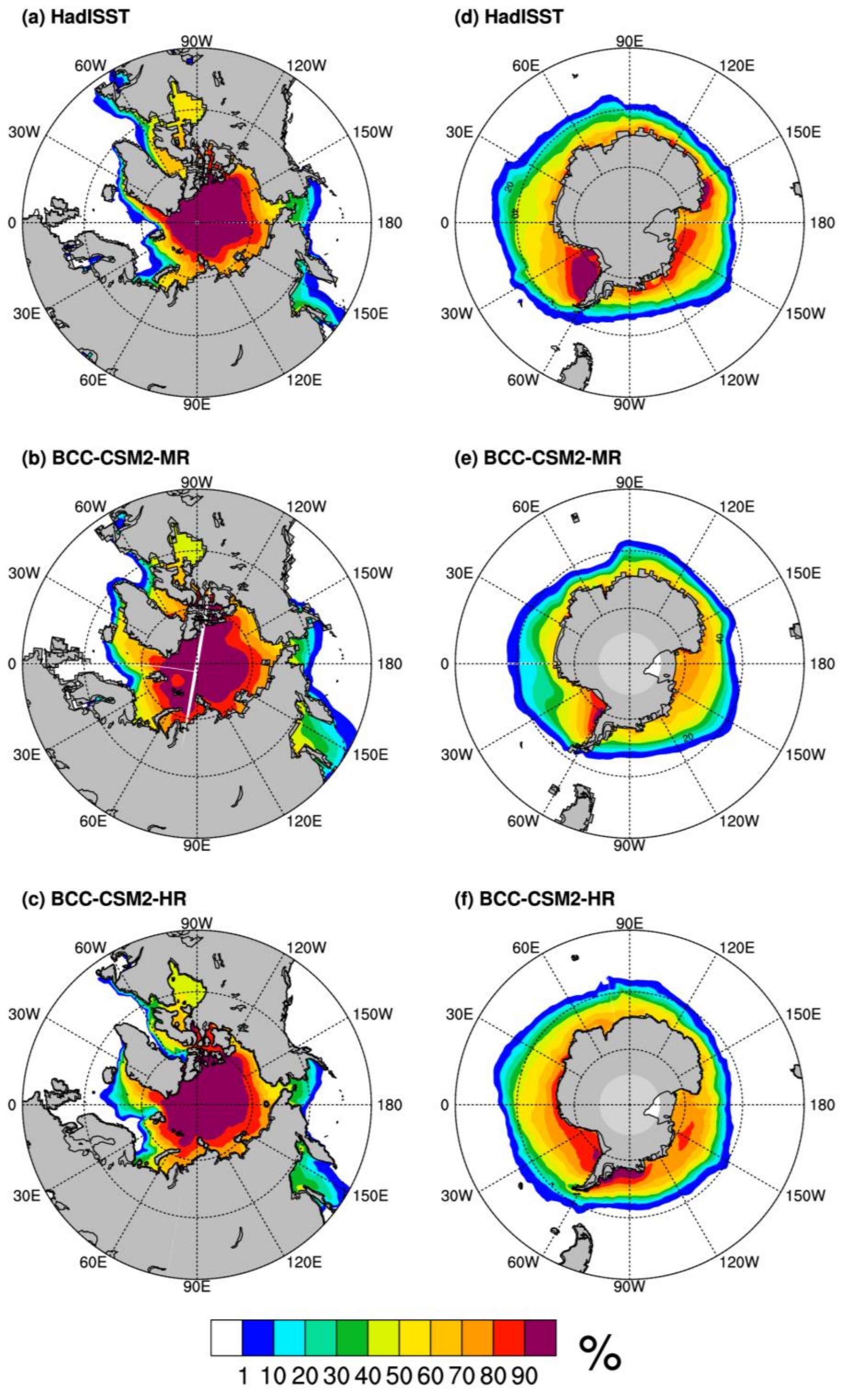
(a) HadISST
(b) BCC-CSM2-MR
(c) BCC-CSM2-HR
(d) HadISST
(e) BCC-CSM2-MR
(f) BCC-CSM2-HR
90W
120W
150W
180
150E
120E
90E
60E
30E
0
30W
60W
90E
120E
150E
180
150W
120W
90W
60W
30W
0
30E
60E
1 10 20 30 40 50 60 70 80 90
%

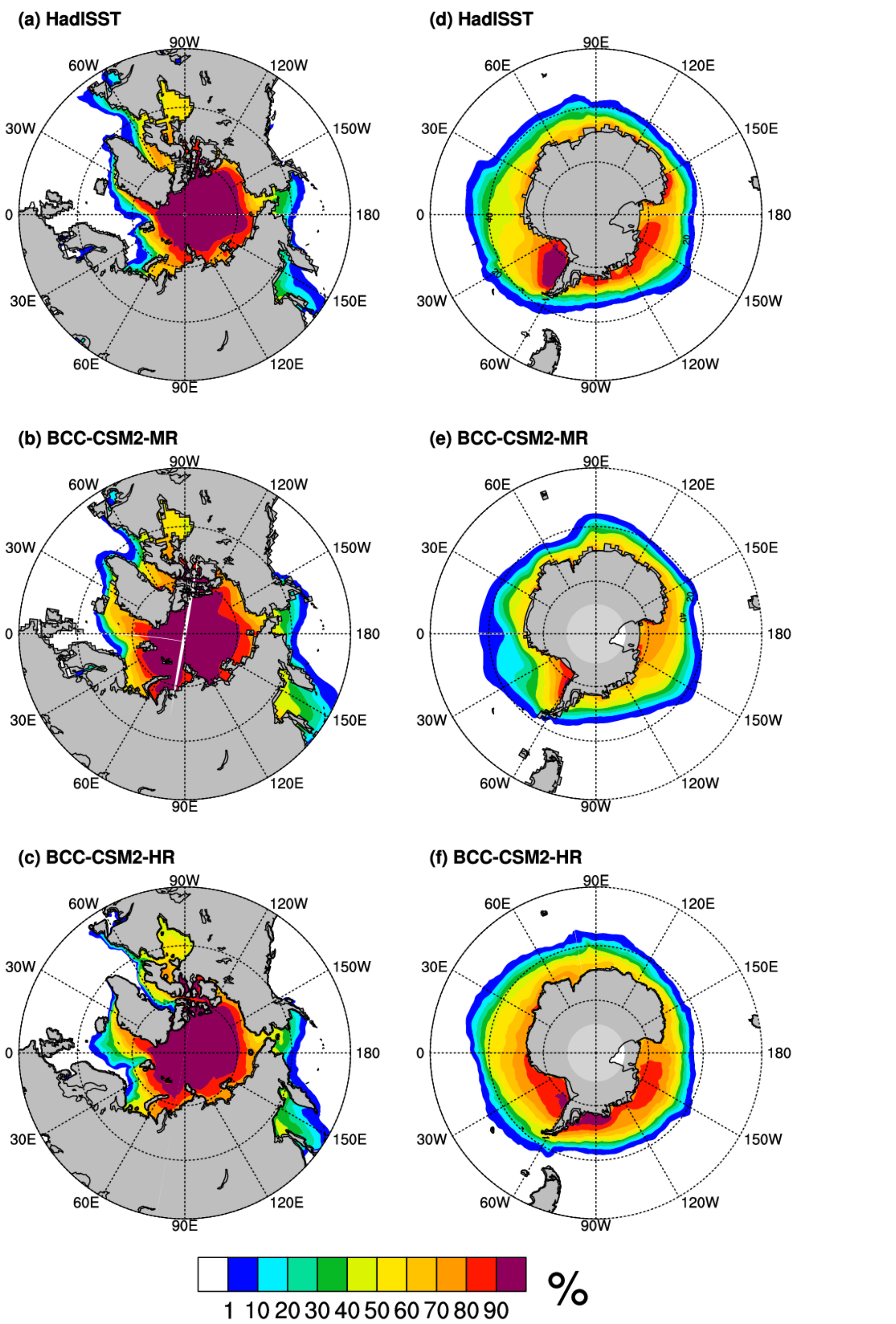

Figure 1~~1~~2. The ~~annual mean~~ spatial distribution of annual mean sea ice concentration ~~sea ice extents~~ from BCC-CSM2-MR and BCC-CSM2-HR with contrast to the observations from the Hadley Centre Sea Ice data set from 1995~~71~~ to 2014~~00~~.

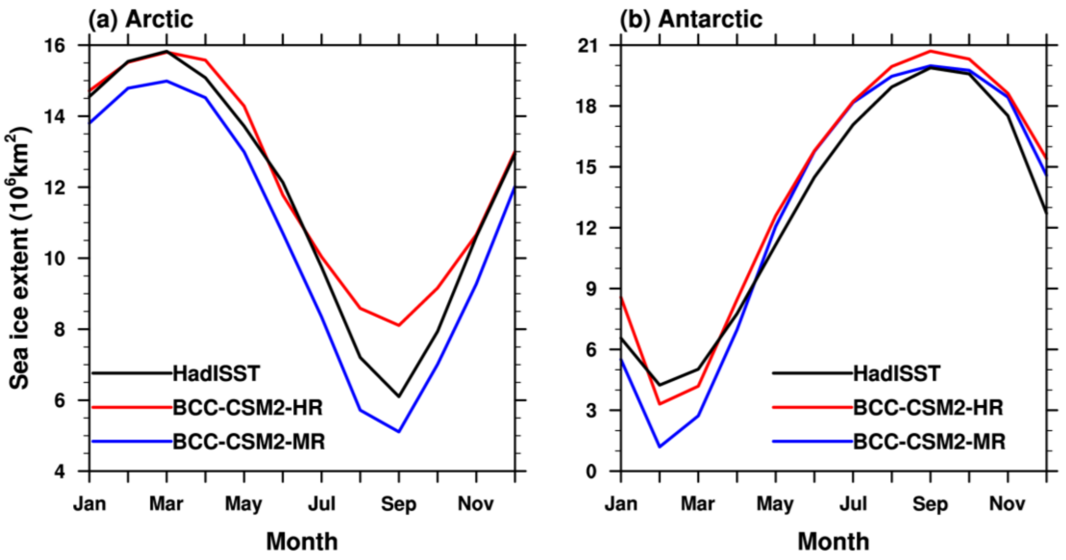

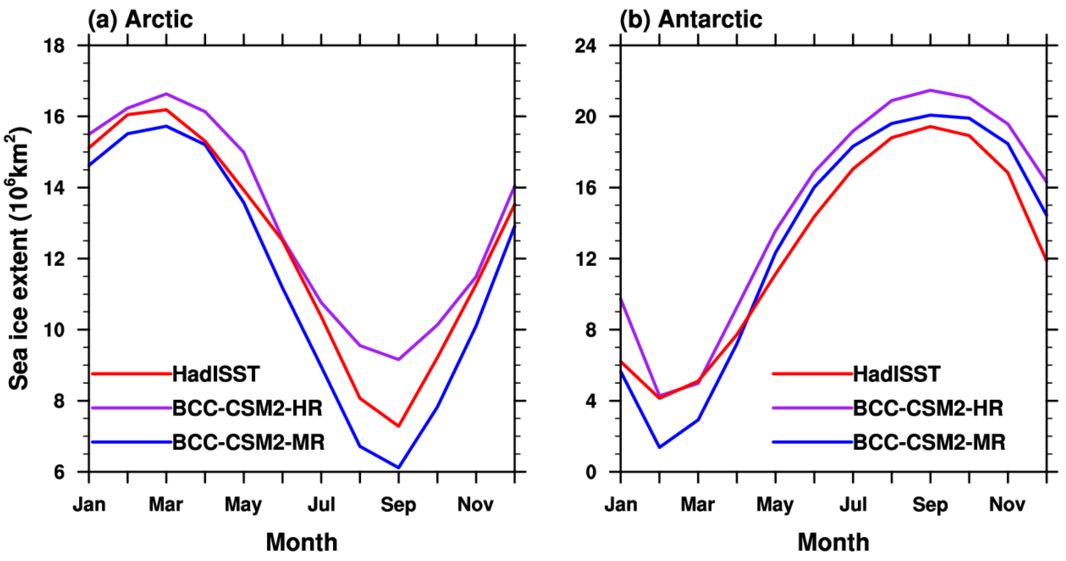

Figure 13~~2~~. The mean (1995~~71~~-2014~~1990~~) seasonal cycle of sea-ice extent (with a sea-ice concentration of at least 15 %) in (a) the Northern Hemisphere and (b) the Southern Hemisphere for the observations from the Hadley Centre Sea Ice and Sea Surface Temperature data~~—~~set (black~~red —~~ lines) and the simulations from BCC-CSM2-MR (blue lines), BCC-CSM2-HR (red~~purple~~ lines).

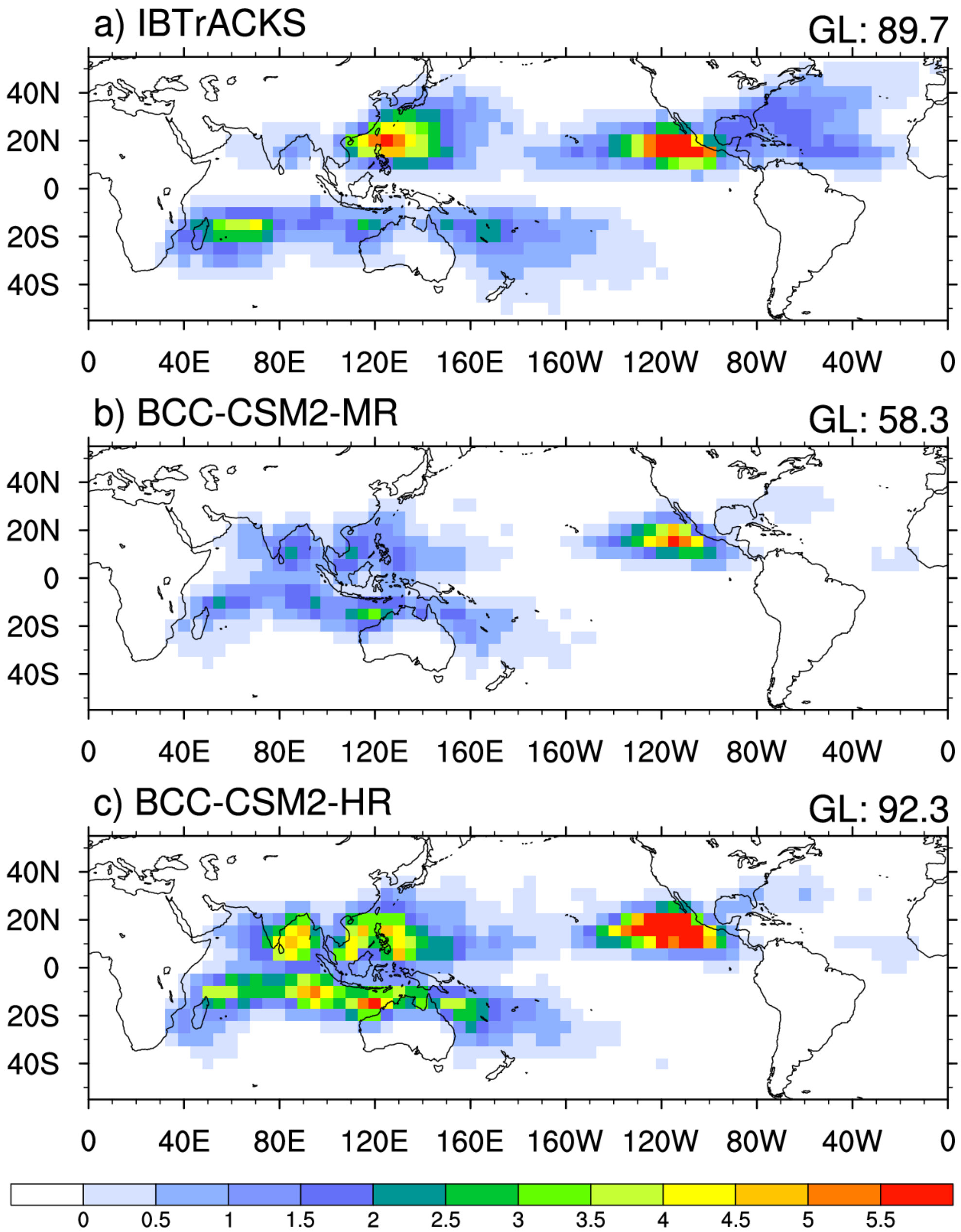
a) IBTrACKS
GL: 89.7
b) BCC-CSM2-MR
GL: 58.3
c) BCC-CSM2-HR
GL: 92.3
40N
20N
0
20S
40S
0 40E 80E 120E 160E 160W 120W 80W 40W 0
0 0.5 1 1.5 2 2.5 3 3.5 4 4.5 5 5.5

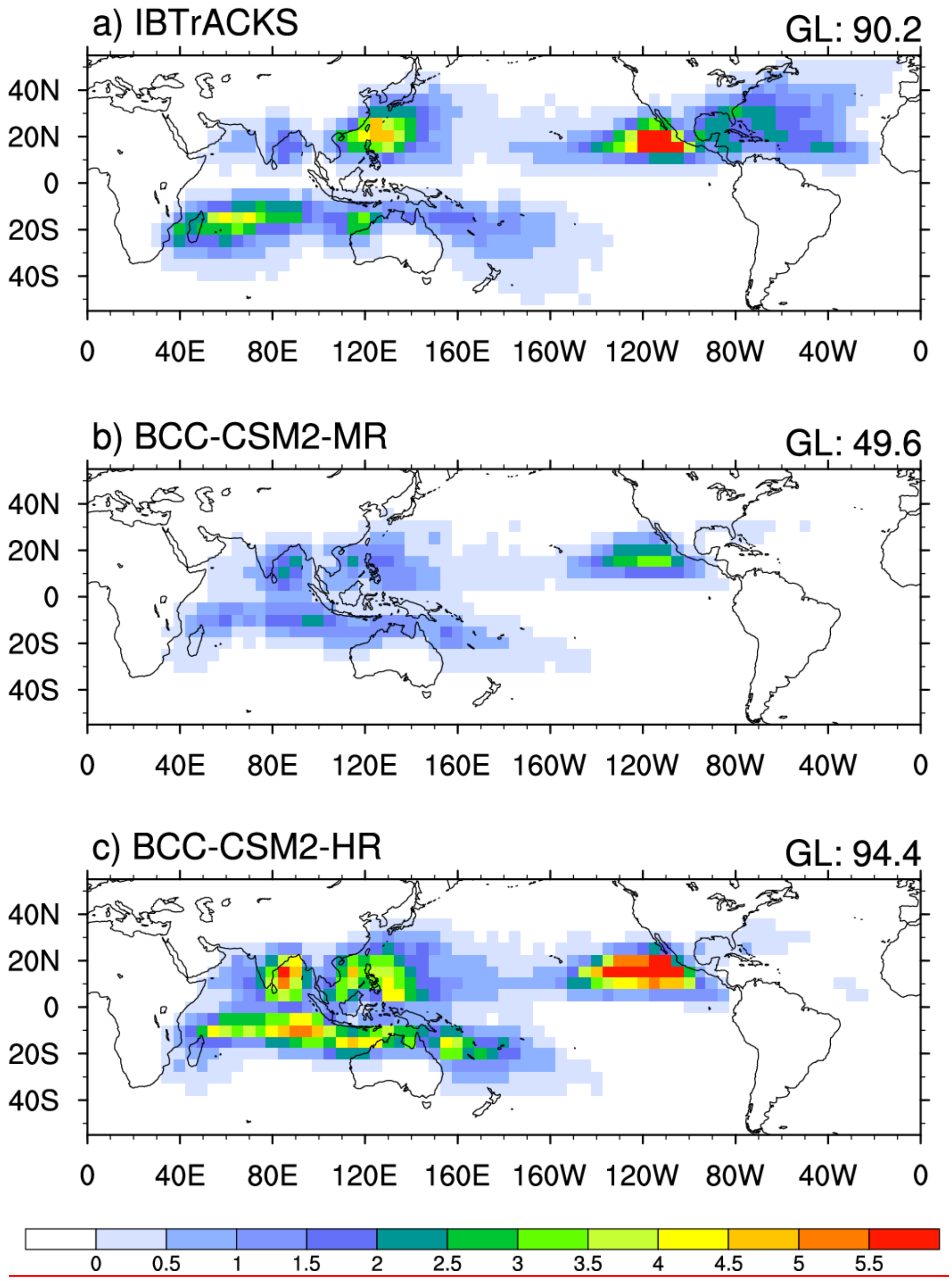

Figure 14~~3~~. The global distribution of tropical cyclone (TC) densities (number per year) averaged for the period of 1995-2014 from (a) the ~~1981-2000~~ IBTrACS_wmo observations, and the simulations of ~~and~~ (b) B~~the~~CC-CSM2-MR ~~1981-2000 simulations~~ and ~~from (b) BCC-CSM2-MR, and~~ (c) BCC-CSM2-HR. The value on the upper-right corner denotes the total number of global TCs on 5°×5° grid box.

1796

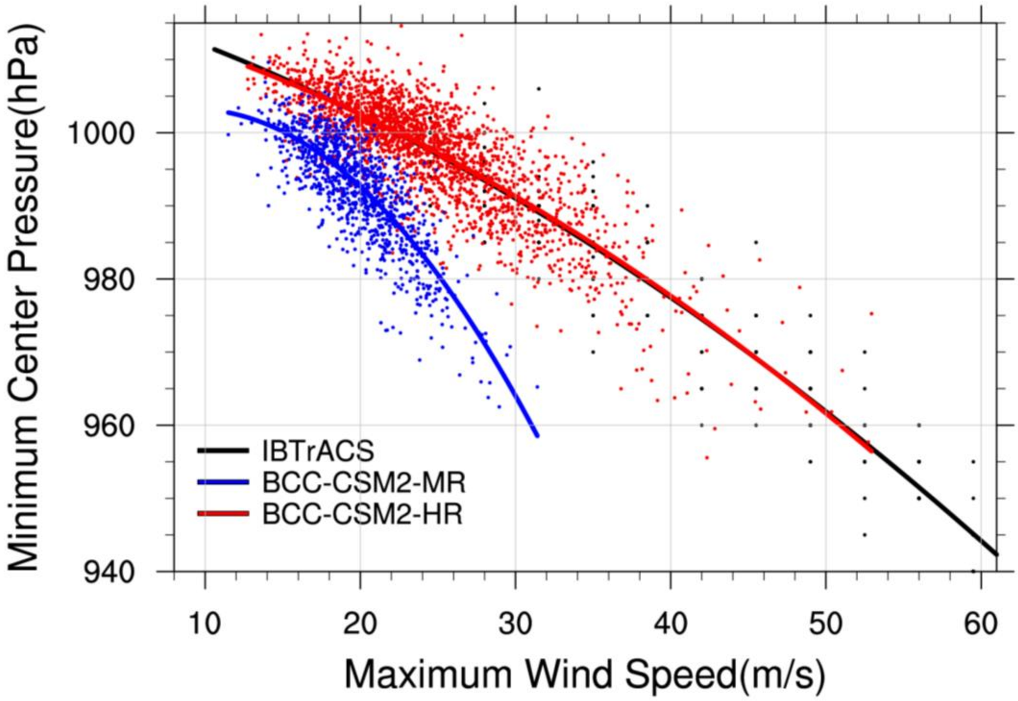

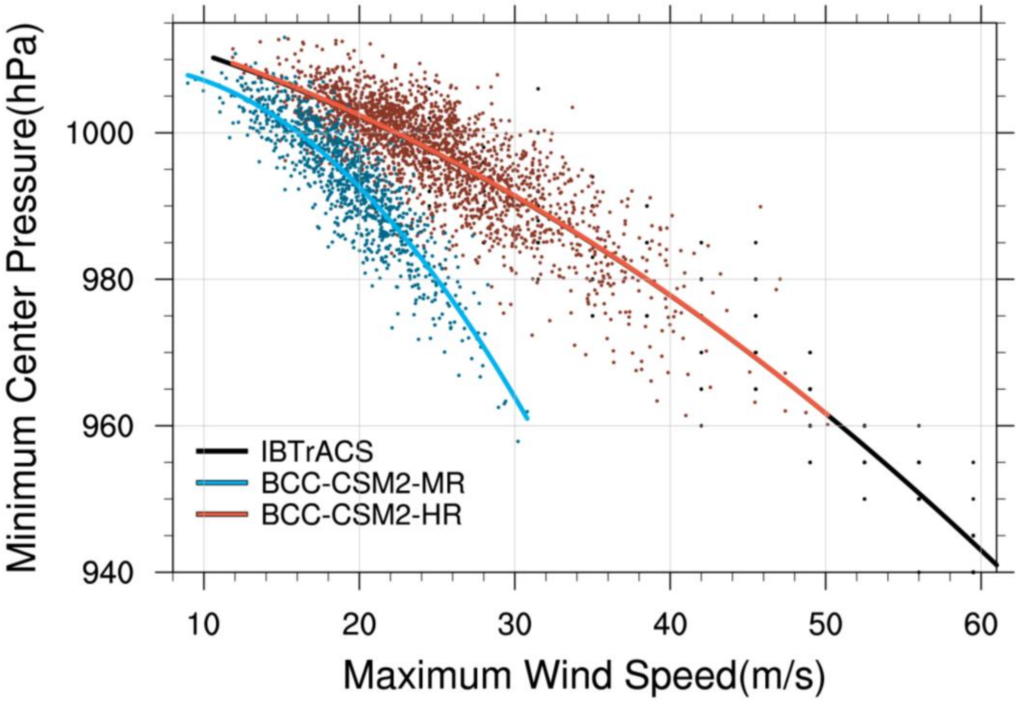

Figure 15~~4~~. Maximum surface wind speed (m s^{-1}) versus minimum sea level pressure (hPa) for tropical cyclones from 6-hourly data for ~~the~~ 1995~~81~~-2014~~00~~ ~~daily~~ IBTrACS observation (black dots and fitting line), and ~~the 1981-2000 daily~~ simulations from

BCC-CSM2-HR (red dots and fitting line) and BCC-CSM2-MR (blue dots and fitting line). Each dot denotes the maximum surface wind speed and its corresponding minimum sea level pressure for a tropical cyclone during its lifetime. ~~Here only plotted the tropical cyclones whose maximum surface wind speed exceeds 10 m s^{-1}.~~

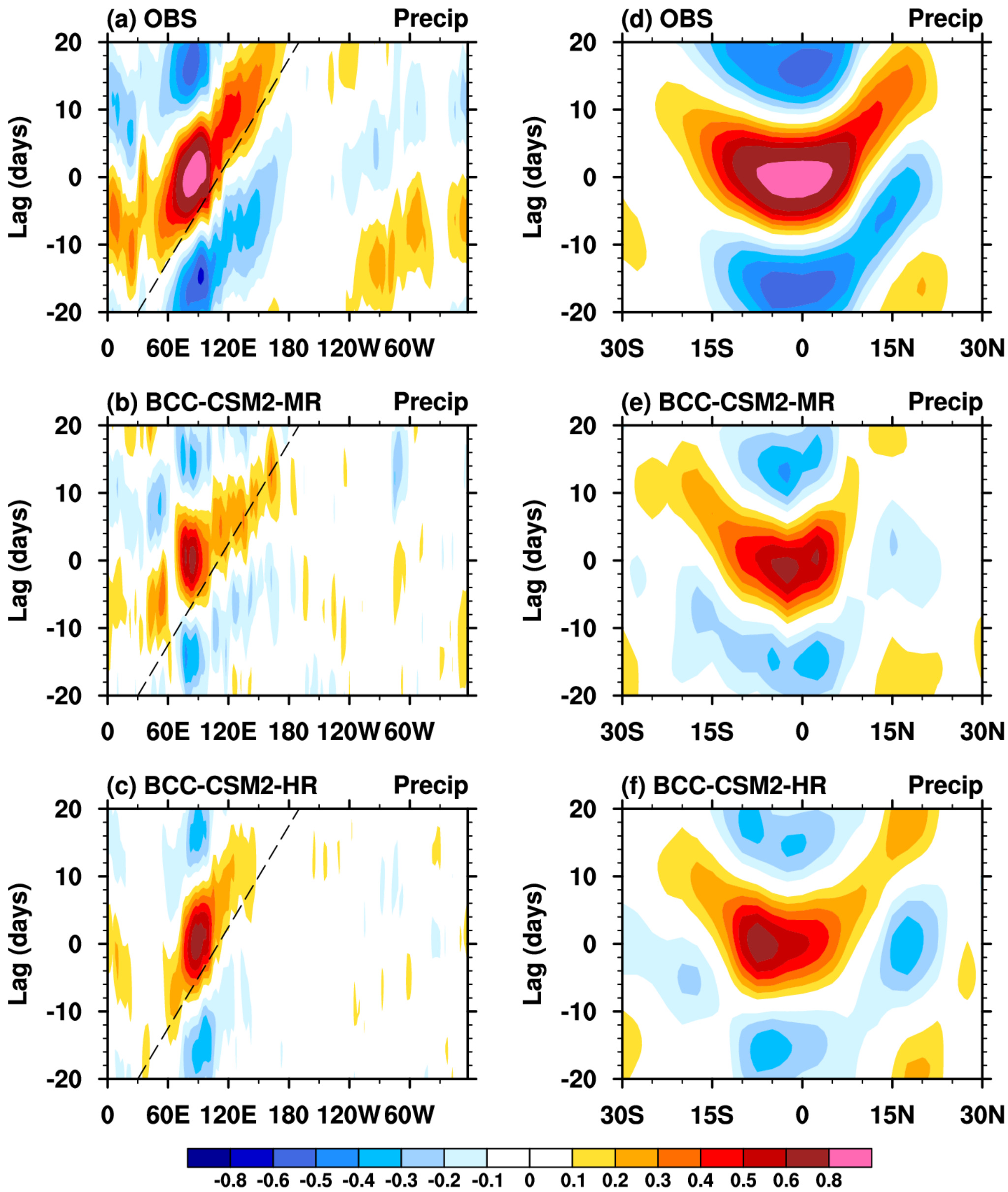
(a) OBS
Precip
(b) BCC-CSM2-MR
Precip
(c) BCC-CSM2-HR
Precip
(d) OBS
Precip
(e) BCC-CSM2-MR
Precip
(f) BCC-CSM2-HR
Precip
Lag (days)
20
10
0
-10
-20
0
60E
120E
180
120W
60W
30S
15S
0
15N
30N
-0.8 -0.6 -0.5 -0.4 -0.3 -0.2 -0.1 0 0.1 0.2 0.3 0.4 0.5 0.6 0.8

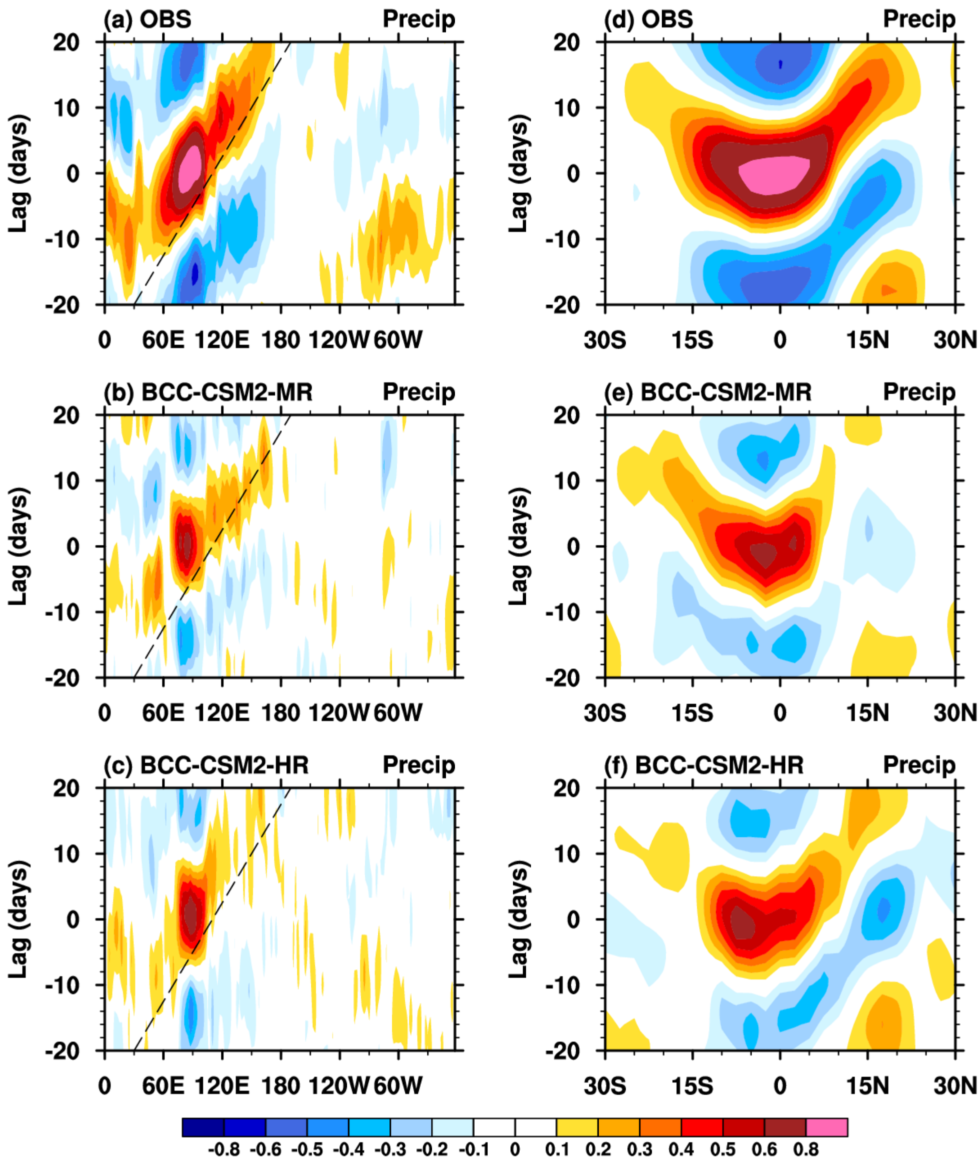

Figure 1~~5~~6. Left panels: longitude-time evolution of lagged correlation coefficient for the 20–100-day band-pass-filtered precipitation anomaly (averaged over 10 °S–10 °N) against regional averaged precipitation over the equatorial eastern Indian Ocean (80 °–100 °E, 10 °S–10 °N). Right panels: same as the left panels, but for the latitude-time evolution of lagged correlation coefficient for filtered precipitation anomaly (averaged over 80 °–100 °E) against the regional averaged precipitation over the equatorial eastern Indian Ocean. Dashed lines in each panel denote the 5 m s^{-1} eastward propagation speed. The observations in (a, b) are derived from GPCP data and the simulations are from (c,d) BCC-CSM2-MR, and (e,f) BCC-CSM2-HR for the period from 1995~~71~~ to ~~-~~2014~~00~~.

1827

1828

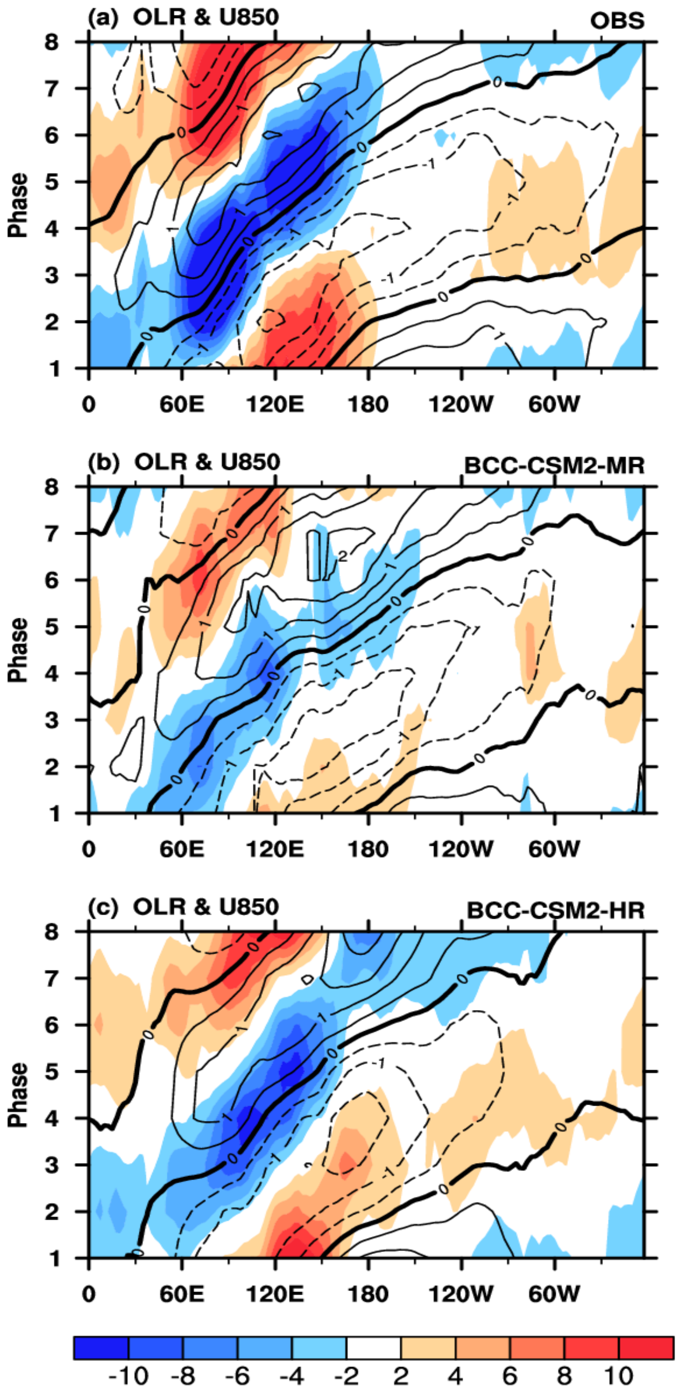

(a) OLR & U850
OBS
Phase
1 2 3 4 5 6 7 8
0 60E 120E 180 120W 60W
(b) OLR & U850
BCC-CSM2-MR
Phase
0 60E 120E 180 120W 60W
(c) OLR & U850
BCC-CSM2-HR
Phase
0 60E 120E 180 120W 60W
-10 -8 -6 -4 -2 2 4 6 8 10

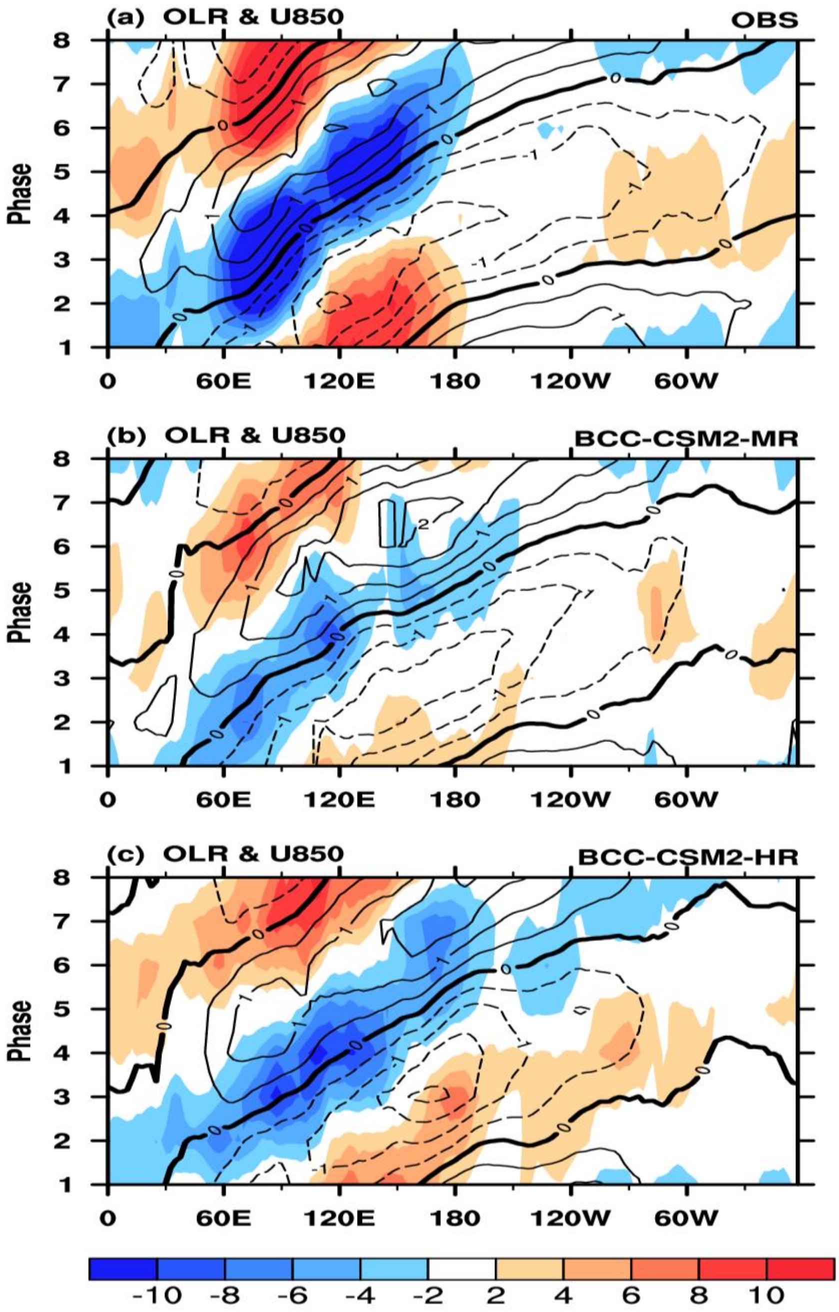

Figure 1~~6~~7. Hovmöller diagrams of MJO phase-composited OLR (shaded) and 850-hPa zonal wind anomalies (contour lines) averaged between 10 °S and 10 °N from (a) ERA5 wind and NOAA OLR reanalyses, (b) BCC-CSM2-MR and (c) BCC-CSM2-HR simulations for the period from 1995 to 2014. The MJO phase is defined by the two principal components corresponding to leading multivariate EOFs of OLR, 850-hPa and 200-hPa zonal wind anomalies as in Wheeler and Hendon (2004).

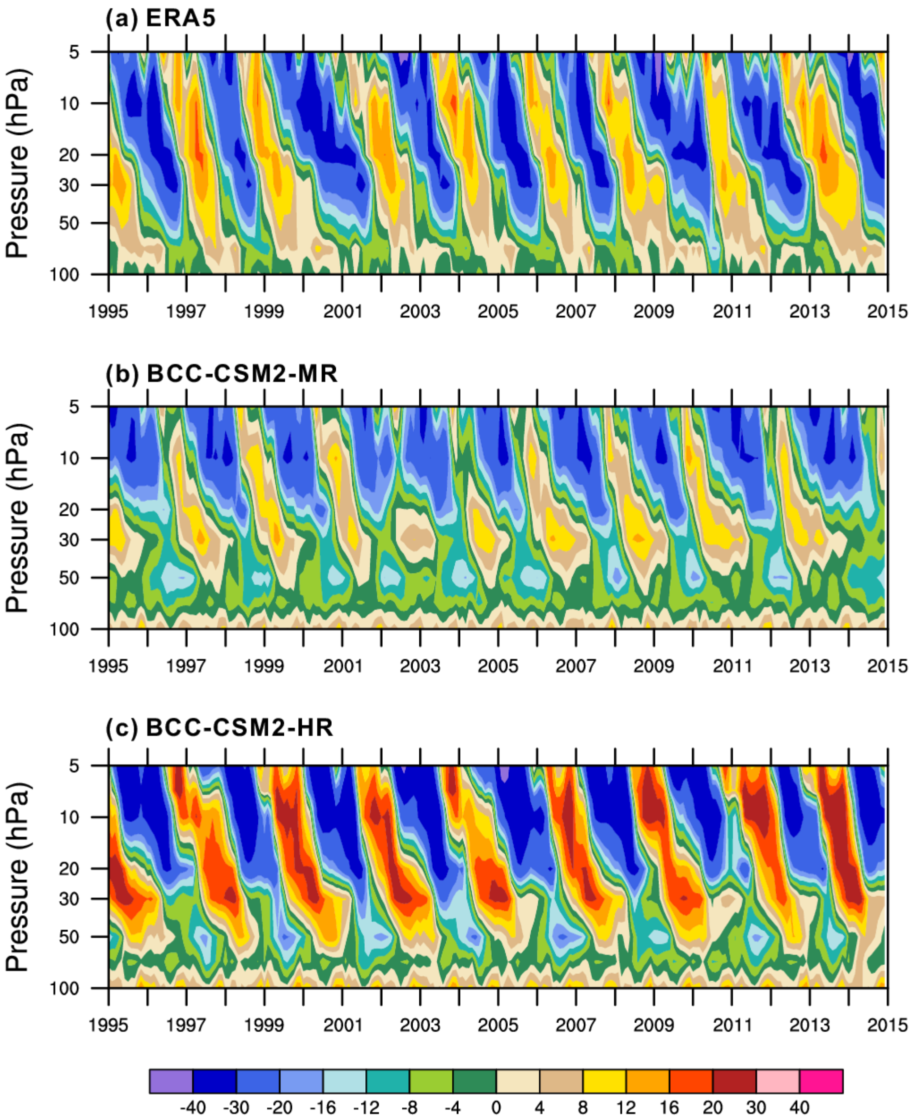
(a) ERA5
(b) BCC-CSM2-MR
(c) BCC-CSM2-HR
Pressure (hPa)
5
10
20
30
50
100
1995
1997
1999
2001
2003
2005
2007
2009
2011
2013
2015
-40 -30 -20 -16 -12 -8 -4 0 4 8 12 16 20 30 40

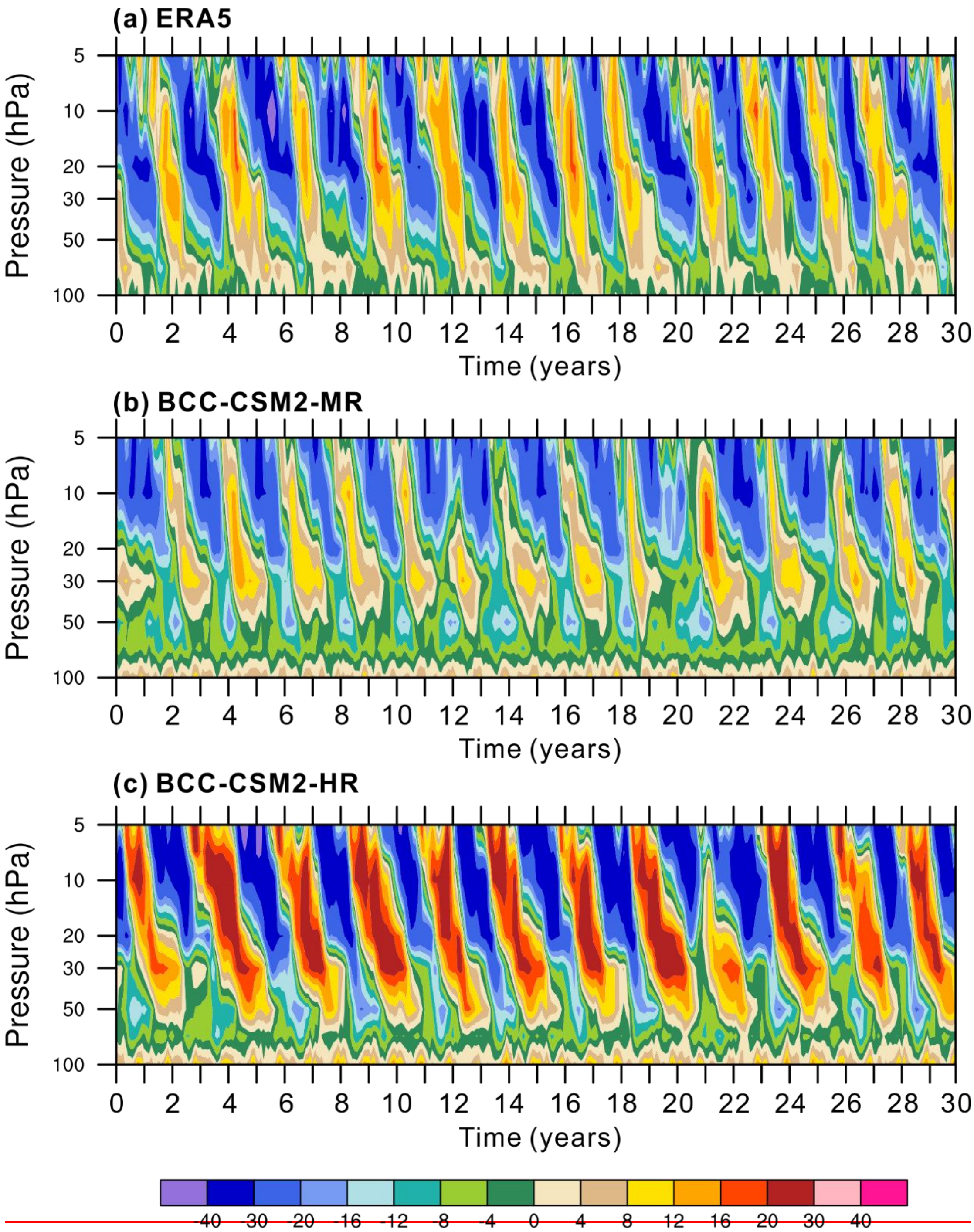

Figure 1~~7~~8. Tropical zonal winds (m s^{-1}) between 5 °S and 5 °N in the lower stratosphere for (a) ERA5 reanalysis ~~(1981–2010)~~, (b) BCC-CSM2-MR ~~(1971–2000)~~ and (c) BCC-CSM2-HR ~~(1971–2000)~~ during the period from 1995 to 2014.~~.~~

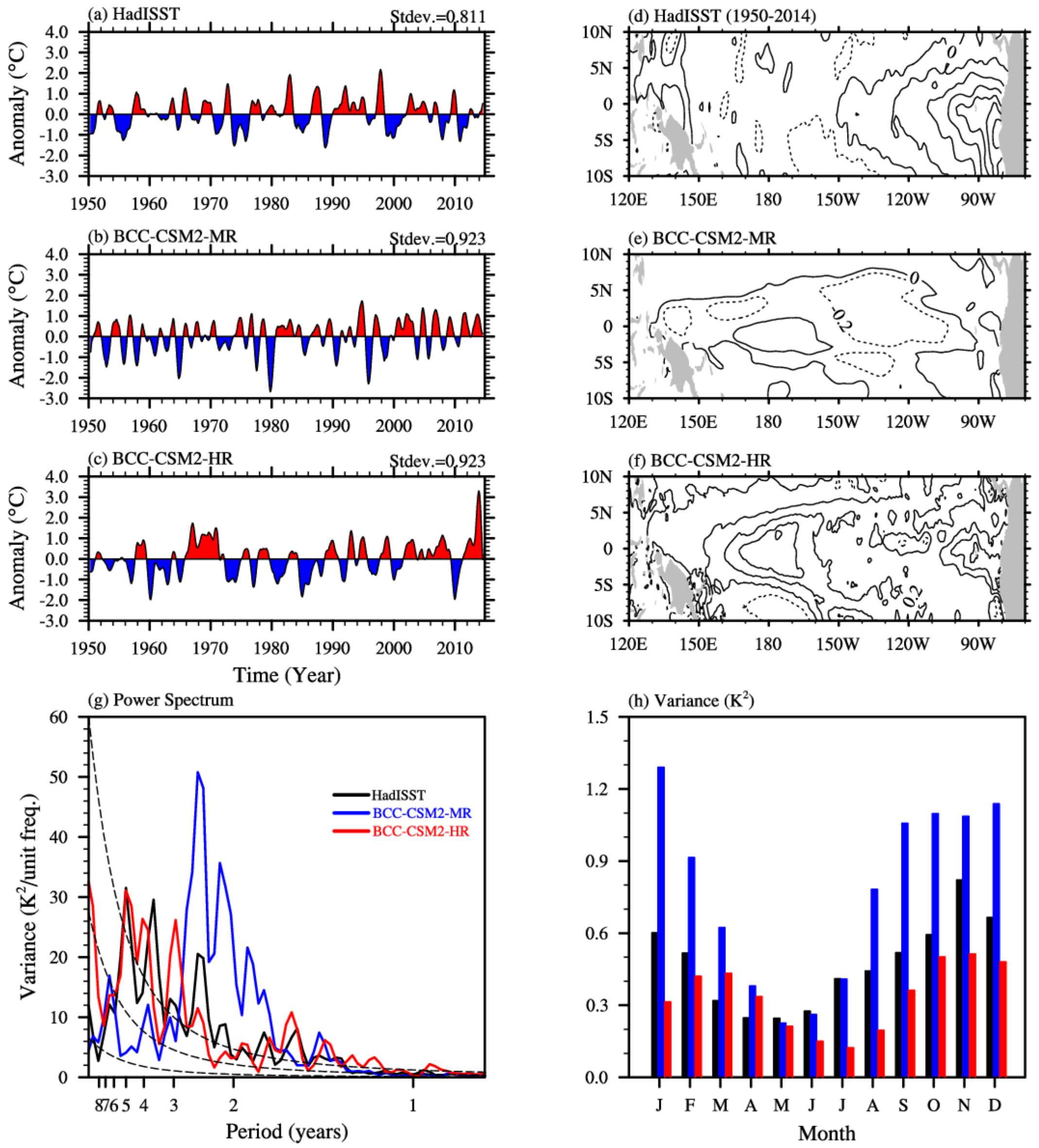
(a) HadISST
Stdev.=0.811
(b) BCC-CSM2-MR
Stdev.=0.923
(c) BCC-CSM2-HR
Stdev.=0.923
Anomaly (°C)
Time (Year)
(d) HadISST (1950-2014)
(e) BCC-CSM2-MR
(f) BCC-CSM2-HR
120E
150E
180
150W
120W
90W
10N
5N
0
5S
10S
(g) Power Spectrum
HadISST
BCC-CSM2-MR
BCC-CSM2-HR
Variance (K²/unit freq.)
Period (years)
(h) Variance (K²)
J F M A M J J A S O N D
Month

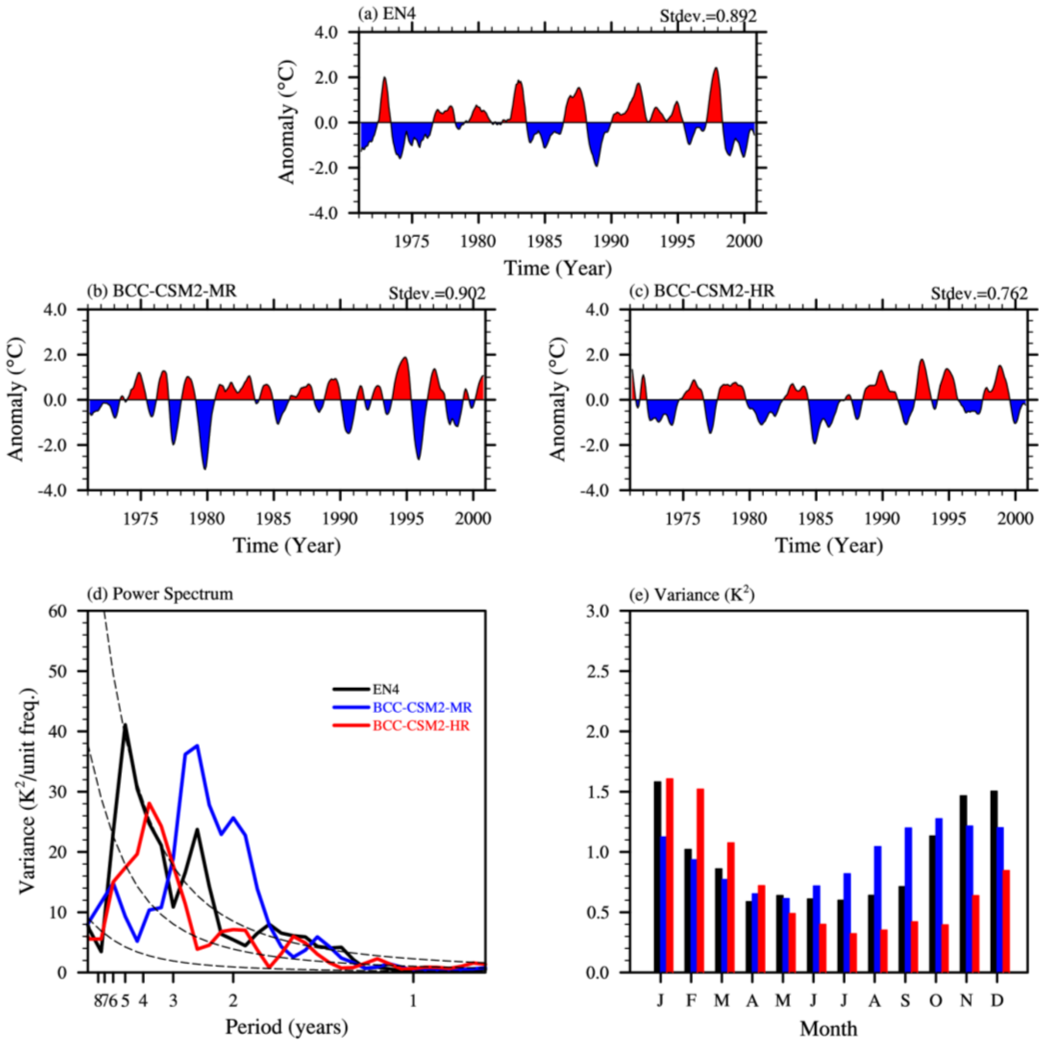

Figure 19~~18~~. ~~T~~The time series of monthly Niño3.4 SST (5°N−5°S, 170°W−120°W) anomalies and spatial distribution of their skewness for (a, d) ~~(a)~~ HadISST~~EN4~~ observation, (b, e) BCC-CSM2-MR, and (c, f) BCC-CSM2-HR during the period 1950~~71~~-2014~~00~~. ~~–~~ (g~~d~~) and (h~~e~~) showshow ~~show~~ their power spectrums and variances, respectively, and ~~. T~~the black, blue, and red solid lines denotes ~~in (d) and (e) show~~ the results from HadISST~~EN4~~, BCC-CSM2-MR, and BCC-CSM2-HR.

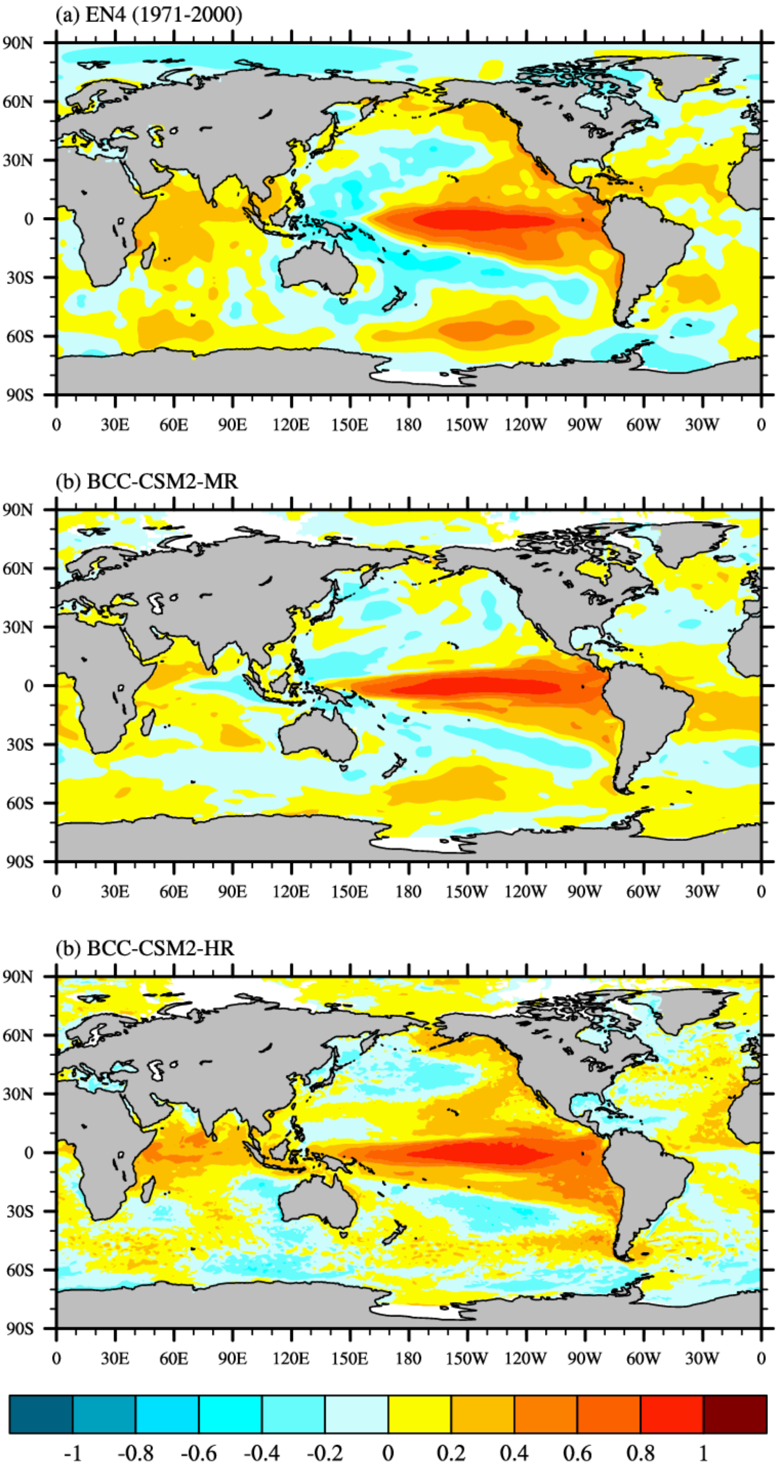
(a) EN4 (1971-2000)
(b) BCC-CSM2-MR
(b) BCC-CSM2-HR
90N
60N
30N
0
30S
60S
90S
0
30E
60E
90E
120E
150E
180
150W
120W
90W
60W
30W
0
-1
-0.8
-0.6
-0.4
-0.2
0
0.2
0.4
0.6
0.8
1

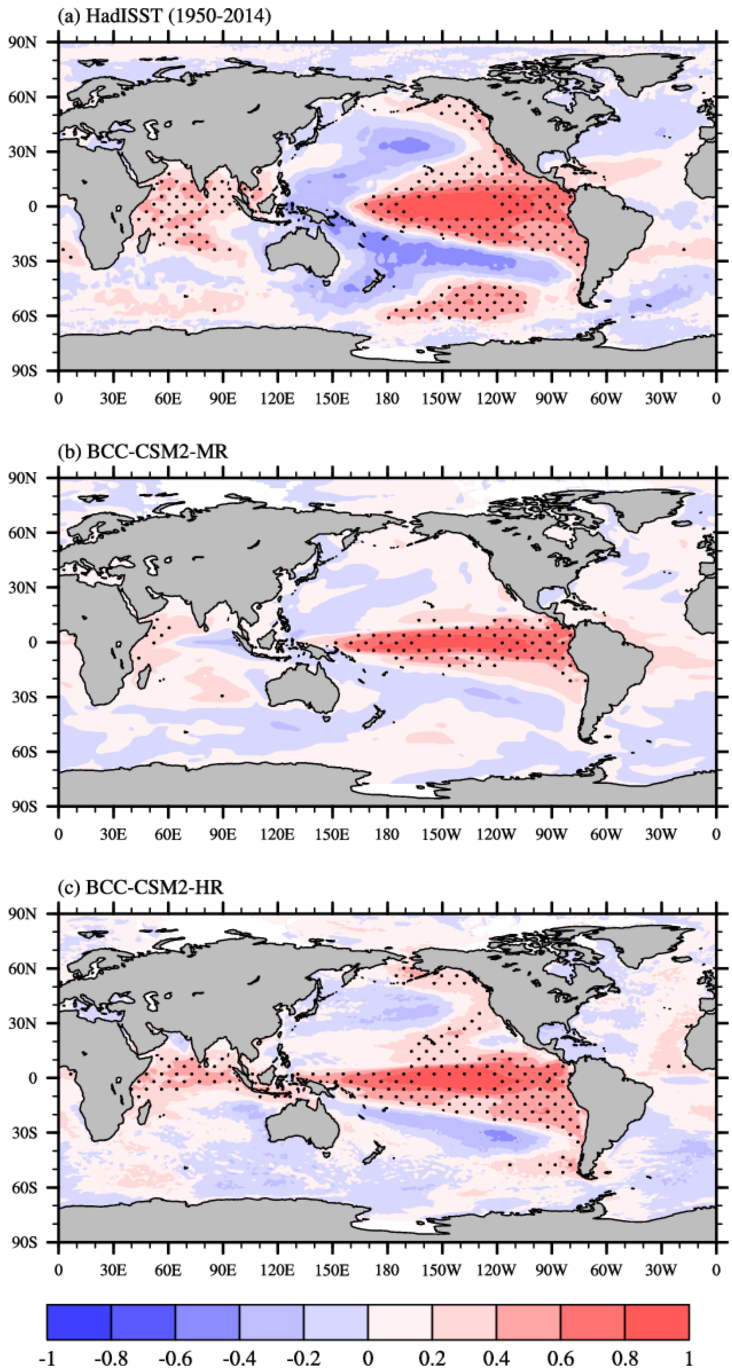

Figure 20~~19~~. Correlation coefficients between SST and the Nino3.4 index from 1950~~71~~ to 2014~~00~~ for (a) HadISST~~EN4~~ data, (b) BCC-CSM2-MR, and (c) BCC-CSM2-HR. Contour intervals are 0.2. Values significant at the 99% level using a Student's t-test are stippled.